LA-UR-12-22357
Approved for public release; distribution is unlimited.

Title: Advanced sample environments for in situ neutron diffraction studies of nuclear materials

Author(s): Reiche, Helmut M.

Intended for: Dissertation

ADVANCED SAMPLE ENVIRONMENTS FOR *IN SITU* NEUTRON DIFFRACTION STUDIES OF NUCLEAR MATERIALS

BY

HELMUT MATTHIAS REICHE, B.Sc., M.Sc.

A dissertation submitted to the Graduate School

in partial fulfillment of the requirements

for the degree

DOCTOR OF PHILOSOPHY

Specialization in: Electrical Engineering

NEW MEXICO STATE UNIVERSITY

Las Cruces, New Mexico

August 2012

UNCLASSIFIED LA-UR-12-22357

"Advanced Sample Environments for *in situ* Neutron Diffraction Studies of Nuclear Materials," a dissertation prepared by Helmut Matthias Reiche in partial fulfillment of the requirements for the degree, Doctor of Philosophy, has been approved and accepted by the following:

Linda Lacey
Dean of the Graduate School

Dr. Steven Stochaj
Chair of the Examining Committee

Date

Committee in charge:

Dr. Steven Stochaj, Chair

Dr. Heinz Nakotte

Dr. Kwong Ng

Dr. David Voelz

Dr. Sven Vogel

DEDICATION

To

Erica

&

Shoshanah

ACKNOWLEDGEMENTS

I'm very thankful to our Creator for providing me with this opportunity and granting me my supporting and loving wife Erica. Thank you, Erica, for your interest in my work and your continuous support throughout many days of fervent research, conducting experiments, analyzing data and compiling results contained in this work. Thank you also for taking good care of our newborn baby girl, Shoshanah. I'm indebted to my mentor at LANL, Dr. Sven Vogel, for patiently helping me to grasp crucial concepts of material science, in particular, the Rietveld refinement. Thank you for teaching me and being the proverbial mentor every student desires to have offering advice, continuous encouragement and always finding a way to make time in an ever busier time schedule. My further appreciation goes to my advisor at NMSU, Prof. Dr. Steve Stochaj, for his time and effort in working out all the intricate details and administrative challenges a dissertation entails, as well as timely guidance. I am very grateful to Prof. Dr. Heinz Nakotte for providing me this fantastic Post-Master's opportunity of continuing my education at NMSU to obtain this doctorate. I am extremely thankful for Dr. Luke Daemen for going beyond helping me with all my chemistry needs to synthesize the samples for my dissertation. My gratefulness goes also to Sabrina Labs for her support in preparing the electron microscopy samples, Ming Tang for the TEM and Darrick Williams for the SEM work. Thanks also to Eric Larson for his frequent instantaneous support related to CAD modeling. I also like to thankfully recognize Paula Mosbrucker and James Wall for their substantial contributions in developing the deformation furnace and high-temperature furnace

respectively. I extend my appreciation also to Jason Burkhart and Melvin Borrego for their timely mechanical support.

Thanks to the American Institute of Physics (AIP) for granting me permission to reuse all content of the following papers I published in the Journal Review of Scientific Instruments. Chapter 3 and 4.1 contain information reprinted with permission from H.M. Reiche and S.C. Vogel, Review of Scientific Instruments, Vol. 81, page 93302, Copyright 2010, American Institute of Physics. Chapter 4.2 and 5 contain information reprinted with permission from H.M. Reiche, S.C. Vogel, P. Mosbrucker, E.J. Larson and M.R. Daymond, Review of Scientific Instruments, Vol. 83, page 053901, Copyright 2012, American Institute of Physics.

VITA

2001	Energieelektroniker, IHK, Betriebstechnik, Gesellenbrief. - Honorary Certificate for Best of State - Professional Certification as Energy Electronics Specialist, Chamber of Commerce and Industry, Saarland, Germany
2002	Fachhochschulreife, Fachoberschule St. Wendel. - Summa Cum Laude - Award for Best of State - University of Applied Sciences Entrance Qualification, Technical Secondary School, St. Wendel, Saarland, Germany
2004	Bachelor of Science in Electrical and Electronics Engineering, HTW, University of Applied Sciences, Saarbrücken, Saarland, Germany
2006	Master of Science in Electrical and Electronics Engineering, - Summa Cum Laude - HTW, University of Applied Sciences, Saarbrücken, Saarland, Germany
2012	Doctor of Philosophy in Electrical Engineering, - Certificate of Recognition for GPA of 4.0 - New Mexico State University, Las Cruces, NM, USA

PUBLICATIONS

[1] H.M. Reiche, S.C. Vogel, P. Mosbrucker, E.J. Larson, and M.R. Daymond, "A furnace with rotating load frame for in situ high temperature deformation and creep experiments in a neutron diffraction beam line," *Rev. Sci. Instrum.*, vol. 83, no. 5, p. 053901, 2012.

[2] Y. Fujioka, J. Frantti, S.C. Vogel, J. Zhang, Z. Lin, H. Reiche, A. Losko, and L.L. Daemen, “Neutron powder diffraction study of the effect of Mn-doping on $SrTiO_{3,}$” Mater. Sci. Forum, vol. 700, pp. 28-32, 2012.

[3] H.M. Reiche and S.C. Vogel, "A versatile automated sample changer for texture measurements on the high pressure-preferred orientation neutron diffractometer," Rev. Sci. Instrum., vol. 81, no. 9, p. 93302, 2010.

[4] M.A. Rodriguez , M.H. Van Benthem, D. Ingersoll, S.C. Vogel, and H.M. Reiche, “In-situ analysis of $LiFePO_4$ Batteries: Signal Extraction by Multivariate Analysis,” Powder Diffr., vol. 25, pp.143-148, 2010.

[5] K. Kothapalli, F. Nasreen, J. Peterson, H. Nakotte, S. El-Khatib, S.C. Vogel, A. Llobet, H. Reiche, I. Swainson, and E. Brück, “Effect of temperature on hybridization and magnetism in UPdSn and UCuSn,” J. Appl. Phys., vol. 105, p. 07E121, 2009.

[6] E.A. Juarez-Arellano, B. Winkler, A. Friedrich, D.J. Wilson, M. Koch-Müller, K. Knorr, S.C. Vogel, J.J. Wall, H. Reiche, W. Crichton, M. Ortega-Aviles, and M. Avalos-Borja, “Reaction of rhenium and carbon at high pressures and temperatures,” Z. Kristallogr., vol. 223, pp. 492-501, 2008.

[7] S.C. Vogel, H.M. Reiche, P.G. Bruch, and J. Seal, “High Pressure Preferred Orientation (HIPPO) – Sample Changer,” American Conference on Neutron Scattering 2008, Santa Fe, NM

[8] J.J. Wall, S.C. Vogel, H.M. Reiche, and B. Winkler, “An ultra-high temperature furnace for in-situ time of flight neutron diffraction,” American Conference on Neutron Scattering 2008, Santa Fe, NM

[9] S.C. Vogel, H. Reiche, and D.W. Brown, “High pressure deformation study of zirconium,” Powder Diffr., vol. 22, no. 2, pp.113-117, 2007.

FIELD OF STUDY

Major Field: Electrical Engineering

ABSTRACT

ADVANCED SAMPLE ENVIRONMENTS FOR *IN SITU*
NEUTRON DIFFRACTION STUDIES OF
NUCLEAR MATERIALS

BY

HELMUT MATTHIAS REICHE, B.Sc., M.Sc.

Doctor of Philosophy, Engineering

Specialization in Electrical Engineering

NEW MEXICO STATE UNIVERSITY

Las Cruces, New Mexico, 2012

Dr. Steven J. Stochaj, Chair

Generation IV nuclear reactor concepts, such as the supercritical-water-cooled nuclear reactor (SCWR), are actively researched internationally. Operating conditions above the critical point of water (374˚C, 22.1 MPa) and fuel core temperature that potentially exceed 1850˚C put a high demand on the surrounding materials. For their safe application, it is essential to characterize and understand the material properties on an atomic scale such as crystal structure and grain orientation (texture) changes as

a function of temperature and stress. This permits the refinement of models predicting the macroscopic behavior of the material. Neutron diffraction is a powerful tool in characterizing such crystallographic properties due to their deep penetration depth into condensed matter. This leads to the ability to study bulk material properties, as opposed to surface effects, and allows for complex sample environments to study e.g. the individual contributions of thermo-mechanical processing steps during manufacturing, operating or accident scenarios.

I present three sample environments for *in situ* neutron diffraction studies that provide such crystallographic information and have been successfully commissioned and integrated into the user program of the *High Pressure – Preferred Orientation* (HIPPO) diffractometer at the *Los Alamos Neutron Science Center* (LANSCE) user facility. I adapted a sample changer for reliable and fast automated texture measurements of multiple specimens. I built a creep furnace combining a 2700 N load frame with a resistive vanadium furnace, capable of temperatures up to 1000˚C, and manipulated by a pair of synchronized rotation stages. This combination allows following deformation and temperature dependent texture and strain evolutions *in situ*. Utilizing the presented sample changer and creep furnace we studied pressure tubes made of Zr-2.5wt%Nb currently employed in CANDU® nuclear reactors and proposed for future SCWRs, acting as the primary containment vessel of high temperature heavy water (D_2O) inside the reactor core. The measured sample texture shows that upon traversing the phase transition, which proceeded according to the Burger orientation relationship, variant selection occurred during heating and cooling

of the zirconium alloy. Experimental results of lattice strains depending on the crystallographic orientation can be used to calculate strain pole figures which grant insight into the three-dimensional mechanical response of a polycrystalline aggregate and represent an extremely powerful material model validation tool.

Lastly, I developed a resistive graphite high-temperature furnace with sample motion for *in situ* crystal structure and texture measurements of nuclear materials at steady-state temperatures up to at least 2200˚C. This permits *in situ* observation of e.g. phase transitions and coefficients of thermal expansion, as well as phase formation and texture development during solidification. Utilizing this apparatus, I investigated the carbothermic reduction of UO_2 nanopowder forming uranium carbide, a promising Generation IV reactor fuel. The onset of the $UO_2 + 2C \rightarrow UC + CO_2$ reaction was observed at 1440˚C with the bulk portion being complete at 1500˚C. I describe the novel synthesis for this nanoparticle UO_2 powder, which closely imitates observed nano grains in partially burnt reactor fuels. Of the three opposing structure models reported for the non-quenchable cubic UC_2 phase, stable between 1769˚C and 2560˚C, the NaCl-type structure according to Bowman is found to be correct. This is deemed major progress as the CaF_2-type structure was used for recent thermal modeling of safety critical factors in nuclear reactors. A temperature dependent increase in density due to carbon diffusion has been observed and quantified. I provide first experimental data of an unspecified, reversible order-disorder transition in this δ-phase with its onset at ~1800˚C which is likely due to rotating C_2 molecules in the sublattice.

TABLE OF CONTENTS

LIST OF TABLES

Page

LIST OF FIGURES

Page

1.0 INTRODUCTION

In this introductory section, I outline the objectives of this dissertation, present a general overview of the topics discussed and elucidate on the order they are presented.

1.1 Objective

The purpose of this dissertation is to present novel sample environments for *in situ* neutron diffraction as well as their scientific application to study nuclear materials. Increasing demand for safety, sustainability and cost-effectiveness drives the research and development of a new generation of nuclear reactors operating at stringent conditions of high temperatures and stresses. In order to achieve long, reliable and effective performance of the nuclear materials deployed, accurate characterization at their operating and accident conditions is indispensable to gain thorough understanding. Therefore, three sample environments have been designed, built and successfully commissioned by the author with collaboration ranging from internal staff to international alliances.

The first nuclear material studied is a zirconium alloy used for pressure tubes of existing CANDU® nuclear power plants as well as anticipated for use in the harsher environment of future supercritical-water-cooled nuclear reactors (SCWRs). Characterizing the impact of crystallographic material changes that occur during the manufacturing process will aid in predicting the behavior of this alloy and its performance as a pressure tube. With the development of a creep furnace, I provide a

sample environment to simulate thermo-mechanical processing steps at elevated temperatures and uni-axial stress in the confined environment of a neutron diffraction beamline.

The second investigated material is uranium carbide anticipated for use as a nuclear fuel in Generation IV reactors. In particular the non-quenchable high-temperature phase accessible during accidental or even normal operating conditions in a reactor is poorly known, but of paramount importance for e.g. thermo-dynamical modeling. Constrained to study the phase above its formation temperature of ~1770˚C, I designed, built and operated a high-temperature furnace in a neutron diffractometer characterizing the phase properties.

1.2 Dissertation Organization

As a note to the reader, the research, preparation, experiments and analysis discussed in this work which I primarily achieved myself will be portrayed in the first person singular. Areas, for which a collaboration was indispensable, I will use the first person plural.

First, the necessary background information will be laid out in Chapter 2.0 to establish a foundation for the presented novelties in their proper context. As neutron diffraction is the investigative tool of choice to investigate the material properties in question, an overview of neutron physics is provided in section 2.1. Fundamentals of crystallography represents another essential building block elucidated in section 2.2, followed by a brief introduction to electron microscopy in section 2.3 necessary to

complement the results found with neutron diffraction. The chapter concludes with a review of existing and anticipated nuclear reactors in section 2.4, which outlines the trend for materials to operate in more demanding environments. The characterization of these underlines the necessity of the sample environments presented in this dissertation.

Chapter 3.0 is dedicated to the experimental approach. The entire collection of sample environments are designed to operate in the HIPPO diffractometer described in section 3.1, followed by a discussion of the utilized data analysis tools in section 3.2, and software I wrote to visualize parts of these results in section 3.3. Concluding remarks include a discussion of inherent peculiarities of the neutron diffraction techniques in section 3.4.

Chapter 4.0 covers the developed sample environments. The improved sample changer for routine neutron diffraction experiments is presented in section 4.1 to optimize the usage of available neutron flux and reduce instrument down time, especially for quick sample measurements (on the order of minutes). A sample environment allowing for uni-axial stress at elevated temperatures and creep experiments is the creep furnace shown in section 4.2. Lastly, a high-temperature furnace for *in situ* crystal structure and texture measurements of materials at temperatures up to at least 2200˚C is described in detail in section 4.3.

Experiments utilizing the developed sample environments are presented in Chapter 5.0 and 6.0 providing a glance of the innovative science now accessible, especially for novel materials in nuclear reactors. While the sample changer

establishes a reference for both experiments, the creep furnace was used in Chapter 5.0 to investigate texture and strain evolution in Zr-2.5wt%Nb a pressure tube material in present CANDU nuclear reactors and anticipated for use in SCWR, a Generation IV reactor. The experiment successfully decouples the effects of phase transitions, uni-axial stress and temperature treatments present during the manufacturing process. Using the high-temperature furnace, we study the carbothermic reduction of innovatively synthesized uranium dioxide nano powder to form uranium carbide in the neutron beam presented in Chapter 6.0. Uranium carbides are actively researched for deployment in future Generation IV nuclear reactors. Structure of the poorly known high-temperature phase is presented and an order-disorder transition discussed.

Novelty and scientific contribution of each topic will be discussed in the opening section of their corresponding Chapter 4.0 through 6.0. Lastly, I summarize and conclude the work presented in this dissertation in Chapter 7.0.

2.0 THEORETICAL FOUNDATION AND APPROACH

In this chapter, I explain neutron scattering, as this is the experimental tool chosen to investigate the crystallographic properties of materials inside the developed sample environments. Crystal structure and texture is introduced followed by a brief explanation of electron microscopy as a powerful and complimentary tool to neutron diffraction. Lastly, existing and future nuclear power plants and their fuel materials are outlined in order to show the growing demand to investigate and predict material behavior at extended extreme operating conditions and accident scenarios.

2.1 Neutron Physics

Neutrons are composed of one ‘up’ quark and two ‘down’ quarks with a spin of ½. Thus, neutrons are fermions (with half-integer spin) that belong to the baryon family (composed of three quarks), which is a subcategory of the hadrons (interact by the strong force). Neutrons have no electric charge, a rest mass of 1.008665 u or $1.674927*10^{-27}$ kg and a nuclear magnetic moment of $-0.96623647 \cdot 10^{-26}$ J T^{-1}[1]. A free neutron decays with a half-life of 881.5±1.5 seconds [2] whereby one of the two down-quarks is transformed into an up-quark (forming a proton) and a virtual W^- boson, which decays within the allowed time frame of Heisenberg’s uncertainty principle into an electron and an electron antineutrino. Hence, free neutrons must be produced shortly before their application.

2.1.1. **Why Neutron Diffraction?**

Optical systems are limited in their capability to resolve small details. This minimal resolvable separation δ is directly proportional to the wavelength λ of the employed method of illumination according to the Rayleigh criterion:

$$\delta = \frac{0.61}{sin\theta}\lambda \tag{2.1}$$

where $sin\theta$ is the numerical aperture, which can be approximated by the diameter of the optical lens divided by twice the focal length. As such, the minimal resolvable separation δ investigated with visible light (λ ~ 400 – 700 nm) is on the order of 400 nm. Atomic radii are three orders of magnitude smaller with 0.1 nm, or 1 Å (angstrom). Hence, instead of visible light, neutron scattering, X-ray techniques and electron microscopy (section 2.3) have emerged to investigate interatomic details. Figure 2.1 illustrates the negative correlation between the atomic number Z of a material penetrated by X-rays or electrons. In contrast, the penetration depth of neutrons varies erratically with the atomic number (as well as the number of neutrons in the nucleus). This allows to differentiate elements with largely different atomic number as well as isotopes using neutron diffraction, which otherwise are indistinguishable with X-rays. For example, hydrogen in the presence of heavier atoms (such as lead or uranium) can be localized with neutrons but are virtually invisible with X-rays. The advantages of deep penetration combined with hydrogen sensitivity are exemplified with neutron radiography: A dense material with high

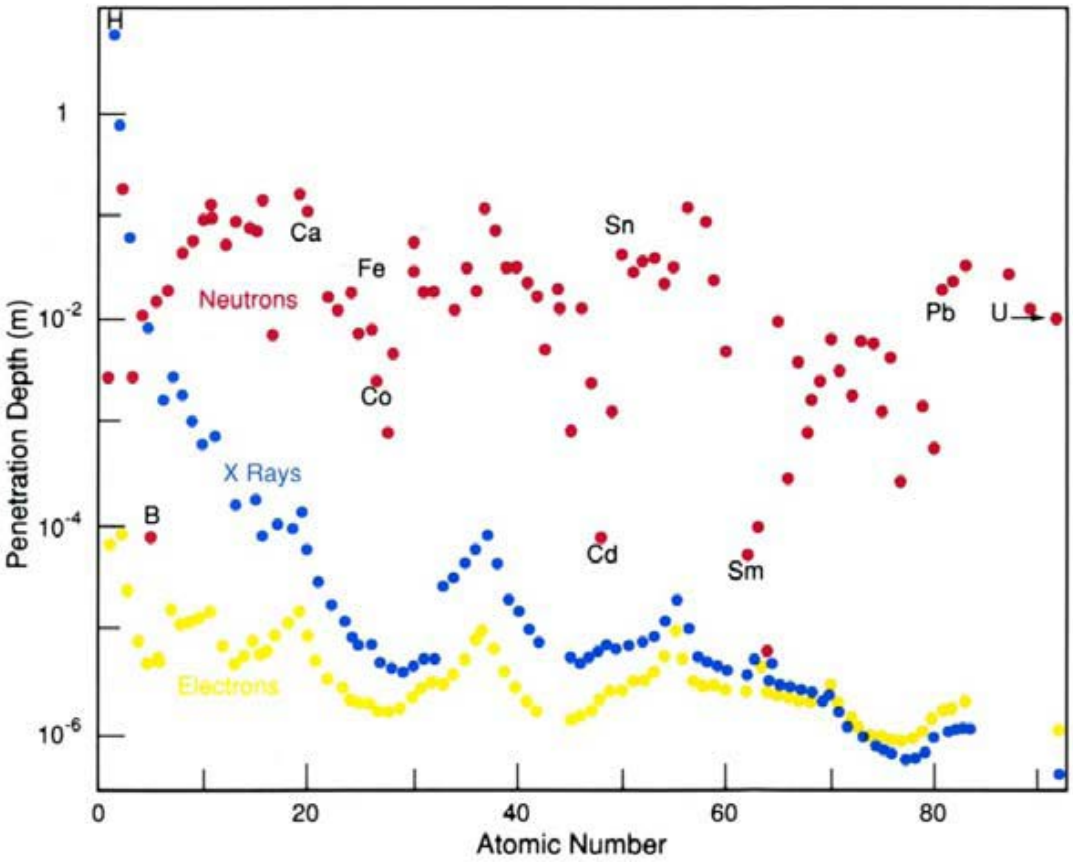

Figure 2.1: Penetration depth of neutrons (red, top), X-rays (blue, middle) and electrons (yellow, bottom) as a function of atomic number of the penetrated material.

atomic number (lead) can be penetrate, while being able to resolve the intricate details of a rose petal or leaf with a spatial resolution of 10 μm (Figure 2.2).

On average neutrons penetrate two orders of magnitude deeper into the material (Figure 2.1) than X-rays and available beam spot sizes are on the order of centimeters. This permits the study of large sample volumes (1 mm^3 to several cm^3) that are representative of the bulk properties, as opposed to the surface sensitivity of X-rays, electrons, or the comparably small volumes probed with synchrotrons. Especially for texture measurements, this allows to probe a large numbers of grains in

Figure 2.2: Photograph (left) and neutron radiography image (right) illustrate the penetration depth of neutrons [7]. The hydrogen from the water inside a rose can be spatially resolved up to ~10μm inside a lead container used for transporting radioactive materials.

order to obtain sufficient grain statistics to reliably determine the orientation distribution function (ODF) even in cases of large grained materials (grain size on the order of 1 mm) [3], which results frequently from high temperature treatments of metals, alloys and rocks. Neutrons also allow investigation of the magnetic structure and enables the construction of environmental cells to investigate samples under conditions of high and low temperature [4], [5], [6], pressure, stress or magnetic and electric fields [7].

2.1.2. **Neutron Generation**

For research, neutrons are mainly generated in either nuclear reactors, where neutrons emerge from nuclear fission reactions (see section 2.4.2), or by spallation, a process in which neutrons are ejected (spalled off) from a nucleus due to fast impacting particles such as protons.

For my research, I used spallation neutrons from LANSCE (*Los Alamos Neutron Science Center*) [7], [8] at LANL (*Los Alamos National Laboratory*, Los Alamos, NM, USA). At LANSCE, two ion sources inside a high voltage dome of a 750 keV Cockcroft-Walton generator provide hydrogen ions, one positively charged H^+ ions (protons) and the second negatively charged H^- ions (one proton with two electrons). These particles are merged, bunched and matched into a drift-tube linear accelerator (linac) for further acceleration to 100 MeV. The last and longest stage of the accelerator (800 m) is the side-coupled-cavity linac, where these particles are accelerated to their final energy of 800 MeV (corresponding to 84% of the speed of light). At LANSCE, the positive hydrogen ions, in case of H^- ions stripped of their electrons, are then injected into a 30 m in diameter proton storage ring (PSR). The PSR converts a 625 μs pulse of hydrogen ions into a 125 ns intense burst of protons, which is guided to the heavy-metal spallation target. Different target materials are used for spallation neutron production, e.g. uranium is used at ISIS, tungsten at LANSCE, liquid lithium at Soreq NRC and liquid mercury at SNS. Proton currents at the brightest spallation sources currently available are 125 μA at LANSCE, 200 μA at ISIS and 1.4 mA at SNS.

Figure 2.3 shows the historical evolution of the performance of neutron sources. In all cases it should be noted that the neutron flux (number of neutrons per unit area and unit time) at the sample is much lower than the peak flux provided by the source. As a representative example for spallation facilities, the spallation neutron source at LANSCE produces $10^{16}\frac{neutrons}{cm^2 s}$. Even at a diffractometer with a short flight path such as HIPPO (section 3.1), where the moderator to sample distance is ~8.83 m, a flux of $1.12 \cdot 10^{7}\frac{neutrons}{cm^2 s}$ (at 120 μA proton current) [10] is available in the thermal (<~0.4 eV) range of neutron energies suitable for diffraction. The closest counterpart to HIPPO is the diffractometer Powgen at the Spallation Neutron Source (SNS, Oak Ridge, TN) which has a neutron flux of $4 \cdot 10^{6}\frac{neutrons}{cm^2 s}$ but compared to HIPPO

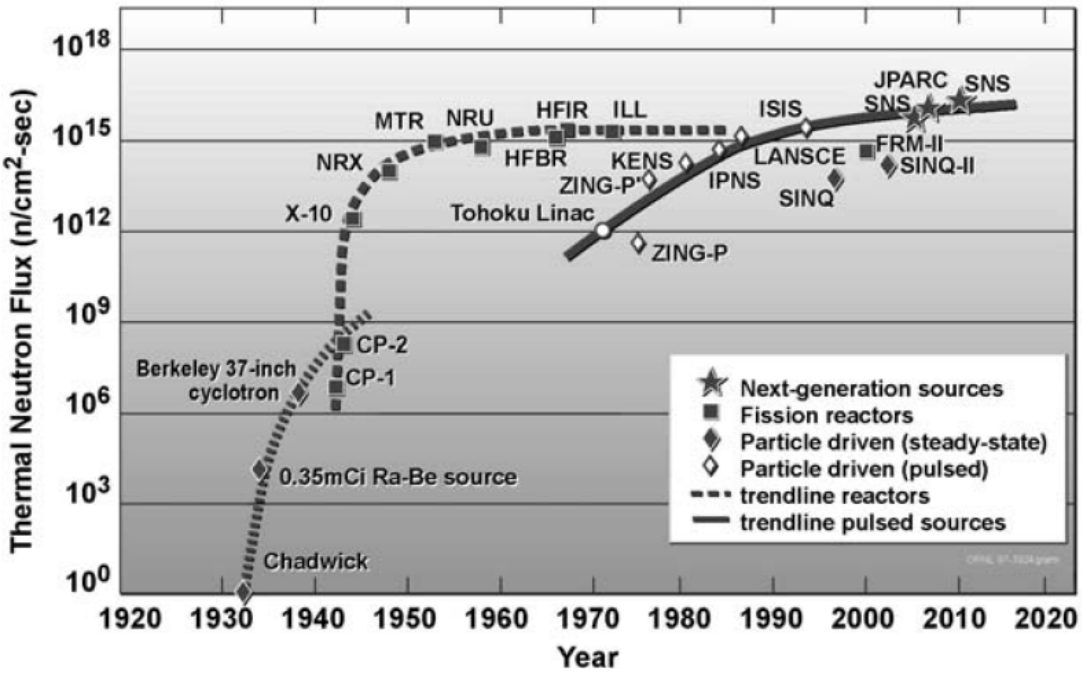

Figure 2.3: Historic development of neutron sources. Performance measured in peak thermal neutron flux [9].

twice [11] the resolution with $\Delta d/d=0.0015$ [12] due to its 60 m distance from moderator to sample. These thermal neutron intensities are small as compared to the number of atoms in a cubic centimeter of solid material. Hence, even after days of exposure, it is apparent that the radiation damage from thermal neutrons for most materials is negligible, as opposed to e.g. X-ray diffraction (XRD) with an about three orders of magnitude higher particle flux.

2.1.3. **Neutron Moderation**

Neutrons generated by reactor or spallation sources initially have energies far too high than the energies required to measure properties relevant to solid state physics. In a reactor, the fission process expels neutrons with a kinetic energy of about 2 MeV per neutron compared to spallation targets, where neutrons are emitted with about 30 MeV. In the latter case, the deposited energy of an incident particle (such as a proton) into the spallation target mainly determines the amount of spalled neutrons. In case of a 1 GeV proton, about 30 neutrons are emitted with 30 MeV each. Spallation initiated by more energetic protons from faster accelerators produce larger amounts of spalled neutrons per incident proton, but do not significantly increase the energy of the generated neutrons. The de Broglie relationship equates the quantum-mechanical particle momentum $p_{QM} = \hbar k$ with the particle momentum of the classical mechanics $p_{CM} = mv$. Hence, we can relate a particle's kinetic energy E and velocity v to its wavelength λ by:

$$E = \underbrace{\frac{1}{2}mv^2 = \frac{p^2}{2m}}_{CM} = \underbrace{\frac{(\hbar k)^2}{2m}}_{QM} = \frac{h^2}{2m\lambda^2} \tag{2.2}$$

where m its mass, $\hbar$ is Planck's constant h divided by 2π, and $k = 2\pi/\lambda$ is the amplitude of the wave-vector of the particle. For measurements of the static distribution of the atoms in a solid (e.g. the crystal structure in crystalline or the average atomic distances in amorphous solids), the wavelength must be of the order of the interatomic distance, similar to Equation 2.1. In case of using neutrons as the probing medium, the particle energy has to be several tens of meV; for X-rays, this energy is in the range of several tens of keV. Measuring the dynamic distribution of atoms (i.e. measurements involving phonons) requires neutron energies of the same order of magnitude. Therefore, the neutron energy must be reduced by about seven orders of magnitude from ~30 MeV (spallation produced neutron) or 2 MeV (fission produced neutron) to ~10 meV. The kinetic energy of neutrons can only be changed by collisions with nuclei as neutrons have no charge. By guiding the neutron beam through appropriate materials like water, hydrogen or methane, the neutrons lose kinetic energy through inelastic collisions with atoms and molecules. This process is called moderation. In thermal equilibrium with the moderator medium, the neutron energies are of the same order of magnitude of thermal vibrations as the moderator atoms, and thus the neutrons may gain or lose energy. The mean energy of the neutron spectrum after the moderation process is given by:

$$E = \frac{3}{2} k_B T \tag{2.3}$$

(k_B is Boltzmann's constant, T the moderator temperature), resulting in an intensity maximum slightly lower than this energy, since the so-called Maxwellian energy distribution of neutrons after moderation is slightly asymmetric. Neutrons with energies corresponding to room temperature are called 'thermal neutrons' and exhibit the wavelengths and energies desired for investigations of atomic arrangements and phonon energies in solids, making the moderation process relatively convenient. It is remarkable that a water layer of only 2.5 cm is sufficient to decrease the neutron energy by about seven orders of magnitude.

2.1.4. **Neutron Diffraction**

As neutrons do not carry electrical charge, they interact primarily with the nuclei of matter, as opposed to X-rays that interact solely with the electron orbitals. A second interaction of neutrons with matter is through magnetic scattering from spin and orbital interactions, which is not important for this dissertation. The range of the nuclear force is about 1 fm, five orders of magnitude smaller than the wavelength of a thermalized neutron. Hence, the German Physicist and Mathematician Max Born approximated the Fermi potential of the nucleus with a point source, expressed through a Dirac function $\delta(r)$ with r being the distance between the wavefront of an incident neutron and the nucleus (Figure 2.4), resulting in the Fermi pseudo potential V:

$$V(\vec{r}) = \frac{2\pi\hbar^2}{m} b\delta(\vec{r}) \tag{2.4}$$

where m is the mass of the neutron. The scattering length b is the isotope dependent coefficient measured in meters, which is directly proportional to this scattering potential and is comprised of a coherent and an incoherent part:

$$b = b_{coh} + b_{inc} \frac{2}{\sqrt{\vec{I}(\vec{I}+1)}} \overrightarrow{s} \cdot \vec{I} \tag{2.5}$$

where $\vec{I}$ is the nucleus spin vector and $\vec{s}$ the neutron spin vector, with amplitude ½. The coherent scattering length b_{coh} is simply the average scattering length over all nuclei and the incoherent scattering length b_{inc} the deviation thereof:

$$b_{coh} = \langle b \rangle \qquad b_{inc} = \sqrt{\langle b^2 \rangle - \langle b \rangle^2} \tag{2.6}$$

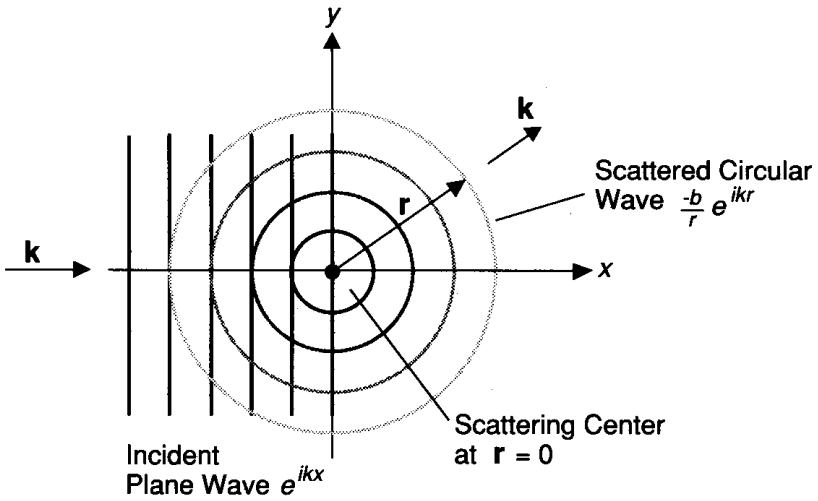

Figure 2.4: Interaction model of a neutron, described as a plane wave traveling in the x-direction, with a single nucleus, approximated as a point source. The result is an isotropic spread in a spherical wavefront with amplitude *b/r*.

where ⟨ ⟩ denotes the statistical average. Nuclei, where the sum of the nucleon spins eliminates itself ($|\vec{I}| = 0$) have a defined incoherent scattering length b_{inc} of 0. The coherent scattering length gives rise to diffraction peaks according to Bragg's law (Figure 2.5), which can be written for crystalline materials as:

$$\lambda = 2d \sin \Theta \tag{2.7}$$

where neutrons with wavelength λ reflect of lattice planes separated by d with angle θ, creating an isotope specific diffraction pattern. In contrast, incoherently scattered neutrons contribute to the 'background' and it is thus considered noise in the diffraction response.

For experiments with neutrons of constant wavelength, such as gained from a reactor source, the diffraction angle θ of Equation 2.7 is varied to obtain different lattice plane separation or d-spacing information of the sample, typically by moving the detector. As an alternative, the wavelength can be the variable when using pulsed

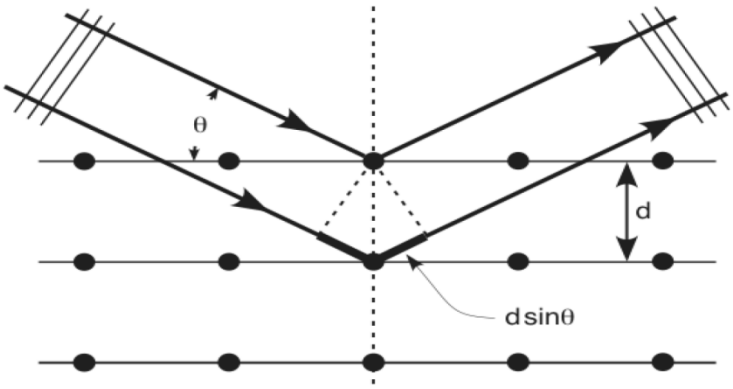

Figure 2.5: Bragg diffraction for angle θ on lattice planes separated by d, when wavelength of incident neutron meets Bragg condition.

neutrons from spallation source, as explained in section 2.1.2. Here, neutrons travel distance *L* from the source to the detector in time *t*, referred to as time-of-flight. Using the de Broglie relationship of Equation 2.2, we can substitute the wavelength λ according to Bragg's law from Equation 2.7 and derive:

$$mv = \frac{h}{\lambda} \;\Leftrightarrow\; \lambda = \frac{ht}{mL} = 2d\,sin\,\Theta \;\Leftrightarrow\; d = \frac{h}{\underbrace{2mL\,sin\,\Theta}_{const}} \cdot t \tag{2.8}$$

Thus, lattice plane separation and time-of-flight are directly proportional, coupled by the so-called diffraction constant *DIFC*. The advantage compared to a monochromatic source is that a broad spectrum of d-spacing information can be collected from a single neutron pulse, as energies and thus wavelengths and velocities of the neutrons in that pulse vary. Fast neutrons (~8000 m/s) with high energies (~300 meV) and thus short wave length (~0.5 Å) arrive first at the sample, offering information of the small d-spacing range, followed by the slower (~400 m/s) low energy (~1 meV) neutrons with larger wavelength (~10 Å) offering high d-spacing information.

As incident neutrons moderated with water at ambient conditions are not equally distributed over their energy, recorded diffraction patterns exhibit an intensity maximum around 1 Å, the center of the Maxwellian distribution. To allow a comparison of peak intensities, recorded data are normalized by dividing the recorded data with a spectrum proportional to the incident neutron intensity, resulting in a 'flat' spectrum with diffraction peaks (Figure 2.6). The energy dependent spectrum can be

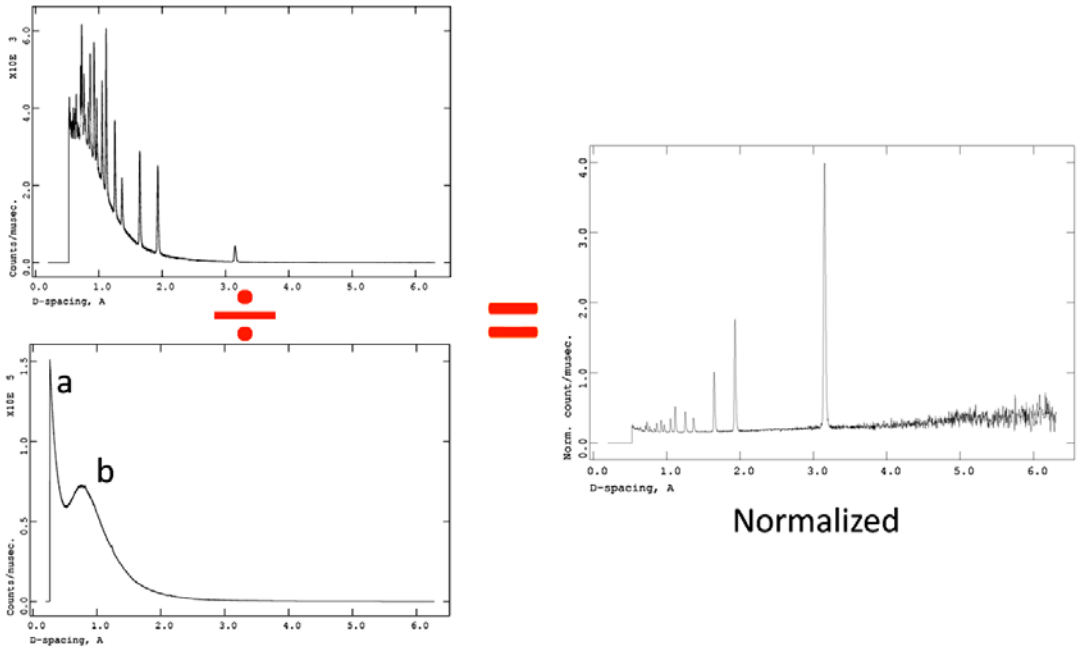

Figure 2.6: Normalization process for a typical recorded diffraction pattern (top left), which is divided by the incident neutron intensity (bottom left) to produce a normalized diffraction pattern that is used for subsequent analysis (right).

recorded utilizing a 'zero-scatterer', i.e. a material which exhibits incoherent scattering only. The coherent scattering can be annulled in a solid solution of two elements, one with a positive, the other with a negative coherent cross section, demonstrating a phase shift of π. If alloyed in the correct ratio, the structure factor annuls and only the incoherent scattering length contributes to the recorded data, resulting in a pattern directly proportional to the number of incident neutrons as a function of energy. Such a zero-scatterer is Ti-38 at% Zr [13] or V-5.1 at% Nb.

Elastic neutron scattering is considered neutron diffraction, where the incident neutrons maintain their momentum amplitude but change the direction thereof. Structural and magnetic properties of materials are probed using neutron diffraction.

In contrast, inelastic neutron scattering, where also the momentum amplitude of the incident neutrons change, allows for studying single-ion excitations, excitation gaps and dynamic processes, such as collective motion of nuclei (phonons) or magnetic moments (magnons). Neutron diffraction may be used to provide direct information on the structure of a material, the size of the unit cell, the time-averaged distribution of nuclear density within the cell and the mean thermal lattice vibrations [14].

2.2 Structural Properties of Condensed Matter

Crystal structure and texture influences the macroscopic structural properties of condensed matter and some of the basics are explained in this section. As a short note on the notation, a symbol such as 123 or hkl without brackets is understood to be a reflection, (123) or (hkl) a plane or set of planes, [123] or [uvw] a direction, {hkl} a form and $\langle uvw \rangle$ all crystallographically equivalent directions of the type [uvw].

2.2.1. Crystal structure

Atoms in matter solidify either in an amorphous manner (e.g. glass), often when the temperature changes too rapidly for the atoms to arrange in their lowest energy state, or in a periodic arrangement, a crystal structure (most metals, ceramics, rocks, etc.). A crystal structure is characterized by its unit cell, the smallest repeating unit of a crystal, consisting of atoms, ions, or molecules, whose geometric arrangement defines a crystal's characteristic symmetry. Unit cells, stacked in three-dimensional space, form the crystal lattice. There are 230 possible crystal symmetries, called crystallographic space groups. These are grouped into seven crystal systems listed in

Table 2.1. Most metals have a cubic or hexagonal structure illustrated in Figure 2.7, namely the body-centered cubic (bcc) structure with a total of two atoms per unit cell (as corner atoms are shared with adjacent cells), the face-centered cubic (fcc) structure with four atoms and the hexagonal closed packed (hcp) structure with six atoms.

Crystallographic planes within a crystal are defined using the Miller indices *hkl*. Miller indices are the reciprocals of the fractional intercepts (with fractions cleared) which the plane makes with the crystallographic x, y, and z axes of the three nonparallel edges of the cubic unit cell. In case of a hexagonal crystal structure the Miller-Bravais indices *hkil* are used, where i = - (h + k), with three basal plane axes in the (0001) plane and one vertical axis in the $(10\bar{1}0)$ plane.

The quantitative description of the probability of all crystal orientations in a polycrystal is described by the orientation distribution function (ODF), typically defined in the Euler space.

Table 2.1: Definition of the seven fundamental crystal systems.

Crystal Systems	Lattice Parameters	Lattice Angles
Cubic	$a = b = c$	$\alpha = \beta = \gamma = 90^\circ$
Tetragonal	$a = b \neq c$	$\alpha = \beta = \gamma = 90^\circ$
Orthorhombic	$a \neq b \neq c$	$\alpha = \beta = \gamma = 90^\circ$
Rhombohedral	$a = b = c$	$\alpha = \beta = \gamma \neq 90^\circ$
Hexagonal	$a = b \neq c$	$\alpha = \beta = 90^\circ; \gamma = 120^\circ$
Monoclinic	$a \neq b \neq c$	$\alpha = \gamma = 90^\circ; \beta \neq 90^\circ$
Triclinic	$a \neq b \neq c$	$\alpha \neq \beta \neq \gamma$, all $\neq 90^\circ$

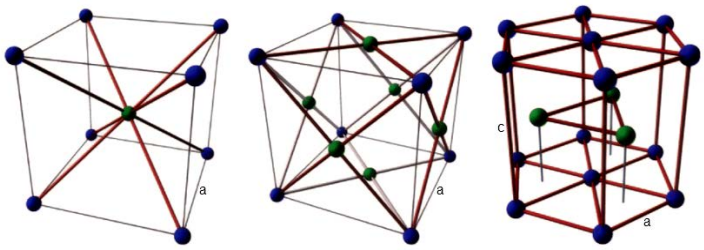

bcc fcc hcp

Figure 2.7: The Crystal structure of most metals is body centered cubic (left), face centered cubic (middle) or hexagonal closed packed (right). All sides in the shown cubic unit cells have length *a*. For clarity of the hcp structure three unit cells are shown, where atoms in the horizontal planes are separated by *a* and planes are stacked vertically by *c*/2.

2.2.2. **Texture**

Atoms within a single crystal are periodically arranged (Figure 2.8, left). Solids composed of an aggregate of single crystals are polycrystalline (ibid, middle), where the individual crystallites or grains are surrounded by a thin layer of atoms without a repetitive periodic structure i.e. in an amorphous state. Polycrystalline materials with grains not randomly oriented exhibit a preferred crystal orientation referred to as texture.

Texture is one of the characteristic features of many polycrystalline materials and, combined with the single crystal anisotropy (e.g. elastic and plastic deformation), the main cause of anisotropic physical properties of bulk solids. Texture is typically represented graphically as a pole figure (PF), inverse pole figure (IPF) or ODF plot. A PF is an equal area or, more commonly, stereographic projection of the orientation distribution of one crystallographic lattice plane. Figure

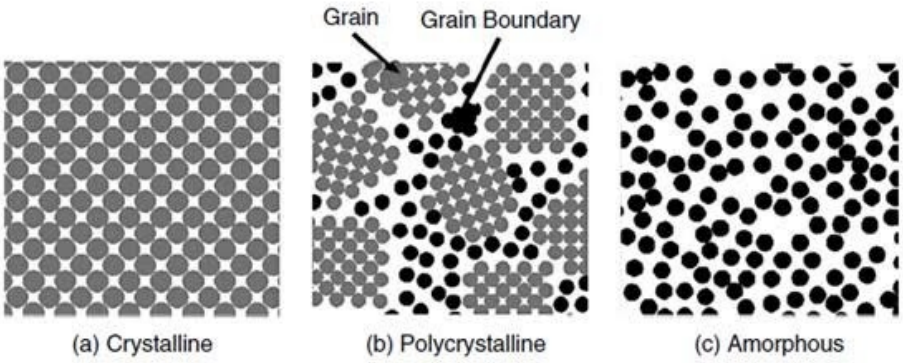

Figure 2.8: Atomic arrangement of condensed matter.

3.4 is an example of a PF plot of a deformed limestone sample, where higher intensities indicate a concentration of $(01\bar{1}2)$ and (0006) lattice planes respectively, i.e. the normal vector of these planes points more frequently to these directions resulting in a higher intensity. PFs reveal the distribution of one lattice plane into different sample directions, as opposed to IPFs, that reveal all lattice plane orientations for one selected sample direction.

The ODF itself can be depicted in a three dimensional rectangular cuboid with its Euler variables describing each of the three Cartesian axes or as two dimensional representation thereof with multiple contour maps along the third dimension. From a complete ODF all pole figures can be derived.

2.3 Electron Microscopy

To validate and complement information obtained from neutron diffraction, electron microscopy is a powerful tool. The structure of a specimen can be

investigated using a scanning electron or a transmission electron microscope, whereas its elemental composition can be characterized by an analytical electron microscope.

2.3.1. **Scanning Electron Microscopy**

Surface properties can be investigated by a scanning electron microscope (SEM) up to a magnification of 1,000,000. A focused electron beam (primary electrons) scans a specimen simultaneously in two perpendicular directions forming a rectangular area or raster. Typically, the main topological information is extracted from secondary electrons, generated in a nanometer thick surface layer of the specimen by energy transferred from the primary electrons. A modern SEM provides an image resolution typically between 1 nm and 10 nm [15].

2.3.2. **Transmission Electron Microscopy**

A transmission electron microscope (TEM) obtains a magnified image of a thin (~1 μm) specimen from penetrating electrons. These are typically accelerated by a voltage difference of 100 kV to 300kV, accelerating the electrons to 55% and 78% of the speed of light, which according to de Broglie (Equation 2.2) corresponds to a wavelength of 3.8 to 2.2 pm and allows the electrons to penetrate the μm-thick specimen. By focusing these electrons after passing through the specimen an image with spatial resolution of ~ 0.2 nm can be achieved from a modern TEM [15].

2.3.3. **Analytical Electron Microscopy**

Frequently, an analytic electron microscope (AEM) is combined with a SEM or TEM. The intensity of the backscattered primary electrons increases with heavier

elements in the specimen. Thus, the recorded image based on the backscattered electrons provides a map featuring a material dependent contrast of the specimen, where lighter areas denote materials with higher atomic number *Z*. To further analyze the elemental composition energy dispersive X-ray spectroscopy (EDX) can be employed. This radiation is generated in an atom of the specimen as a primary electron dislodges a lower orbit electron, which is re-occupied by an electron of a higher orbit, emitting the energy difference as a characteristic X-ray radiation.

2.4 Nuclear Reactors

A total of 368 GW of electrical power is generated by 435 nuclear power plants (NPPs) worldwide. The three leading countries are the United States generating 101 GW with 104 NPPs followed by France with 63 GW from 58 NPPs and Japan with 44 GW from 50 reactors [16].

2.4.1. Reactor Types

Nuclear reactors are classified by their type of nuclear reaction, moderator material, coolant, phase of fuel, use and generation [17]. The different types of nuclear reactions in a reactor are nuclear fission, on which all commercial power reactors are based, nuclear fusion which is actively pursued as a future source of power e.g. ongoing construction of *International Thermonuclear Experimental Reactor* (ITER) in France, fully operating superconducting medium-sized tokamaks, namely *Korean Superconducting Tokamak Advanced Research* (KSTAR) in the Republic of Korea and *Experimental Advanced Superconducting Tokamak* (EAST) in

China [18]. Though not yet suitable for power generation, fusion can be used for neutron production (Farnsworth-Hirsch fusors). Radioactive decay generally produces heat and power in the form of an atomic battery or a radioisotope thermoelectric generator by passive radioactive decay. Moderator materials range from graphite, water, and light element moderators (such as lithium or beryllium) to organic materials (e.g. Biphenyl or Terphenyl). As coolant in fission reactors light water (H_2O), heavy water (D_2O) or an inert gas is used. In fast breeder reactors (FBR) also liquid metal (e.g. N, NaK, Pb) or molten salt (e.g. FLiBe) in molten salt reactors (MSR) is circulated as a coolant. The phase of the fuel can be solid, fluid (e.g. nuclear salts dissolved in water in aqueous homogeneous reactor which has assumed some importance in recent years as a potential medical isotopes production system [19]) or gaseous. Gas and vapor core reactors (G/VCR) are externally reflected and moderated nuclear energy systems fueled by stable uranium compound in gaseous or vapor phase. In G/VCR systems the functions of fuel and coolant are combined and the reactor outlet temperature is not constrained by solid fuel-cladding temperature limitations. G/VCRs can potentially provide the highest reactor and cycle temperature among all existing or proposed fission reactor designs [20]. Lastly reactors are distinguished by their use, as to generate electricity, propulsion (marine or rocket), heat (domestic and industrial), transmuted elements (e.g. uranium enrichment, breeding of reactor-grade plutonium, production of radioactive isotopes for medical and industrial applications), a source of neutron radiation and positron radiation (e.g.

neutron activation analysis and potassium-argon dating), or research reactors (e.g. for materials testing).

NPP technology has evolved as distinct design generations (Figure 2.9). The first power reactors generation was introduced during the period 1950-1970 and included early prototype reactors such as the *Shippingport Atomic Power Station* in Dresden, Germany, fast breeder reactor (FBR) *Fermi I* in Michigan, USA and the magnox reactors in the UK.

The second generation included commercial power reactors built during the period 1970-1990 such as the light water cooled reactors (LWRs) with enriched uranium including the pressurized water reactor (PWR), and the boiling water reactor (BWR). It includes the Canadian deuterium uranium (CANDU®) heavy water

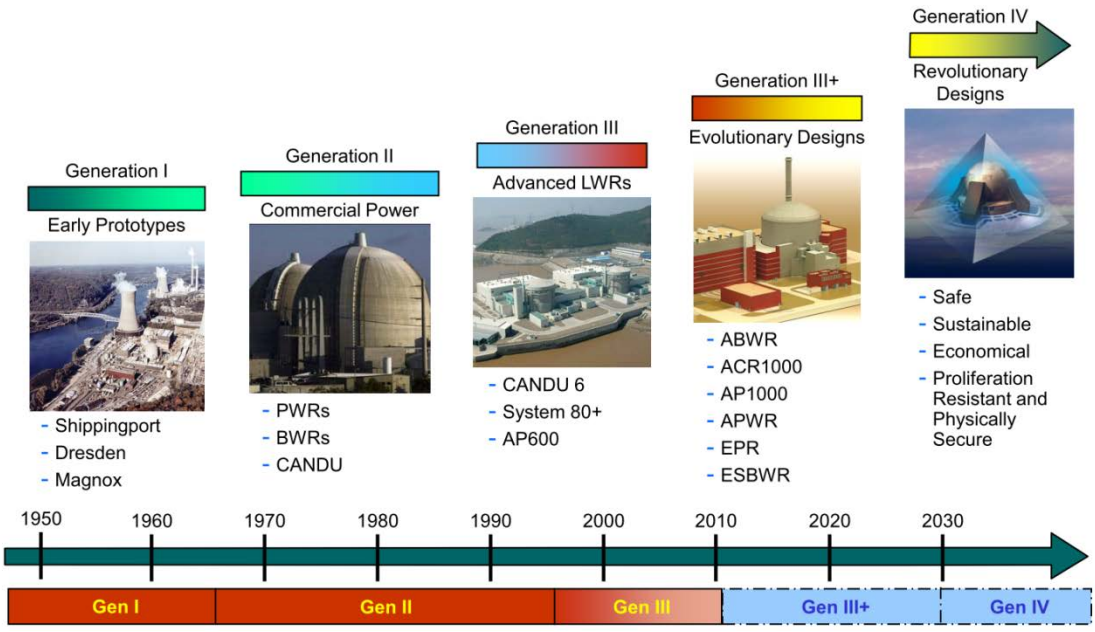

Figure 2.9: Evolution of nuclear reactors [21].

moderated and natural uranium fuelled reactors. The CANDU® reactor is a Canadian version of a pressurized heavy water reactor (PHWR), which used the heavy water as coolant and moderator. The Russian versions of second generation reactors were light-water cooled graphite moderated reactors (LWGRs), mainly the VVER-1000 and RBMK-1000. Their hard to control, positive void reactivity (the change in reactivity for 100% voiding of all coolant channels) was eliminated after the Chernobyl NPP accident, which was a LWGR. Today, 15 LWGR are in operation worldwide, all of which in the Russian Federation.

The third generation of NPPs started being deployed in the 1990s and is composed of the advanced light water reactors (ALWR) including the advanced boiling water reactor (ABWR) and the advanced pressurized water reactor (APWR). Also heavy-water reactors such as the enhanced CANDU® 6 (EC6) and the advanced heavy water reactor, using thorium fuel, belong to this generation. New designs deployed since 2010 include the advanced passive reactor AP1000 (a two loop PWR) employed in the *Sanmen* unit 1 reactor completed in 2012 in Zhejiang province, China and the advanced CANDU® reactors (ACRs) currently pending licensing in the USA and Canada. These Generation III+ reactors are considered as evolutionary designs offering improved safety and economics.

The fourth generation of nuclear reactors is expected to start being deployed by 2030. The new reactors are designed with the objectives in mind to increase economic competitiveness, enhanced safety, reduce radioactive waste generation, and secure proliferation resistance. The *Generation IV International Forum* (GIF) has been

formed out of ten countries, namely the USA, the UK, France, Japan, Canada, Argentina, South Korea, Republic of South Africa, Switzerland, and Brazil. This forum selected the following six Generation IV concepts to be developed.

The gas-cooled fast reactor (GFR) system features a fast-neutron-spectrum, helium-cooled reactor and closed fuel cycle. The high outlet temperature (~850˚C) of the helium coolant used in the GFR system makes it possible to deliver electricity (~1.2 GW), hydrogen, or process heat with high efficiency. The GFR uses a direct-cycle helium turbine for electricity generation, or can optionally use its process heat for thermo-chemical production of hydrogen. Through the combination of a fast spectrum and full recycle of actinides, the GFR minimizes the production of long-lived radioactive waste. The GFR's fast spectrum also makes it possible to use available fissile and fertile materials (including depleted uranium) considerably more efficiently than thermal spectrum gas reactors with once-through fuel cycles.

The very-high-temperature reactor (VHTR) is a graphite-moderated, helium-cooled reactor with a thermal neutron spectrum. The VHTR is designed to be a high-efficiency system, which can supply electricity and process heat to a broad spectrum of high-temperature and energy-intensive processes. The reactor core can be a prismatic block core or a pebble-bed core according to the fuel particles assembly. The reactor supplies heat with core outlet temperatures up to 1,000˚C, which enables such applications as hydrogen production or process heat for the petrochemical industry. As a nuclear heat application, hydrogen can be efficiently produced from only heat and water by using the thermo-chemical iodine-sulfur process, high-

temperature electrolysis process or with additional natural gas by applying the steam reformer technology. Thus, the VHTR offers a high-efficiency electricity production and a broad range of process heat applications, while retaining the desirable safety characteristics in normal as well as off-normal events. The basic technology for the VHTR has been well established in former high temperature gas reactors plants, such as the US *Fort Saint Vrain* and *Peach Bottom* prototypes, and the German AVR and THTR prototypes. The technology is being advanced through near- or medium-term projects lead by several plant vendors and national laboratories, such as: PBMR, GT-HTR300C, ANTARES, NHDD, GT-MHR and NGNP in South Africa, Japan, France, Republic of Korea and the United States respectively. Experimental reactors: HTTR (Japan, 30 MW_{th}) and HTR-10 (China, 10 MW_{th}) support the advanced concept development, and the cogeneration of electricity and nuclear heat application.

The supercritical-water-cooled reactor (SCWR) system shown in Figure 2.10 is a high-temperature, high-pressure water-cooled reactor that operates above the thermodynamic critical point of water (374˚C, 22.1 MPa). The supercritical-light-water coolant enables a thermal efficiency about one-third higher (45-50%) than current light-water reactors (30-35%) [22], as well as simplification in the balance-of-plant. The latter is achieved because the coolant does not change phase in the reactor and is directly coupled to the energy conversion equipment, thus steam generators, steam dryers, steam separators, etc. can be eliminated [23]. The reference system is 1,700 MW_e with an operating pressure of 25 MPa, and a reactor outlet temperature of 510 to 550˚C. Investigated fuels are uranium dioxide and uranium carbides. The

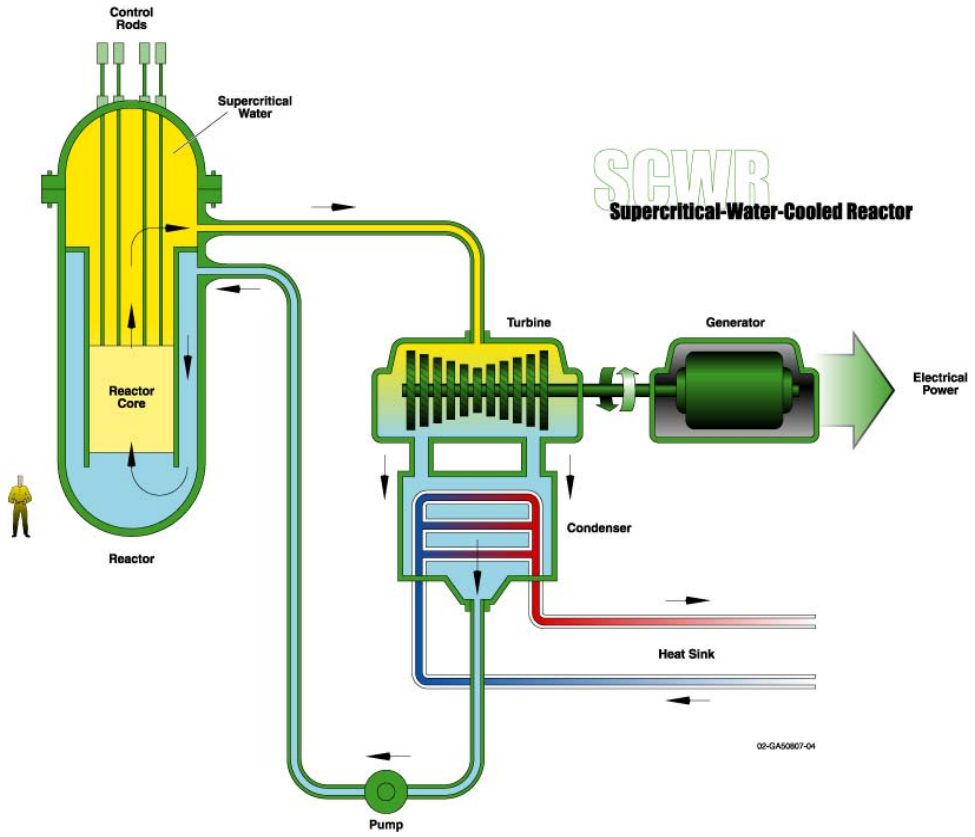

Figure 2.10: Schematic concept of a supercritical-water-cooled reactor (SCWR) [24].

SCWR system is primarily designed for efficient electricity production, with an option for actinide management based on two options in the core design: the SCWR may have a thermal or fast-spectrum reactor; the second is a closed cycle with a fast-spectrum reactor and full actinide recycle based on advanced aqueous processing at a central location.

The sodium-cooled fast reactor (SFR) system features a fast-spectrum, sodium-cooled reactor and a closed fuel cycle for efficient management of actinides and conversion of fertile uranium. The SFR is designed for management of high-level wastes and, in particular, management of plutonium and other actinides. Important

safety features of the system include a long thermal response time, a large margin to coolant boiling, a primary system that operates near atmospheric pressure, and intermediate sodium system between the radioactive sodium in the primary system and the power conversion system. Water/steam and carbon-dioxide are being considered as the working fluids for the power conversion system in order to achieve high-level performances in thermal efficiency, safety and reliability. The first option is a large size (600 to 1,500 MW_e) loop-type sodium-cooled reactor using mixed uranium-plutonium oxide fuel, supported by a fuel cycle based upon advanced aqueous processing at a central location serving a number of reactors. The second option is an intermediate size (300 to 600 MW_e) pool-type reactor and the third a small size (50 to 150MW_e) modular-type sodium-cooled reactor employing uranium-plutonium-minor-actinide-zirconium metal alloy fuel, supported by a fuel cycle based on pyrometallurgical processing in facilities integrated with the reactor. The outlet temperature is approximately 550˚C for all the three concepts. The SFR's fast spectrum also makes it possible to use available fissile and fertile materials (including depleted uranium) considerably more efficiently than thermal spectrum reactors with once-through fuel cycles. The envisaged SFR capability to efficiently and nearly completely consume trans-uranium as fuel would reduce the actinide loadings in the high-level radioactive waste it produces. Such reductions would bring benefits in the radioactive waste disposal requirements associated with the system and enhance its non-proliferation attributes.

The lead-cooled fast reactor (LFR) system features a fast-spectrum lead or lead/bismuth eutectic liquid-metal-cooled reactor and a closed fuel cycle for efficient conversion of fertile uranium and management of actinides. An important feature of the LFR is the enhanced safety that results from the choice of molten lead as a relatively inert coolant. In terms of sustainability, lead is abundant and hence available, even in case of deployment of a large number of reactors. More importantly, as with other fast systems, fuel sustainability is greatly enhanced by the conversion capabilities of the LFR fuel cycle. The LFR was primarily envisioned for missions in electricity and hydrogen production, and actinide management. The LFR concepts that are currently being designed are two pool-type reactors: (a) the *Small Secure Transportable Autonomous Reactor* (SSTAR) developed in the USA and (b) the *European Lead-cooled System* (ELSY), developed by the EC. The SSTAR is a small factory-built turnkey plant operating on a closed fuel cycle with very long refueling interval (15 to 20 years or more) cassette core or replaceable reactor module.

The molten salt reactor (MSR) system produces fission power from a molten salt fuel circulating in a fast or epithermal-spectrum reactor and contains an integrated fuel cycle. In a MSR the fuel is dissolved in a fluoride salt coolant. Prior MSRs were mainly considered as thermal-neutron-spectrum graphite-moderated concepts. MSFRs exhibit large negative temperature and void reactivity coefficients, a unique safety characteristic not found in solid-fuel fast reactors [25]. Apart from MSR systems, other advanced reactor concepts are being studied employing liquid salt

technology as primary coolant in fluoride-cooled high-temperature reactor (FHR), or intermediate coolant as an alternative to secondary sodium in sodium fast reactors (SFR) and to intermediate helium in very high temperature reactors (VHTR).

2.4.2. **Nuclear Reactor Fuels**

When short-range nuclear forces attract protons and neutrons stronger than the Coulomb forces repel the protons, a stable nucleus is formed. These rather large forces receive their binding energies ΔE (see Figure 2.11) from the mass of the nucleons according to Albert Einstein's formula relating energy to mass *m* and the speed of light *c*

$$\Delta E = \Delta m c^2 \tag{2.9}$$

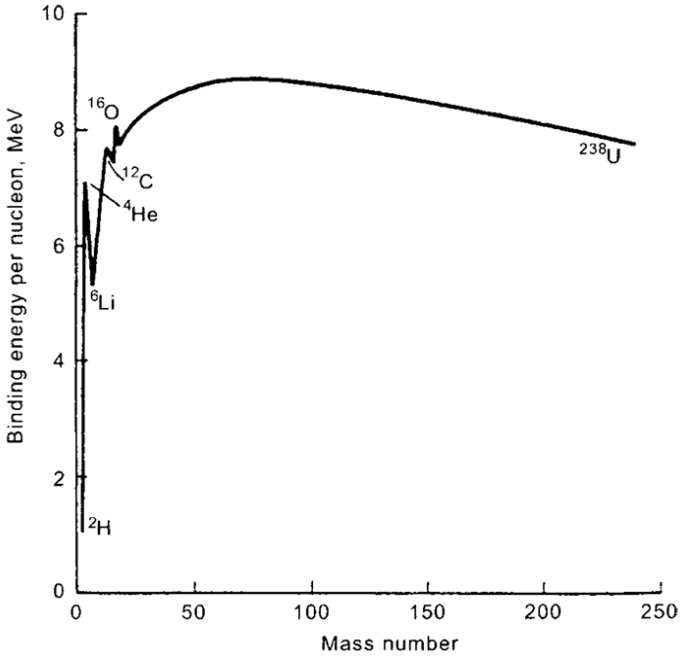

Figure 2.11: Binding energy per nucleon as a function of atomic mass [26].

Thus, the mass of a stable atomic nucleus is less than the sum of the masses of its N neutrons (m_n) and Z protons (m_p). This difference for the mass of an element ${}^{Z+N}_{Z}m$ is the mass defect

$$\Delta m = \left(Z\, m_p + N\, m_n\right) - {}^{Z+N}_{Z}m \tag{2.10}$$

In a nuclear fission process a heavy (high Z) nucleus absorbs a neutron and splits into two daughter nuclei of lower atomic number and overall lower binding energy but higher binding energies per nucleon. Uranium with 235 nuclei (^{235}U) is relatively stable with a half life of 7.1 x 10^8 years. As first recognized by Otto Hahn and Fritz Strassmann in 1938 [27], ^{235}U undergoes induced fission when bombarded with a neutron forming Barium and Krypton according to:

$${}^{235}_{92}U + {}^{1}_{0}n + 5MeV \rightarrow {}^{236}_{92}U^{*} \rightarrow {}^{144}_{56}Ba + {}^{89}_{36}Kr + 3\ {}^{1}_{0}n + 172MeV \tag{2.11}$$

As other fission products are possible, a split with mass ratio of 3:2 is most common [28]. The uranium forms an excited state for about 0.1μs before breaking apart. Some isotopes such as ^{233}U, ^{235}U and ^{239}Pu are called fissile as they exhibit a smaller activation energy than the binding energy of a neutron which allows fission using relatively low energy neutrons (≥1 MeV) [28].

The amount of neutrons n being emitted during the fission process depends on the fissioning nuclide and on the energy of the neutron inducing fission (Figure 2.12). For an average of three neutrons to be emitted in the fission process the incident neutron has to collide with 5 MeV in kinetic energy. The available energy of 172 MeV after the fission process originates from the mass defect plus the original 5 MeV

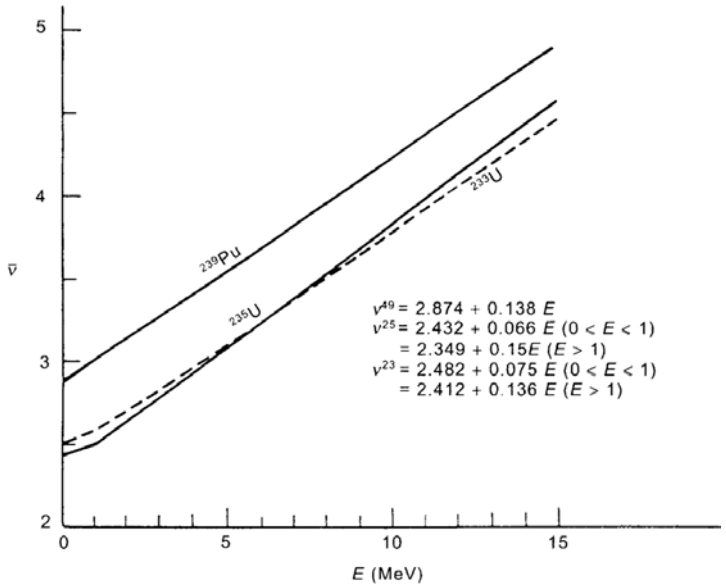

Figure 2.12: Average number of neutrons emitted per fission [29].

of the incident neutron. Subtracting the atomic mass of the fission products ^{144}Ba with 140.9144064 ± 8.8E^{-6} u, ^{89}Kr with 91.9261528 ± 12.9E^{-6} u and three neutrons with 1.0086649 ± 0 u from our starting material ^{236}U with a mass of 236.0455619 ± 2.2E^{-6} u, we are missing 0.179008 ± 23.8E^{-6} u, or 2.9725E^{-28} ± 3.952E^{-32} kg which according to formula (2.9) corresponds to a energy of 166,744.88 ± 22.2 keV. Further, energy is released from the decay of the fission products, which emit electrons with a total of 8 MeV and neutrinos with 12 MeV. The kinetic energy deposited into the neutrinos escapes the system due to their rare interaction with matter. The rest of the released energy is transferred into kinetic energy, about 93% of which to the fission products, about 4% into gamma radiation and the remaining 3% into emitted neutrons. Thus the resulting neutrons obtain on average about 2 MeV each and are capable of starting a fission reaction in turn, creating a chain reaction.

The fission products tend to be neutron-rich and subsequently decay by beta or neutron emission and undergo transmutations via beta decay into a heavier isotope, which further decays and transmutes. Beta decay can be seen as the decay of one of the neutrons to a proton via the weak interaction, whereby one of the 2 down-quarks is transformed into an up-quark and a virtual W^- boson, which decays within the allowed time frame of the uncertainty principle into an electron and an electron antineutrino.

Nuclear power plants operate with different fuels containing fissile elements such as plutonium, uranium, or thorium. Reactor-grade plutonium contains 50-60% fissile ^{239}Pu. Uranium fueled reactors utilize fuel developed from natural uranium containing a mixture of ^{234}U, ^{235}U and ^{238}U, with the fissile ^{235}U content carrying from 0.72% (naturally occurring uranium) to more than 90%, depending on the enrichment. When the uranium fuel stems from a recycling plant it will also contain various isotopes produced in the transmutation-decay process of uranium, such as neptunium, plutonium, and americium. Thorium fueled reactors will contain ^{232}Th and ^{233}U or ^{235}U and, if the fuel is from a reprocessing plant, isotopes produced in the transmutation-decay process of thorium, such as protactinium, uranium, and neptunium.

In general, the primary fuel choice is enriched uranium dioxide (UO_2). The temperature of the nuclear fuel elements is about 530 - 1530°C in a FBR, and ~280 - 1530°C in a LWR [30]. The industry accepted limit for the fuel centerline temperature is 1850°C [22], [23]. Previous studies have shown that the maximum fuel

centerline temperature of a UO_2 pellet might exceed this industry accepted limit at SCWR conditions [23]. Therefore, alternative fuels with higher thermal conductivities need to be investigated for SCWR use. Uranium monocarbide (UC), uranium nitride (UN), and uranium dicarbide (UC_2) are excellent fuel choices as they all have higher thermal conductivities compared with conventional nuclear fuels such as UO_2, ThO_2 and mixed oxides (MOX) [23]. UC is an important ingredient in the Indian nuclear fuel program [31]. In Fast Breeder Test Reactor (FBTR), Kalpakkam, India; UC–PuC mixed carbide fuel has been used extensively for the last 15 years. Initially the FBTR was made critical with Mark I fuel (30%UC + 70%PuC) and afterward, it was continuously fueled by Mark II (45%UC + 55%PuC) with the expansion of the FBTR core. Another important application of uranium carbides is as a target material to generate a heavy ion beam in particle accelerators [31].

3.0 EXPERIMENTAL TECHNIQUES

In this chapter, I present the neutron diffractometer HIPPO as the selected experimental approach to investigate nuclear materials. All sample environments of Chapter 4.0 are designed to operate in conjunction with HIPPO and resulted in the experimental findings described in Chapter 5.0 and 6.0. The Rietveld approach to analyze structural properties of condensed matter (introduced in section 2.2) and a Java™ program that I developed to visualize results are explained. The concluding section points out limitations of the neutron diffraction technique and their implications regarding sample alignment.

3.1 HIPPO Diffractometer

The *High Pressure – Preferred Orientation* (HIPPO) diffractometer [11], [32], located in the Experimental Room-1 (Figure 3.1), is one of 15 instruments at LANSCE. Details of the high intensity, neutron time-of-flight (TOF) diffractometer HIPPO, with a total detector area of 4.9 m^2 and an accessible d-spacing range of 0.12-24 Å, are reported in [11], [32]. I briefly summarize the instrument and a recent detector upgrade. Relativistic 800 MeV protons generated by the 800 m linear accelerator spall off neutrons in the *1L* tungsten target. At a short distance of ~8.83 m from the water moderator, a high neutron flux of $1.12 \cdot 10^7 \frac{n}{cm^2 s}$ [10] constricted to a beam diameter of 10 to 14 mm interacts with the sample in HIPPO and is detected by 1200 ^{3}He tube detectors. The detector configuration has been updated in 2011. Now, the detector tubes are mounted on 53 panels with 12, 24 or 32 tubes each. The panels

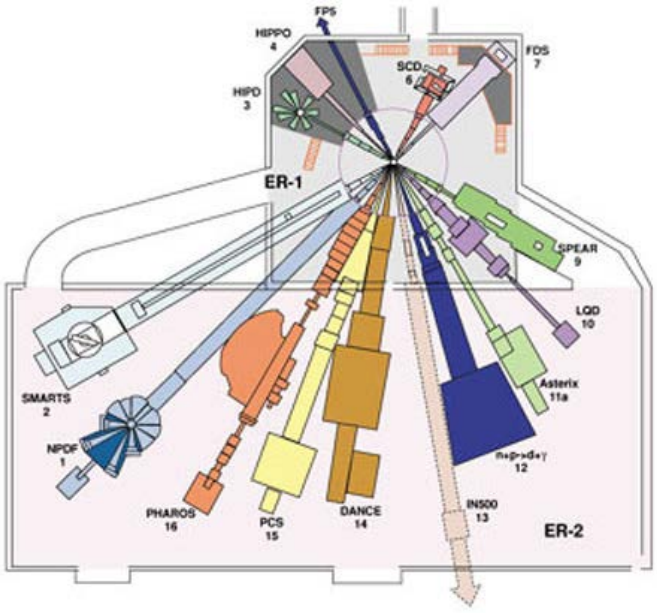

Figure 3.1: Experimental Room 1 (ER-1, top) and ER-2 (bottom) of the LANSCE user facility, showing 15 available neutron instruments surrounding the spallation target.

are arranged on six rings around the incident beam direction with nominal diffraction angles $2\theta = 40^{\circ}$, 60°, 90°, 120°, and 145° (Figure 3.2). A software routine merges the 16 detector panels of the 145° ring to eight histograms, resulting in a total of 45 histograms per data collection run for the refinement process in case of texture experiments. Histograms from the panels measured at typically three to four sample rotations around the vertical axis result in up to $4 \cdot 45 = 180$ unique histograms. Based on these histograms the ODF or texture of the sample can be reliably derived by using a Rietveld software package. For samples with no or mild preferred orientation, the 53 panel are merged to five histograms representing the detector rings, allowing rapid data collection for powder diffraction.

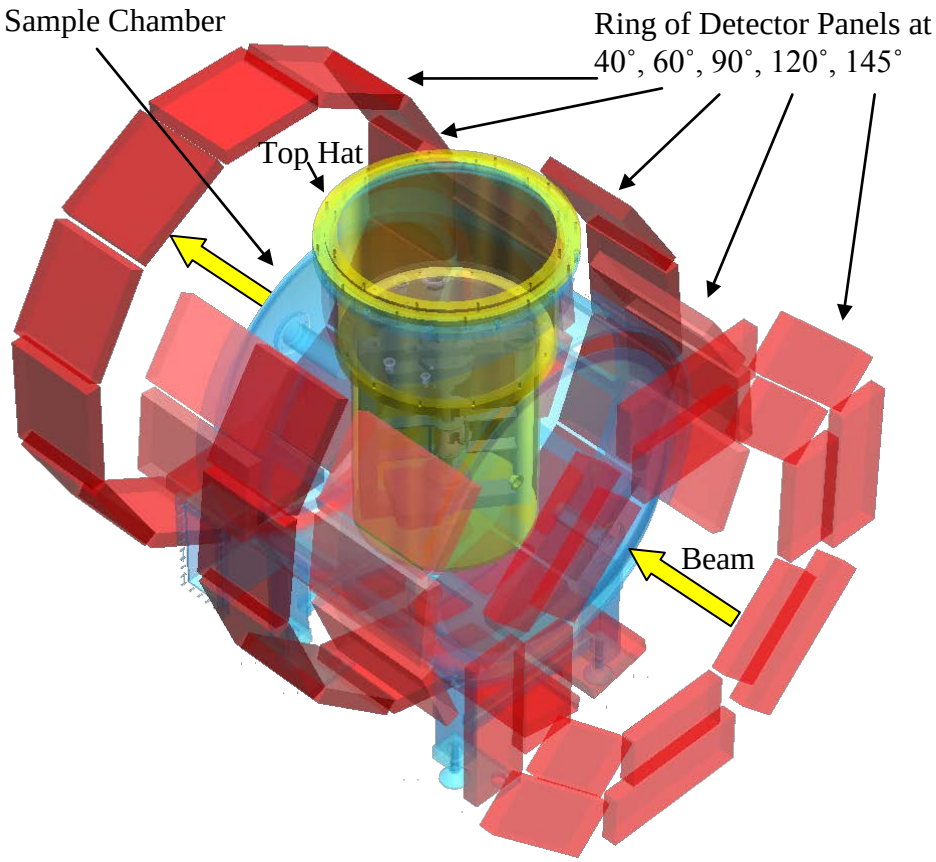

Figure 3.2: Schematic of the HIPPO neutron diffractometer with top hat (yellow) inserted into the HIPPO vacuum chamber (blue) surrounded by detector rings (red). The total length from the 145˚ back-scattering detectors to the 40˚ detectors is 2.2 m; the outer diameter of the back-scattering detectors is 1.85 m.

The large sample chamber of HIPPO is built to accommodate a variety of sample environments. This ancillary equipment is generally mounted in a so-called 'top hat' that mates with the HIPPO flange, an opening 60 cm above the neutron beam centerline with a standardized diameter of 75 cm [11]. This standardization allows interchange of ancillary equipment with other LANSCE beamlines; aside from HIPPO also NPDF (*Neutron Powder Diffractometer*), SMARTS (*Spectrometer for*

Materials Research at Temperature and Stress), and the inelastic neutron scattering instrument *Pharos*. Available sample environments include but are not limited to cryogenic equipment (displex system capable of ca. 10–300 K), ILL vacuum furnaces (300–1500 K), a toroidal anvil high-pressure cell (30 GPa and 2000 K), a kappa geometry 3-circle goniometer and a load frame [11].

3.2 Data Analysis

Recorded neutron time-of-flight (TOF) data are analyzed using the Rietveld method [33], [34]. A complex function with ~10-100 parameters approximates the recorded data incorporating instrument specific parameters, e.g. incident intensity, background, count time, and sample specific parameters, such as lattice parameters, atomic position, thermal motion, site occupation, phase fraction, texture and absorption. Neutron TOF peak profiles are somewhat different from constant wavelength neutron or X-ray data [35], therefore, specialized peak profiles have to be available in the software. I used available Rietveld packages such as the General Structure Analysis System (GSAS) [36], [37], [38], which allows to analyze larger data sets when combined with the gsaslanguage [39], and the platform independent Materials Analysis Using Diffraction (MAUD) [40], [41], [42]. A detailed step-by-step description on a streamlined texture analysis using MAUD has been published in [43]. Other options such as FullProf [44], [45] or Topas [46], [47] are available. In MAUD texture is analyzed by the E-WIMV algorithm [43] which is based on the direct methods approach of WIMV (i.e., not Fourier space), but has been modified for

maximum entropy optimization. Phonons (i.e. thermal lattice vibrations) are described in GSAS by the isotropic thermal motion parameter U_{iso} which is the mean square displacement of the atoms with unit $Å^2$ and correlated to the isotropic *B-factor* in MAUD by

$$B = 8\pi^2 U_{iso} \tag{3.1}$$

The validity of the applied procedure for texture analysis has been established by measuring a texture round-robin sample and the resulting agreement with other measurements [3], [11].

3.3 Data Visualization using pod2k

After the refinement process, a sample texture can be visualized as pole figure plots with the freely available cross-platform Java™ program *pod2k* [48] developed by the author. Compatible input formats are the standard popLA format as detailed by Kallend et al. [49] or a plain three column format representing azimuth, tilt, and intensity as frequently used by self-consistent models [50], [51]. I use the open GNU licensed software GMT (General Mapping Tool) [52], [53], [54] within pod2k to render the texture as a color-coded pole figure plot. Up to six publication quality pole figures per page are plotted and saved in Postscript format. Additional file outputs via conversion using Ghostscript [55] are PDF, JPEG, PNG and BMP with resolutions scalable between 100 and 600 dpi.

An intuitive GUI (Figure 3.3) allows modifying the plot layout, scale range, output format as well as selecting and previewing color schemes. The latter can be manually overwritten with a fixed value e.g. for comparing multiple plots at the same scale. Aside from the Miller indices *hkl* and the scale, values for both minimum and maximum intensity of each pole figure can be selected for plotting. For hexagonal crystal structures the Miller indices can be modified to appear in the Bravais-Miller form *hkil* on the plot including bars for negative directions. Labels specifying the sample direction (e.g. rolling, normal, or compression direction) can be plotted at 12 and 3 o'clock of the first pole figure. Available azimuthal projections are Lambert equal-area and stereographic projection. Pole figures including all layout options can also be plotted by command line allowing for scripts to process numerous plots

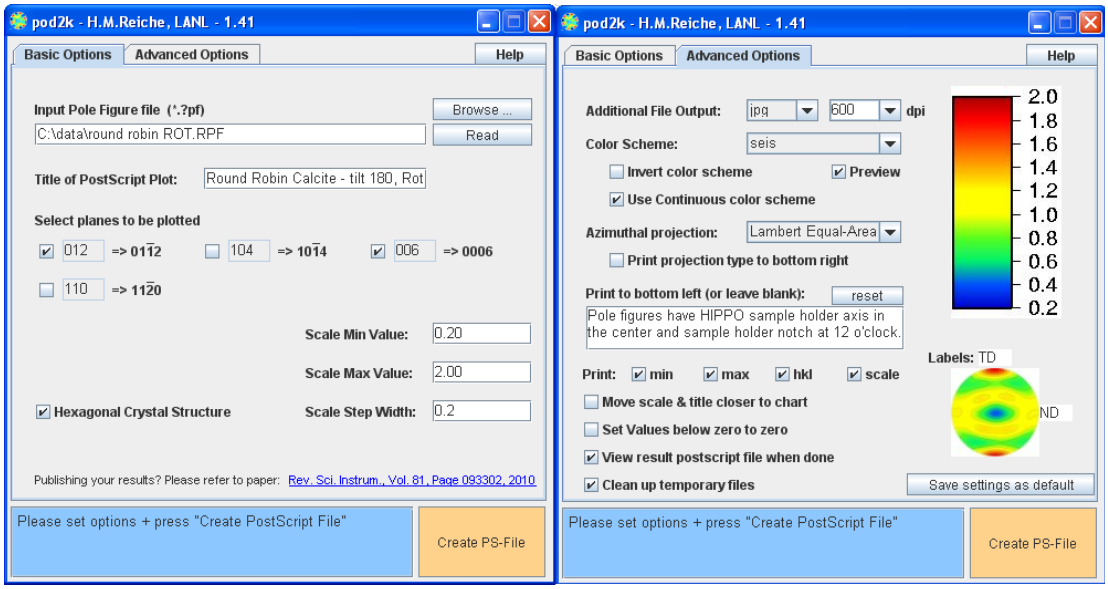

Figure 3.3: GUI of pod2k a cross-platform software to create high quality pole figure plots showing basic option tab (left) and advanced option tab (right).

without user interference. Figure 3.4 shows the round-robin limestone standard [11] rotated with popLA by 31.6˚ clockwise and plotted with pod2k Version 1.41.

3.4 Sample Alignment

With time-of-flight neutron diffraction relative changes in the lattice parameter can be determined rather precisely, as can be seen by the small standard deviation (Table 5.2) which is calculated by MAUD. On the other hand, absolute lattice parameters cannot be easily extracted from neutron TOF experiments, based on sample alignment and variation in center of diffraction [57]. If we split the distance *L* that a neutron travels in Equation 2.8 into the distance from source to sample L_0 and

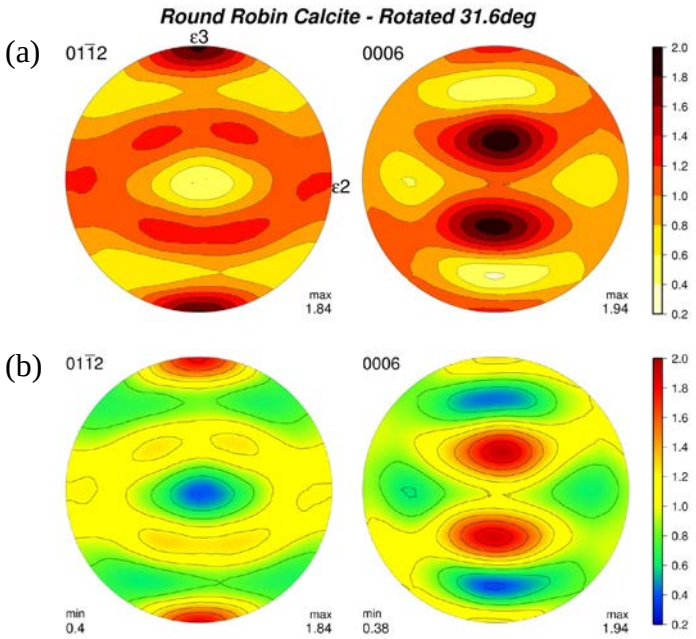

Figure 3.4: Pole figures generated from experimental data of the round-robin sample (deformed limestone) with strain directions according to Fig. 5 in [56] plotted with pod2k showing (a) equal area projection, color scheme ‘hot’, (b) stereographic projection, color scheme ‘seis’, continuous scale, min, max values and *hkil*.

sample to detector L_1 we obtain:

$$d = \frac{h}{2m(L_0 + L_1)sin\theta} t \tag{3.2}$$

When a sample is displaced from its calibrated position the variables L_0, L_1 and θ change. For a displacement x along the incident beam path, we can modify [57] the above equation to:

$$\frac{\Delta d}{d} = \frac{\Delta t}{t} = -x\left(\frac{1 - cos2\theta}{L_0 + L_1} + \frac{sin2\theta}{2L_1 tan\theta}\right) \tag{3.3}$$

Considering the dimensions of the HIPPO diffractometer at a distance of L_0=8.83m from the neutron source, a misaligned sample would result in reflection shifts recorded in Table 3.1. For example, a sample aligned within 0.1 mm of the calibration sample would cause the recorded lattice parameters to shift by 0.001 Å in the 60˚

Table 3.1: Shift in d-spacing (Δd) for the five detector banks of the HIPPO diffractometer if the sample is misaligned from the calibrated position by 1 mm towards the neutron source. L_1 denotes the center-to-center distance between sample and active detector area.

Detector (2θ)	145˚	120˚	90˚	60˚	40˚
L_1	1.216m	0.811m	0.864m	0.811m	1.245m
d in Å	**Δd in Å**	**Δd in Å**	**Δd in Å**	**Δd in Å**	**Δd in Å**
0.5	0.0013	0.0023	0.0034	0.0049	0.0037
1.0	0.0026	0.0046	0.0068	0.0098	0.0073
3.0	0.0077	0.0139	0.0205	0.0293	0.0220
5.0	0.0128	0.0232	0.0341	0.0488	0.0366
10.0	0.0255	0.0464	0.0682	0.0977	0.0732

detectors of HIPPO for a reflection expected at 5 Å, one order of magnitude larger than the uncertainty shown in this work. Even a perfectly aligned sample will have a neutron cross section other than that of the calibrant which will cause the diffraction center to shift easily on the order of ±1 mm, resulting in lattice parameter shifts of 0.01 Å. Therefore, any absolute lattice parameters obtained with neutron diffraction needs to be calibrated with another technique such as X-rays. It is further imperative for any sample environment encompassing motion control to position the sample with high repeatability, e.g. back to its origin after a sample rotation. When sample environments are built to simulate extreme conditions, they are typically larger in order to isolate the surroundings from the extreme condition and thus, exhibit long sample sticks to position a specimen in the beam position. The High-Temperature Furnace presented in section 4.3 is a good example for this scenario, as only a small tilt of the sample stick head causes a significant translation of its tip. Therefore, an image plate can be used to verify the sample position. Also, during commissioning of sample environments, it is helpful to use such an image plate to identify the beam position relative to nearby materials, such as shielding.

Image plates are based on the effect of delayed luminescence as a result of X-ray irradiation. The material used as a phosphor for the image plate is the alkali-earth halide $BaFBr:Eu^{2+}$. A thin layer of ^{157}Gd can be used to absorb and transform the energy of incident neutrons into X-rays. An overview of its mode of operation is given in Figure 3.5. An example of a recorded image is shown in Figure 3.6 which was taken during a maintenance period of the linear accelerator, thus without neutron

beam. The activated spallation target emitted sufficient γ-rays to record the sample position.

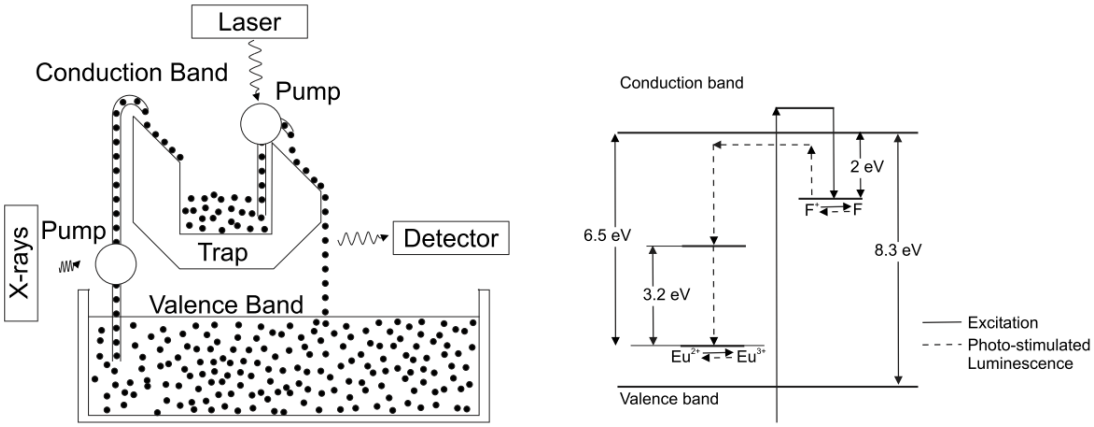

Figure 3.5: Schematic of photostimulated luminescence (left, [58]) and their utilized energy levels (right, [59]) using an image plate.

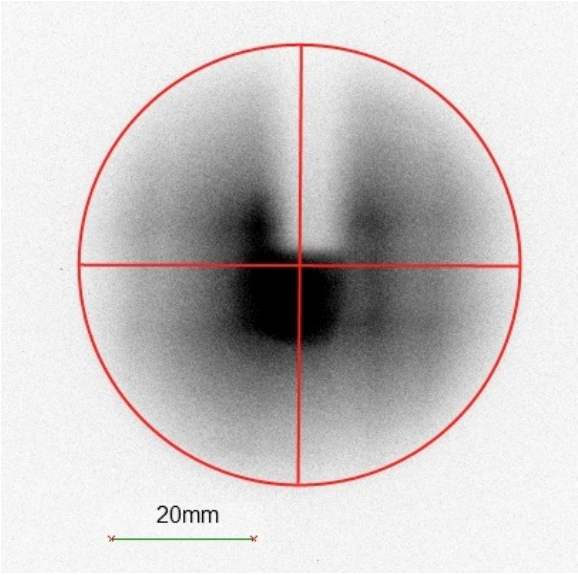

Figure 3.6: Recording of an image plate to align the sample position. A suspended lead sample (white, top) blocked incident γ-rays. The crosshair denotes the center of the neutron beam.

4.0 SAMPLE ENVIRONMENTS

In this section three sample environments for *in situ* neutron diffraction studies are described which provide information regarding crystallographic structure and texture of nuclear materials. I adapted a sample changer for reliable and fast automated texture measurements of multiple specimens. I built a creep furnace combining a 2700 N load frame with a vanadium element resistive furnace, capable of temperatures up to 1000˚C, and manipulated by a pair of synchronized rotation stages. This combination allows following deformation and temperature dependent texture and strain evolutions *in situ*. Lastly, I developed a resistive graphite high-temperature furnace with sample motion for *in situ* crystal structure and texture measurements of nuclear materials at steady-state temperatures up to at least 2200˚C. This permits *in situ* observation of e.g. phase transitions and coefficients of thermal expansion, as well as phase formation and texture development during solidification. These sample environments have been successfully commissioned and integrated into the user program of the HIPPO (section 3.1) diffractometer at the LANSCE user facility.

4.1 Sample Changer

An automated sample changer [48] with an Eulerian cradle for neutron texture measurements is described. I optimized this device, which has been measuring over 2300 texture and almost 400 powder samples at ambient conditions since it became operational in 2002 for use in the HIPPO diffractometer. Operation for almost a

decade resulted in sustained enhancements of mechanics, electronics, and software, which significantly improved reliability and resiliency.

4.1.1. **Motivation**

Short counting times per sample on modern neutron diffractometers allow for high sample throughput. In order to optimize the usage of available neutron flux and reduce the instrument downtime due to closing and opening of shutters, as well as alignment of samples, automation for sample changes is essential. This also reduces the workload of beamline personnel greatly, since count times for texture measurements of e.g. steel samples on the HIPPO instrument at LANSCE may take as little as one minute of beam time.

Several automated sample changers for neutron diffraction measurements are described in the literature: For neutron diffraction, a twelve-position carousel sample changer for beam-lines at ISIS, capable of sample temperatures between 20 and 150ºC, was described by Shah [60]. For the beamline POWGEN-3 at SNS, a 24-can sample changer capable of cryogenic temperatures of ~10 K, was portrayed by Rix et al. [61]. None of these instruments are used for routine texture measurements and therefore, none of the sample changers allows for a re-orientation of the sample in the beam position for texture measurements or probing different sample volumes in elongated samples.

The present work was focused on automating the measurements for which HIPPO was designed: the study of preferred crystal orientation or texture and powder

measurements. Texture is one of the characteristic features of many polycrystalline materials and, combined with the single crystal anisotropy (e.g. elastic and plastic deformation), the main cause of anisotropic physical properties of bulk solids [51], [62]. Texture measurements on HIPPO take advantage of its large number of detectors which record intensities from differently oriented crystals satisfying Bragg's law. In combination with the time-of-flight technique, inverse pole figures are recorded for many sample directions simultaneously, allowing for a determination of the orientation distribution for a given sample. The key feature of HIPPO for this kind of measurement is that sample rotation around a single axis is sufficient in order to obtain data to determine the orientation distribution function. The common approach on other neutron or X-ray diffraction beamlines is to rotate the sample on a goniometer around two axes. Therefore, the combination of this improved sample changer, published by Reiche and Vogel [48], and the HIPPO diffractometer accomplishes efficient, i.e. with a minimum of beam time, texture measurements.

Throughout the initial years of operation mechanical problems as well as control predicaments have emerged. Mechanical misalignments lead to sample gripping problems or even crushing of costly custom-built vanadium sample cans. The latter has to be avoided especially when a sample can is filled with radioactive powder as the HIPPO chamber would become contaminated. Powder samples are contained in vanadium because of its very low coherent cross section of 0.0184b. Insufficient software exception handling and communication issues demanded high supervision of the system. Maintenance and repair of sporadically defective hardware was time

consuming as custom device firmware had to be uploaded into the replacement manually. Thus, expensive neutron beam time was lost which lead to the necessity to refurbish the entire system. I performed the general system upgrade as described.

4.1.2. **Mechanical Design**

The sample changer hardware was originally designed and manufactured by ZYGO/Square One Systems Design [63], [64] with the control software developed entirely at LANSCE. Since delivery in 2001, numerous modifications have been incorporated. Actuators and sensors have been upgraded to optical home switches, video signal feedback and motion control torque limiters have been installed. All electronic devices (motion control, network switch etc.) are mounted on top of the sample changer, such that only the power and network cable have to be connected for operation, allowing setup of the sample changer in HIPPO within a few minutes. In practice, this allows the utilization of even short amounts of beam time, e.g. one hour, with the sample changer while other experiments are set up.

The geometric configuration of sample changers is likely to be instrument specific [65], sometimes even inextricably build into a neutron diffractometer [66]. By standardizing both the flange of the sample wells and the beam position relative to that flange, this sample changer, like many other sample environments at LANSCE, fits into four different instruments; aside from HIPPO also into NPDF (*Neutron Powder Diffractometer*), SMARTS (*Spectrometer for Materials Research at Temperature and Stress*), and the inelastic neutron scattering instrument *Pharos*.

Limiting the radial size of the sample changer is the 73.7 cm (29 inches) diameter opening of this standard flange on top of HIPPO's sample chamber (Figure 3.2) on which the base plate (Figure 4.1) of this sample changer rests. In order to minimize weight, aluminum was employed to create a framework on which the sample can be lowered form the tray 0.7 m into the beam position. The frame design minimizes the amount of attenuating material in the path of the diffracted beam.

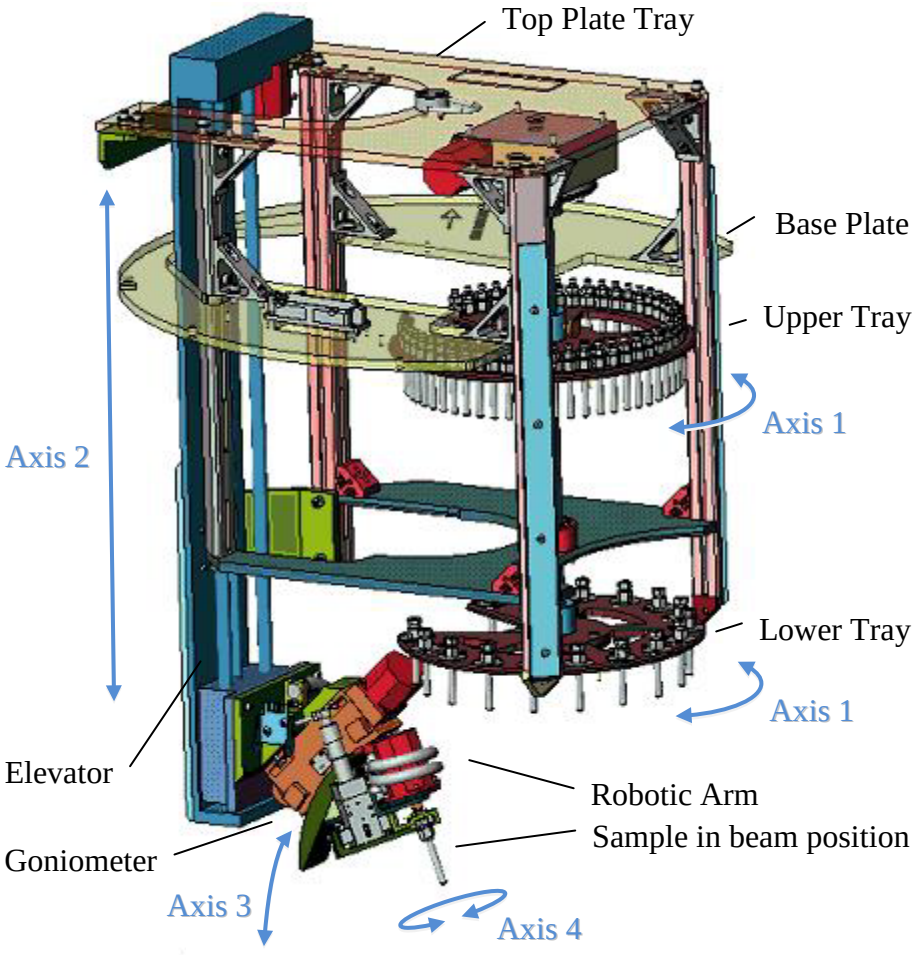

Figure 4.1: Sample changer design without electronics mounted on top. Figure originally published in my paper [48].

Electronics, especially semiconductors, on the other hand, were distanced from the beam in order to prolong their lifetime and were placed on the top plate (Figure 4.1) of the sample changer, also making it more accessible for maintenance. The original design had electronics in a separate rack-mounted casing, which turned out to make setup and maintenance more complicated, as large amounts of cables had to be moved when the sample changer needed to be worked on outside the beam. Borated silicone [67] mounted underneath the top plate reduces the risk of radiation damage to motion control electronics by scattered thermal neutrons. In the five years of operation in this mode we did not observe an increased failure frequency as compared to components kept outside the HIPPO instrument from the direct beam. Hence, no failure could be unambiguously related to radiation damage.

The sample changer features four motion axes as shown in Figure 4.1. The components are as follows: 1) Up to two horizontal sample trays on a vertical rotation axis, 2) 820 mm vertical travel range of an elevator holding 3) a ±20° goniometer [68], moving around the horizontal axis, with 4) the sample gripper attached to it, which can spin the sample 245° around its vertical axis. The third and forth perpendicular axes form an Eulerian cradle with a limited angular range. Optical and proximity sensors are used to establish reference points for home and beam positions as well as end of travel limits. A commercially available Compumotor 6k4 from Parker [69] was selected as the motion controller, directing four ‘Compumotor Zeta 4’ drivers, one for each motion axis. The linear motion sample gripper [70] is electrically actuated and has position feedbacks for the open and closed position. The

trays are interchangeable for powder samples (50 samples, tray hole diameter 10 mm) and texture samples (16 samples, tray hole diameter 37 mm). We decided that the tray with the larger hole diameters, originally designed for texture samples only, provided a higher tolerance for mechanical uncertainties. Therefore, this tray-type is now also used for powder samples loaded in vanadium cans. With the old configuration, due to the difference of only 1 mm between sample can diameter and tray hole diameter, even slight misalignments resulted in costly damage of vanadium cans, in addition to possible contamination of the instrument depending on sample composition and the amount of damage done.

The motion sequence to transport a selected sample into the beam position starts with a rotation of the trays in order to position the desired sample underneath the gripper. The elevator then lowers the gripper which in turn grabs the head of the sample. Next, the elevator lifts the gripper, now with the sample attached, back up. Then, the tray rotates back to its home position, which places a slit in the tray under the gripper, allowing the elevator to lower the gripper past the tray to the beam position. As soon as the required histograms are recorded, the sample is returned to its original slot in the tray via the reverse motion sequence and the next sample is measured.

The sample changer accommodates various bulk sample dimensions, ranging from ~1 mm^3 specimens glued on vanadium cans to single phase [11], [71], [72] and complex multi-phase [73], [74], [75] samples between 0.1 and 1 cm^3. The maximum sample diameter is limited to 37 mm by the tray hole and 195 mm in length restricted

by the maximum lifting height of the gripper above the tray. However, larger samples can be manually mounted. In order to define the volume irradiated by neutrons, the sample can be lowered by 22 mm or raised by 300 mm relative to the beam position, allowing the probing of different volumes of the same sample. Longer and wider samples like plutonium samples [76], which require a bulky safety encapsulation can be manually loaded without using the trays. To probe different sample directions, the sample is rotated about the vertical axis to, typically, three to four orientations in order to analyze its texture [41].

Texture samples are typically glued to the flat end of a 35 mm long, 9 mm in diameter aluminum rod wrapped in cadmium sheet. Cd absorbs thermal neutrons due to its high absorption cross-section of 2520 b (1 b = 10^{-28} m^2), hence, preventing diffraction from the sample holder. The head of the sample holder, to which the gripper attaches, is a custom machined Al piece (Figure 4.2). A notch aligns the vertical rotation with the sample changer tray and, therefore, references the sample orientation with the instrument for texture measurements. During a measurement, the

Figure 4.2: Up to 16 of these sample holder heads made of aluminum can be placed in a tray for sequential sample measurements. The alignment notch shown left ensures repeatability of the sample position. A sample can be attached using the standardized 10-32 screw hole shown on the bottom. Figure originally published in my paper [48].

angle between the notch and the transmitted beam spans 61.7˚. This angle needs to be included into the data analysis to obtain pole figures with e.g. rolling directions at the top of the pole figure [11]. The sample holder head has a No. 10-32 thread in the rotation center for mounting either the aforementioned Al rods or 69 mm tall vanadium cans of 6.4 mm (1/4 in.) or 9.5 mm (3/8 in.) with the same threads in their end-caps as used for displexes and furnaces at LANSCE. This concept proved rather useful as special sample holders can be readily fabricated, e.g. by simply gluing a nut on the sample holder head to hold a threaded sample. Bulky or heavy specimens can be clamped or screwed into special fixtures attached to the No. 10-32 thread of the sample holder head.

The only required mechanical maintenance is an annual application of grease to both the linear bushings of the elevator and the rotary bearings of the vertical tray rotation axis.

4.1.3. **Software Design**

I developed robust control software at LANSCE using LabVIEW. This software interfaces with the sample changer hardware and provides EPICS [77] channels for the main data acquisition (DAQ) computer in order that diffraction data can be accumulated up to a specified integrated beam current before a sample is rotated or returned. In the initialization routine, all customized motion control parameters such as scale factors and velocities are transmitted to the motion controller, allowing for quick ‘Plug and Play’ exchange of sporadically defective hardware. A self-diagnostic

routine identifies common errors (i.e. communication problems, motion misalignments) and attempts to mitigate them. If these automated attempts fail, a series of solutions is suggested to the users, effectively decreasing possible down time due to such problems.

Typically, the LabVIEW program is remotely controlled by a Perl script which runs on HIPPO's main DAQ computer and processes a simple text file with details of the current batch of samples (run titles, user proposal information, count times and orientations), allowing to mix samples for powder and texture measurements arbitrarily. During normal operation, the user is assumed to be away from the local screen and, so the LabVIEW program will send a message to a pager and/or cell phone via email to communicate occurring issues that are not fixable without human intervention. The status of the sample changer is also tied into the instrument status web page for routine monitoring.

Our latest version incorporates real time image analysis and resilient sample sequencing. When samples are taken out of the tray a *Pepperl & Fuchs* camera [78], with integrated image analysis capabilities, provides feedback regarding the position of the sample holder, its orientation, or detects slots in the tray that were accidentally left empty. Furthermore, a picture is archived from each sample to document sample type, shape, orientation and programmed beam height offset in a database. Resiliency to prevent costly beam time losses is provided in numerous ways. In case of temporary network issues, the DAQ computer reissues the command to pick up a sample, return it, rotate it or change its beam height position. If the command cannot

be executed due to mechanical issues, a report is stored and a new command is requested from the DAQ computer. This procedure repeats itself for all commands pertaining to the irretrievable sample (e.g. various rotations and beam positions). Then the command for the next sample in line is executed and an email summarizing all skipped samples is sent. When transporting samples to or from the beam position, a certain mechanical reference point has to be reached. If this cannot be achieved, the stepper motion is assumed to have stalled and its position to be out of sync. In that case, LabVIEW maneuvers the gripper back into its home position with the current sample loaded, the reference point is re-established, and the sequence of positioning the sample is resumed.

4.1.4. **Discussion and Results**

The incorporated optical limit switches provide reliable motion control, as reference positions do not shift due to mechanical fatigue. Samples are more successfully retrieved also due to the optical feedback system. No vanadium cans have been damaged since the optical feedback system became functional. In case a sample can still not be retrieved, the LabVIEW program requests information about the next sample, avoiding the need for immediate maintenance and attention regarding the skipped sample which can be granted at a more convenient time. An image is taken before the sample is transported into the beam position to archive sample mounting and orientation. Defective hardware can be swapped any time, even by personnel unfamiliar with the system, as the custom firmware is uploaded to the

motion controllers automatically. The increased user friendliness reduces downtime as the user is instantly advised with a list of potential problems to inspect.

Misalignment of the sample position due to custom-built sample holders or glued on samples and the resulting inaccuracy of the lattice parameters is tolerable for texture measurements. For powder samples, the overall mechanical accuracy of the sample alignment is sufficient as accurate absolute lattice parameters from a neutron time-of-flight experiment can only be accomplished with an internal standard: Even slight misalignments, i.e. deviations from the calibration sample position, of less than a millimeter result in measurable diffraction peak-shifts (section 3.4). The only way to circumvent this and obtain reliable absolute lattice parameters from a neutron time-of-flight experiment is by adding an internal standard, i.e. mixing a substance of known lattice parameter with the sample and re-calibrating the sample position based on this lattice parameter. In practice, if the absolute lattice parameters are needed, the sample is measured at the same temperature by X-ray diffraction.

To reduce background from air scattering in the sample tank, the beam entrance and exit ports of the HIPPO sample chamber are connected with a 73 mm diameter aluminum shroud pipe, lined with 3.2 mm borated silicon [67] on the inside to absorb air scattered thermal neutrons. The shroud pipe has an oval opening of 110 mm along the beam and 51 mm perpendicular to the beam direction for the sample. The shroud pipe improves the ratio of peak intensity to background by 1.5 to 2.0, depending on the incident wavelength and the detector position, as compared to operation without it. For comparison, in vacuum (without the sample changer), the peak intensity to

background ratio is 2.3 to 3.0 times better than for the unshielded direct beam in air. Due to the design of the sample changer, operation in vacuum cannot easily be achieved, but since the recent installation of a 'T_0 chopper' high energy neutrons entering the sample chamber were greatly minimized. Without the chopper, high energy neutrons generated at the instance of the spallation, i.e. at time T_0, were moderated close to or even inside of the HIPPO sample chamber by the surrounding shielding and thus, visible to the detectors. In some cases, this increased the background after the installation of shielding without operating the T_0 chopper. Further background reduction of thermal neutrons using shielding in the sample chamber is ongoing.

4.1.5. **Summary**

This automated sample changer significantly reduces the time required to change samples and allows unattended operation of the instrument. Its three degrees of freedom allow for versatile use for texture analysis and sample alignment. Over 500 texture and almost 100 powder samples have been measured since its upgrade in 2010. Advancements in the software, mechanical components, electrical and optical feedbacks resulted in a high resiliency, improving the productivity and reliability of continuous sample measurements.

Typically, the time gap between texture measurements is ~10 seconds for different orientations of the same sample, and ~2 minutes between consecutive samples.

4.2 Creep Furnace

A resistive furnace combined with a load frame [79] was built that allows for *in situ* neutron diffraction studies of high-temperature deformation, in particular, creep. A maximum force of 2700 N can be applied at temperatures up to 1000ºC. A load control mode permits studies of e.g. creep or phase transformations under applied uni-axial stress. In position control, a range of high-temperature deformation experiments can be achieved. The examined specimen can be rotated up to 80º around the vertical compression axis allowing texture measurements in the neutron time-of-flight diffractometer HIPPO (Section 3.1).

4.2.1. **Motivation**

The ability to study texture, lattice strains, and phase transformation kinetics of a material under uni-axial stress and at elevated temperature *in situ* provides unique insight into, for example, variant selection during phase transformations or deformation mechanisms active during creep. Variant selection describes the preferred occurrence of otherwise equivalent crystallographic orientations in a crystal undergoing a phase transformation due to an external stimulus e.g. local stresses. There is evidence that for example in hexagonal closed packed (hcp) metals anisotropic thermal expansion induced stresses contribute a driving force for variant selection during such a phase transformation [4]. It has also been observed that an applied macroscopic stress during phase transformation can provide a biasing force for variant selection [80]. Since the resulting orientation distribution of all crystals

after a phase transformation will determine the mechanical properties of the polycrystalline aggregate, understanding and ultimately predicting the involved processes is crucial for material scientists and engineers to optimize material properties. Similarly, understanding of active deformation mechanisms during creep is of paramount importance for modeling material behavior under stress at elevated temperatures. Likewise, in materials with low crystal symmetry such as hcp (e.g. Zr, Mg, Ti, Be etc.) the propensity of twinning versus slip changes as a function of temperature and strain rate, which can be studied *in situ* with the device presented here. *In situ* neutron diffraction allows measurement of e.g. lattice strain evolution as a function of crystal orientation relative to the applied stress as well as texture. Both quantities provide unique input as well as benchmark and constraining parameters for material models such as visco-plastic self-consistent models. Therefore, an apparatus was designed, constructed and published by Reiche et al. [79] that allows for the acquisition of neutron diffraction data while the specimen is under uni-axial stress at elevated temperatures, the so-called creep furnace. Additional rotation of the sample, while at stress in the furnace, allows texture measurements in the HIPPO instrument at LANSCE.

4.2.2. **Mechanical Design**

Design of this creep furnace was driven by the need to maximize temperature and applied stress while being constrained by the ability to perform *in situ* neutron diffraction experiments. The latter directs the selection of materials as well as

geometrical constraints (Figure 4.3). Electrical and software development as well as assembly were done in-house at LANSCE. I enjoyed a collaboration regarding the mechanical design with the Queen's University, Kingston, Canada.

A. Vacuum Chamber

For the purpose of reducing oxidation of sample and resistive metal heating elements, there are two viable options; either inert cover gases or vacuum to surround the sample. I selected the vacuum environment due to the additional benefit of

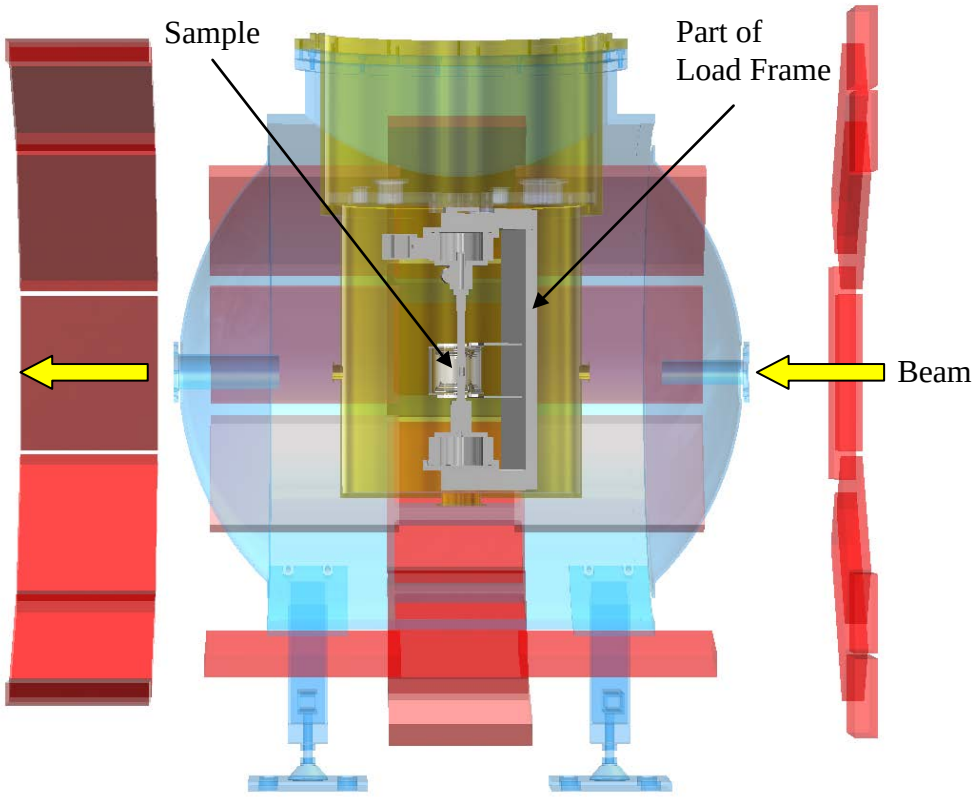

Figure 4.3: Section view of HIPPO from side, illustrating intersection of neutron beam with sample. Figure originally published in my paper [79].

reduced convective heat loss. This results in lower necessary input power, fewer cooling requirements for adjacent parts and fewer pressure safety concerns. In order to accommodate the combined load frame and furnace instrumentation, we built the largest possible vacuum chamber the HIPPO instrument allowed for. The limiting factor for the radial size was the 73.7 cm (29 in.) diameter opening of the LANSCE standard flange on the top side of HIPPO's sample chamber (Figure 3.2). By standardizing both the flange of the sample environment wells and the beam position relative to that flange, this apparatus, like many other sample environments at LANSCE, fits into four different instruments of LANSCE; aside from HIPPO, it is compatible with NPDF (*Neutron Powder Diffractometer*), SMARTS (*Spectrometer for Materials Research at Temperature and Stress*), and the inelastic neutron scattering instrument *Pharos*. A top hat (Figure 4.4) provides a cylindrical vacuum chamber with a total evacuated volume of ~200 liters. To minimize weight and intensity losses of diffracted neutrons, the vacuum chamber is made of aluminum alloy 6061. To minimize diffraction from the beam ports, the neutron beam enters and exits via vanadium beam windows mounted on cylindrical beam ports. The base plate (marked blue in Figure 4.4), with the load-frame and furnace assembly suspended below and connectors and electrical equipment on top, can be lifted out of the vacuum chamber into a stand for sample changes and maintenance. The total assembly weighs 225 kg. The same top hat can also be used for a high-temperature graphite furnace (section 4.3) by simply swapping the base plates.

A primary rotary vane pump in combination with a Varian V301 turbo-molecular pump achieves vacuum pressures of the order of 10^{-6} mbar, measured with a cold cathode gauge.

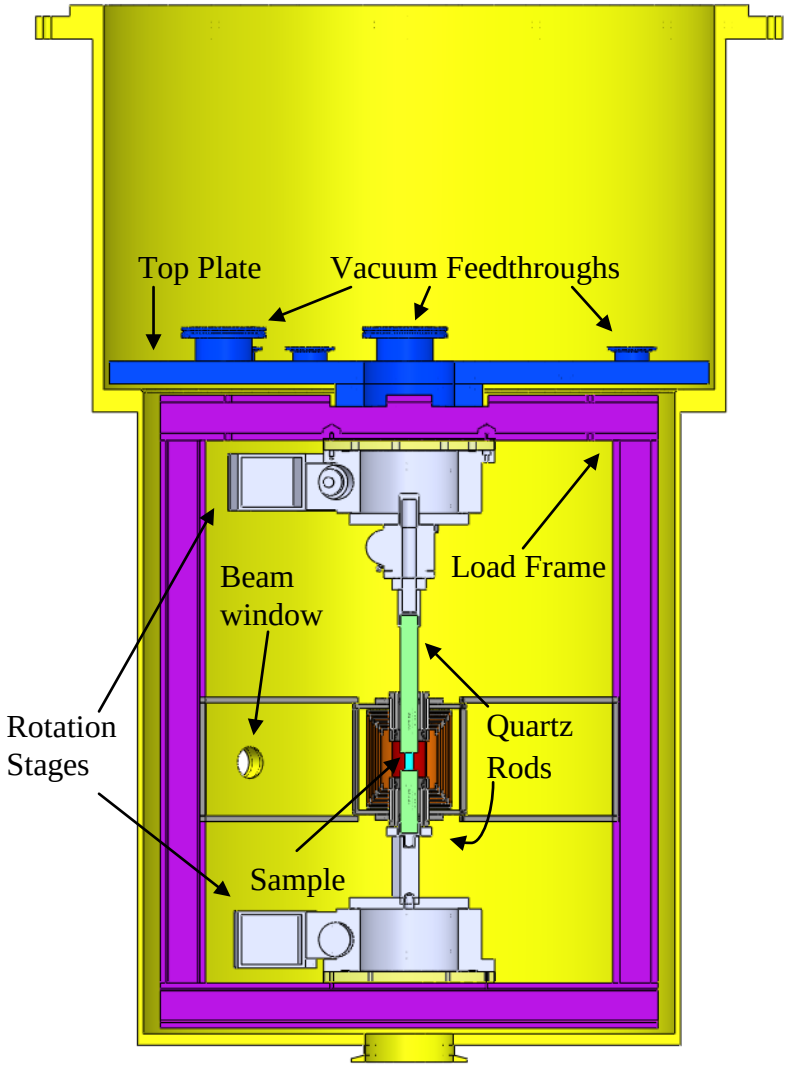

Figure 4.4: Section view of sample environment top hat showing vacuum sealing top plate (dark blue), load frame (purple), rotation stages (grey), quartz push rods (green), vanadium heat shields (orange), heating element (red), and sample (light blue). Overall height is 1.3 m. Figure originally published in my paper [79].

B. Furnace

As the vacuum reduces the convection in this system, the remaining heat loss can be described by conduction and radiation. The former can be described by

$$\dot{Q}_{Cond} = k \cdot A \frac{\Delta T}{x} \tag{3.1}$$

where $\dot{Q}$ denotes the heat flow, k the thermal conductivity, ΔT the temperature difference measured between two points at distance x and connected by a material with cross section A. The radiation heat loss is described by

$$\dot{Q}_{Rad} = \varepsilon \cdot \sigma \cdot A \cdot (T^4 - T_{Sur}^4) \tag{3.2}$$

where surface A has an emissivity ε at temperature T (in Kelvin), is surrounded by temperature T_{Sur} and σ is the Stefan-Boltzmann constant. At higher temperatures the T^4 term of the radiation heat flow dominates the total heat flow. Thus, the heating element is surrounded by up to six layers of heat shields (Figure 4.5) which are equally spaced by 3.5 mm. All shields and elements are made of 99.8% pure vanadium sheets of 40 μm thickness with a melting point of 1910˚C. Vanadium has a very low (0.0184 b) coherent scattering cross section, resulting in negligible neutron diffraction peaks and thus can be tolerated to be in the neutron beam with the sample. The assembly of heating element and heat shields is designed as a clam-shell setup, allowing access to the sample in the center by vertically parting the shields and heating element in two shells. The assembly has a total height of 90 mm at the fourth layer of heat shields, providing a hot zone height of approximately 40 mm to

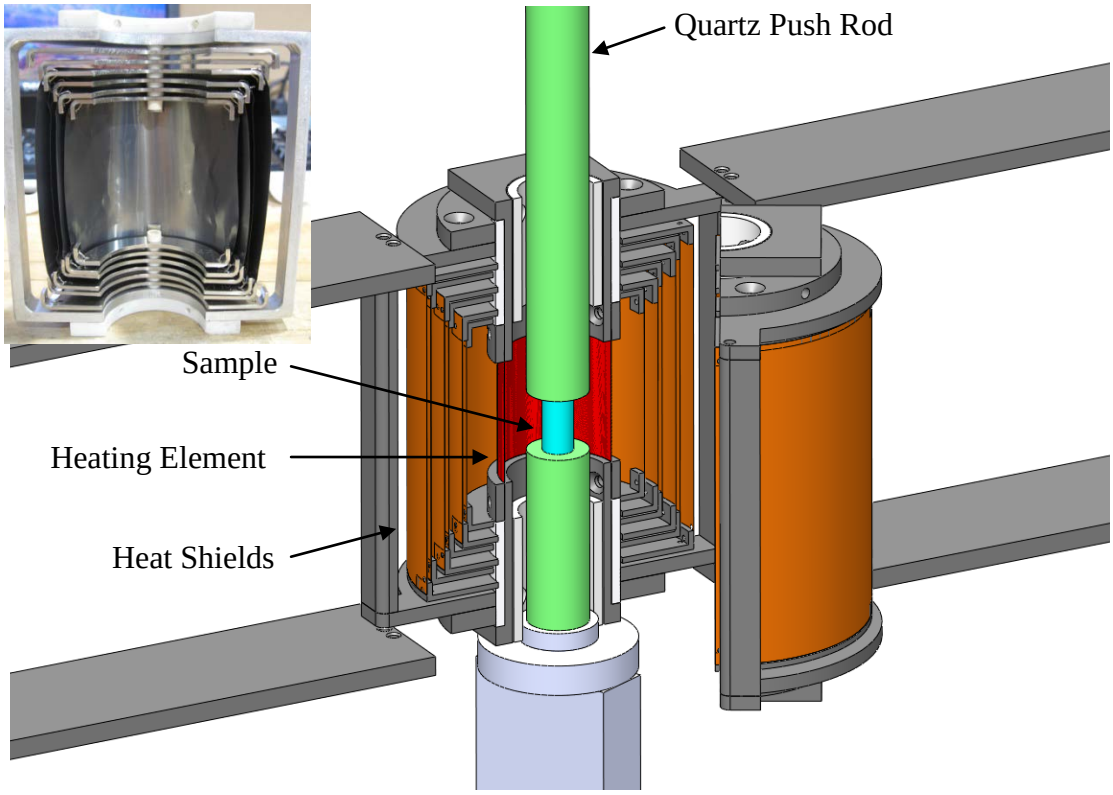

Figure 4.5: Schematic of furnace core with Al_2O_3 electrical isolators shown in white. Top left: Photograph of half of one shield assembly. Figure originally published in my paper [79].

accommodate cylindrical samples of up to ~20 mm height and ~10 mm diameter, which completely fill the 10 mm diameter neutron beam spot.

The 38 mm diameter heating elements are press fitted between screw-connected stainless steel half cylinders, allowing for quick exchange of the heating elements after many heating cycles when the vanadium fractures due to grain growth. These stainless steel brackets are electrically isolated from their surroundings by machined Al_2O_3 spacers (Figure 4.5).

C. Load Frame

The sample is held in the center of the hot zone by 20 mm diameter silica glass push rods. Silica glass allows for high compressive strength at elevated temperatures and low thermal conductivity, minimizing a thermal gradient in the sample. The rods are compressed using a motorized *Joyce* machine screw jack (Model WJ1000) and the applied force is measured by an 'S'-shaped *Omega* load cell (Model LCCA-750). Sample, rods, jack and load cell are rotated for texture measurements with two synchronized *Newport* rotation stages (Model RV160PE-EV6) mounted to a hollow stainless steel frame with a profile of 50.8 x 76.2 mm [2 x 3 in.] and 4.6 mm [0.18 in.] wall thickness. These rotation stages are the limiting factor of the maximum compression force of 2700 N of the load frame. The stainless steel frame was chosen to block the 120˚ detectors on one side and the 60˚ detectors on the other to avoid a partial shadowing of multiple detector rings (Figure 4.6). The pathway from the sample to the 90˚ detectors was left unobstructed because these deliver a valuable diffraction signal. The reason for this is based upon their proximity to the sample which results in a larger solid angle covered as compared to the 60˚ and 120˚ detectors, a thinned window in the HIPPO vacuum chamber at the 90˚ position, resulting in decreased attenuation of diffracted neutrons, and a diffraction angle providing a balanced resolution to intensity ratio.

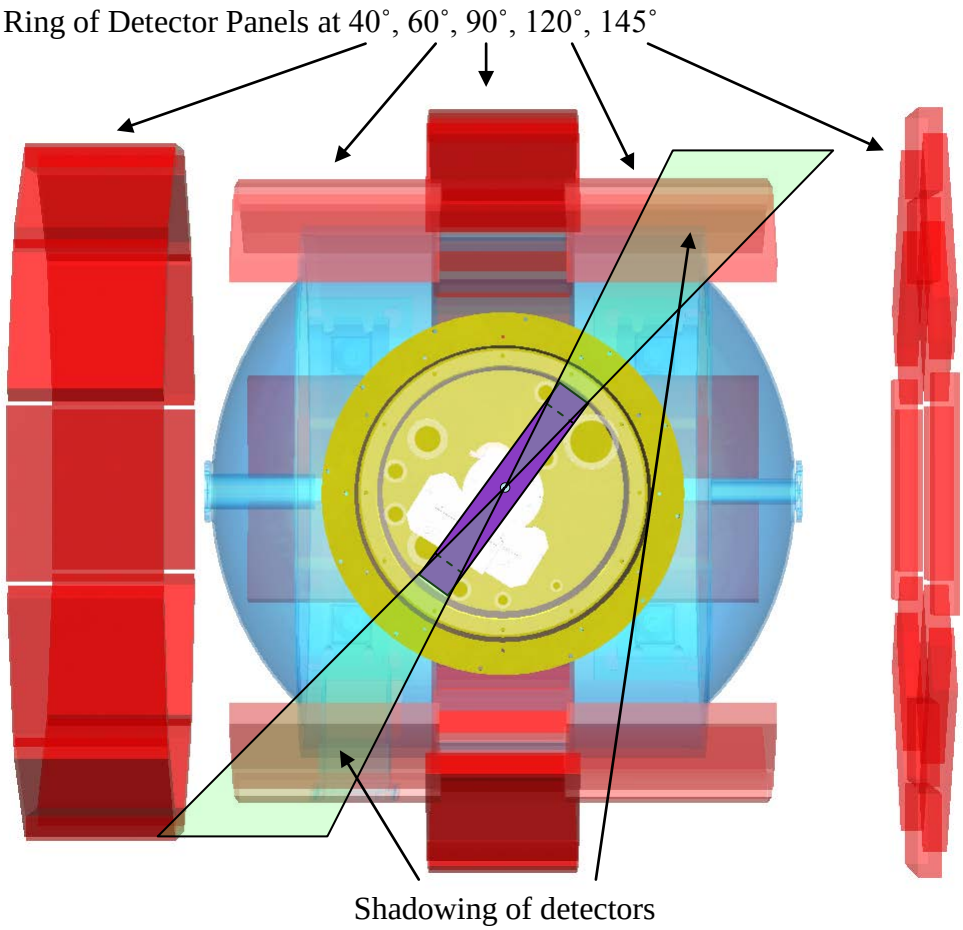

Figure 4.6: Top view of HIPPO illustrating shadowing of detector banks at 120˚ on top and 60˚ on bottom from load frame. Figure originally published in my paper [79].

D. Strain

A finite element analysis, confirmed by ex-situ compression experiments, revealed a maximum deformation of the complete load train by 0.1 mm with the maximum force of 2700 N applied. This load-dependent deformation is subtracted from the total displacement during an experiment, which is derived by the count of micro steps of the compression stepper motor.

4.2.3. **Electrical and Software Design**

Redundant hardware and software interlocks ensure safe operating conditions. The power to the heating elements is interrupted if the vacuum is breached, one of four monitored temperatures (sample position, outer heat shield, beam port, electrical connector) exceeds a predefined limit, the flow rate of cooling water is insufficient, or communication with the controlling LabVIEW program is unsuccessful for more than 45 seconds.

I developed robust control software at LANSCE using LabVIEW to provide an interface for the load frame, furnace equipment and motion control units, as well as communication with the main data acquisition (DAQ) computer using EPICS. The EPICS interface allows experiment automation such that diffraction data can be accumulated up to a specified integrated beam current before a sample is rotated, deformed or heated to the next measurement point. In the initialization routine, all customized motion control parameters such as scale factors and velocities are transmitted to the motion controller, allowing for quick Plug and Play exchange of sporadically defective hardware. An ample error detection routine identifies common errors (e.g. communication problems) and suggests a series of solutions to users, in cases where an automatic solution could not be implemented. Both temperature and stress are controlled by LabVIEW with an advanced PID controller and fuzzy logic controller respectively. The PID controller features a rate limiter and an optional ramp rate. The values for the proportional (P), integral (I) and differential (D) coefficients have been calculated, experimentally refined, and are changed during

operation based on a temperature dependent table; because the heat loss in the furnace and thus its thermal system response is, according to Equation 3.2, highly temperature dependent. The stress is controlled by a simple fuzzy controller which allows for a straightforward regulation of this non-linear system. In particular, this solution offers a simple way to manage both sample loading when no wind-up of the integral coefficient is allowed, as well as during material softening at higher temperatures when the stress has to be balanced between excessive sample deformation and misalignment of the sample, especially during sample rotations.

Similar to the operation of the sample changer, also this LabVIEW program interfaces with the Perl script on HIPPO's main DAQ computer and processes a simple spreadsheet with details of the current sample and the desired temperature and deformation profile. During normal operation, the user is assumed to be away from the local screen and the LabVIEW program will send a message to a pager and/or cell phone to communicate occurring issues, from which a recovery without human intervention is impossible. The status of the furnace is also tied into the instrument status web page for routine monitoring.

4.2.4. **Conclusion and Outlook**

This novel apparatus provides new opportunities to study the individual influences of elevated temperatures and uni-axial stress on the evolution of texture and strain. I successfully confirmed phase composition and texture via comparison with room temperature results from a known sample environment, as well as

temperature dependent lattice parameters which agree with published results of conventional furnaces and literature values. Commissioning results are described in Chapter 5.0.

To allow tensile creep tests, the silica glass rods could be replaced with custom made rods exhibiting threads or pin holes to pull on dog-bone shaped samples with a small diameter gage section slightly longer than the beam diameter and substantially larger diameter shoulders. A further enhancement in opening up an ample new range of experiments would be the installation of a high-temperature extensometer which could penetrate the heating elements with a set of ceramic extensions.

4.3 High-Temperature Furnace

A resistive high-temperature furnace capable of temperature up to at least 2200˚C at heating rates of 100˚C/min was built that allows for *in situ* neutron diffraction studies. A up to 28 mm in diameter and 100 mm long sample can be translated in the vertical direction by 50 mm and rotated around the vertical axis by 360˚ enabling texture measurements and various sample volume scanning at elevated temperatures.

4.3.1. **Motivation**

In situ neutron diffraction investigations of materials above 2000˚C provides unique insights into e.g. phase diagrams, thermal expansion, kinetic studies of solidification and solid state transformations of refractory compounds. This

temperature range above 2000˚C is experimentally challenging [81] and thus not routinely available at neutron beam lines.

This is evident, as the *Inorganic Crystal Structure Database* (ICSD) collected by *Fachinformationszentrum* (FIZ) Karlsruhe [82] lists, for example, 15 entries of UC_2 structures. Whereas 12 describe the quenchable tetragonal UC_2 ε-phase, only three deal with the non-quenchable cubic UC_2 δ-phase stable between 1769˚C and 2560˚C. One of the three entries is a calculated first-principle study and the other two experimental data, which contradict each other. Thus, a furnace for routine high-temperature neutron diffraction experiments to study e.g. phase structures is desirable.

The following alternate models of high temperature furnaces for *in situ* neutron studies have been designed but exhibit limitations which lead to the development of the furnace presented here. An induction furnace has been published by Bowman et al. [83] reaching 2500˚C, but the available diffraction opening 2θ is limited to 70˚, which would shield most of the HIPPO detectors. It also does not feature a rotation axis for texture measurements. Induction furnaces have advantages of being mechanically relatively trouble-free to implement and to exhibit high heating rates. The challenges are that poorly conducting ceramics such as oxides can only be heated in a conducting sample holder [83]. The sample holder and radiation shielding are in the diffraction beam, producing considerable interference in the diffraction pattern [83]. Mirror furnaces, which commonly have an oval mirror with a light source in one focal point and the sample in the other, can be equipped with rotation stages allowing

for texture measurements, but are often limited to 2000˚C [84] due to cooling difficulties of the reflective surfaces. A resistive neutron-scattering furnace for temperatures up to 2657˚C has been explained by Clausen et al. [85] , known as the Harwell furnace. The heating elements and inner heat shields are made of tungsten, whereas, the outer heat shields are made of molybdenum providing a good balance between their lifetime and neutron attenuation. A common point of failure for tungsten at high temperatures is material embrittlement based on grain growth or chemical transformations due to imperfect vacuum. The sample temperature is measured via a type C thermocouple and an infrared pyrometer. Nevertheless, the sample cannot be manipulated in the beam position, which does not allow for texture measurements.

It is clear from the literature that different types of heating are not equally well suited to different types of (single-crystal, powder) diffraction experiments [84]. A particular type of furnace and specific method of temperature determination and control must be chosen for a specific scientific problem [84].

Here, I present the development status for an ultra-high temperature furnace for the HIPPO diffractometer at LANSCE. This device provides to-date temperatures up to 2200˚C in combination with vertical sample scanning and vertical rotation for texture measurements. Mechanical, electrical and software design as well as assembly were done in-house at LANSCE.

4.3.2. **Mechanical Design**

The mechanical design is a derivative of a graphite tube furnace for neutron radiography at atmospheric conditions by Kahle et al. [86] to investigate viscosity properties. I supported the substantial mechanical adaptation for neutron diffraction which was spearheaded by Dr. James Wall. Design of this high-temperature furnace was driven by the need to maximize temperature yet allow for sample position manipulation and vertical rotation, while being constrained by the ability to perform *in situ* neutron diffraction experiments. The latter drives choices for materials as well as geometrical constraints.

For the purpose of reducing oxidation of sample and the resistive graphite tube a vacuum environment as well as reduced heat loss due to thermal convection the high-temperature furnace operates in vacuum. This furnace shares the aluminum vacuum chamber with the creep furnace described in section 4.2. To swap between the two furnaces, the base plate of one can simply be craned out and replaced with its counterpart of the other furnace (Figure 4.7, left).

The base plate of the high-temperature furnace holds feedthroughs for water, power and thermometry as well as the translation stage (Figure 4.7, right). Suspended below this plate is the 590 mm long hollow graphite tube representing the heating element. Water-cooled copper clamps on both ends of the tube conduct the electric power from the tube through copper wiring along a circular path to avoid the diffracted neutron path to the feedthroughs.

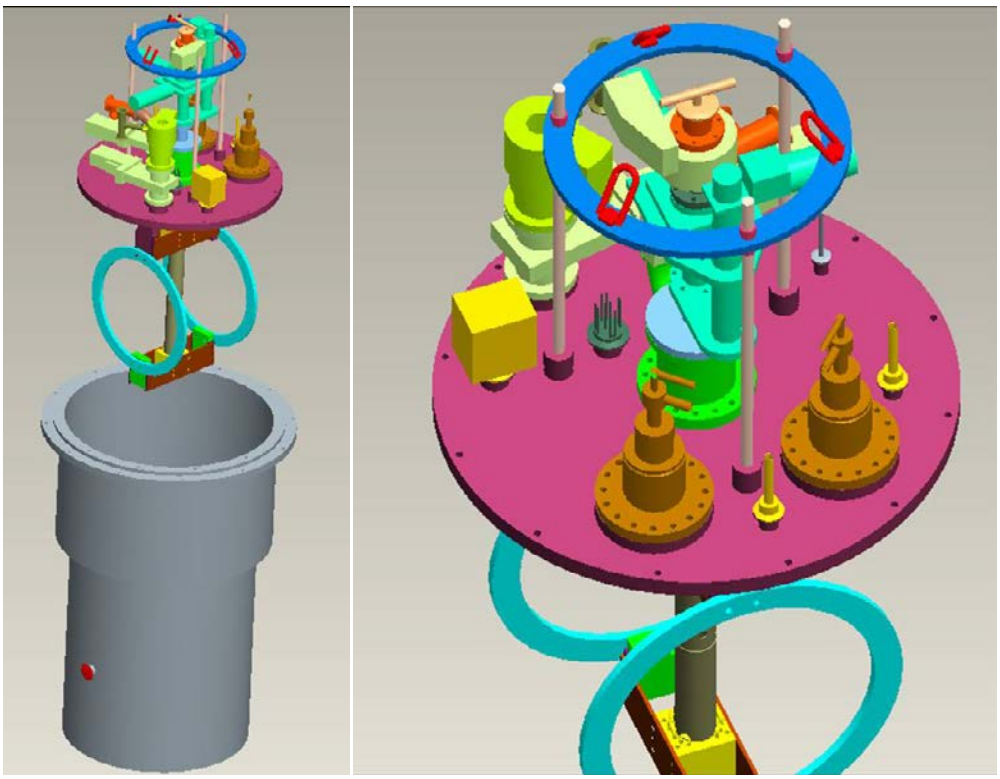

Figure 4.7: Left: High-temperature furnace suspended on base plate (pink) craned out of its vacuum chamber (gray). Right: Top plate (pink) of furnace showing vacuum feedthroughs for water (yellow), power (orange) and thermometry (dark gray). A translation stage (center) manipulates a sample stick reaching inside the graphite tube (brown) below the top plate.

The inside diameter of the heating tube is 38.1 mm (Figure 4.8) where the 864 mm long sample stick is inserted. To minimize radial sample misalignment a coupling piece with an inside opening of 28 mm mates with its counterpart connected to the sample stick with little tolerance (Figure 4.9). Thus the maximal sample diameter is limited to < 28 mm. This copper alignment piece is water cooled and joins the tungsten rod from the sample stick head with a 343 mm long graphite rod with the sample attached to its tip.

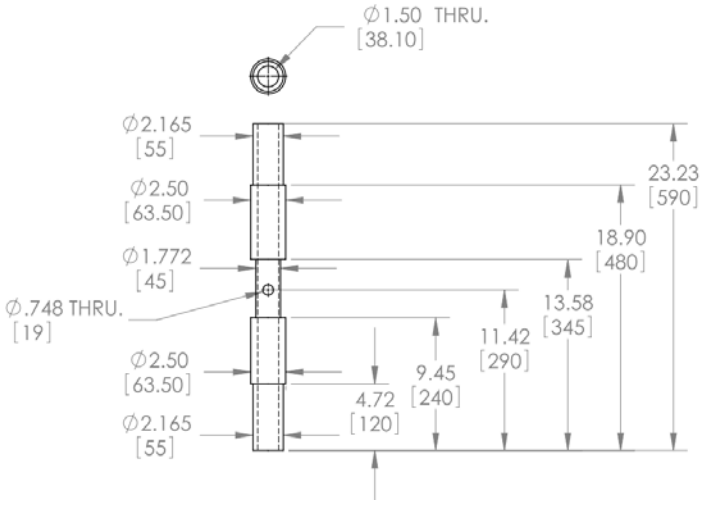

Figure 4.8: Hollow graphite furnace heating element with dimensions in inches and mm in brackets

On the outside of the heating tube a heat shield setup minimizes radiation heat losses. Two water-cooled half shells made of aluminum each contain two pieces of graphite acting as a thermal buffer. The layered structure of graphite exhibits highly anisotropic thermal conductivity as phonons propagate rapidly along the tightly-bound hexagonal lattice planes, but slower from one plane to another. Therefore,

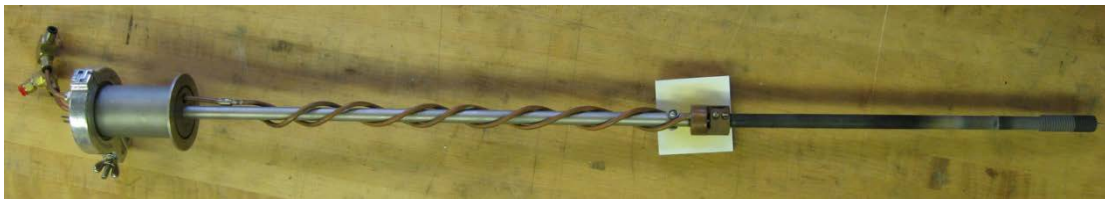

Figure 4.9: Tungsten sample stick with water quick connectors (far left), vacuum flange (left) and water-cooled copper coupling piece (center). This coupling piece provides radial alignment and a junction for the graphite sample stick (right). The thermocouple is connected at the same location as the water and guided in the center of the hollow stick to the tip where its sheath is exposed (far right).

layers of the inner buffer are oriented coaxially to the heating element reducing radial heat loss surrounded by another piece with perpendicular layer orientation minimizing coaxial heat loss at the edges of the hot zone (Figure 4.10).

Except for the vanadium vacuum ports, only the sample is exposed to the incident neutron beam. Materials in the direct beam exhibit a low coherent cross section to avoid an overlap of Bragg diffraction peaks from the material with those of

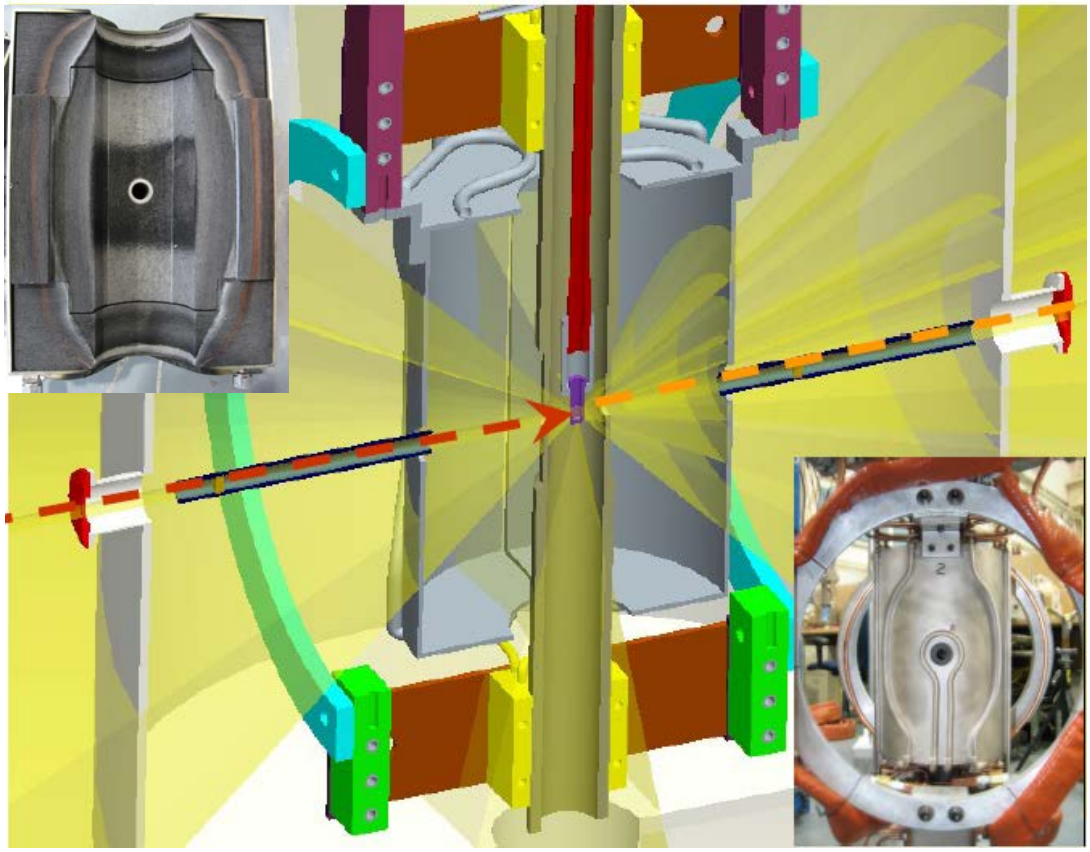

Figure 4.10: Photograph (right inset) and CAD model cutaway of hot-zone showing sample (center, purple), suspended by sample stick (red) inside graphite tube (brown), surrounded by water-cooled aluminum shells (grey). Left inset shows photograph of one half of this shell containing a two piece thermal graphite buffer. Incident neutrons (red dashed arrow) are either diffracted to the detector banks (yellow cones) or transmitted (orange dashed arrow).

the sample. Materials between sample and detector are required to have low absorption (σ_{abs}) and combined scattering (σ_{Scatt}) cross sections to avoid attenuating the diffracted neutrons. Here, the diffracted neutrons have to penetrate graphite (σ_{Scatt}=5.55 b and σ_{abs} =0.004 b) and aluminum (σ_{Scatt}=1.50 b and σ_{abs} =0.23 b).

A primary rotary vane pump in combination with a Varian V301 turbo-molecular pump achieves vacuum pressures of the order of 10^{-6} mbar, measured with a cold cathode gauge CCG-525 from *Terranova*.

4.3.3. **Electrical and Software Design**

I plotted the entire control and power electronics in the schematic shown in Figure 4.11. This related view indicates the spatial grouping of the individual components into the transformer box, which is located outside of the diffractometer near the 480 V / 60 A receptacle, the top hat box attached to the sample environment and the components inside the vacuum chamber. The latter are connected via vacuum feedthroughs. A 480 V to 400 V autotransformer T1 (Figure 4.11) energizes a over-temperature protected 400 V / 55 A *Bebermann* transformer T2 supplying 10 V and 0-2000 A. The amount of current is controlled by a silicon controlled rectifier (SCR) power control unit B2P-60-60-S1-CL from *Avatar Instruments Inc.* with a phase angle firing pair of inversely connected SCR's. This power control unit is marked A1 in the schematic and receives a fail-safe 4-20 mA input signal from an *Omega* D4252 digital analog converter with a RS-485 communication interface.

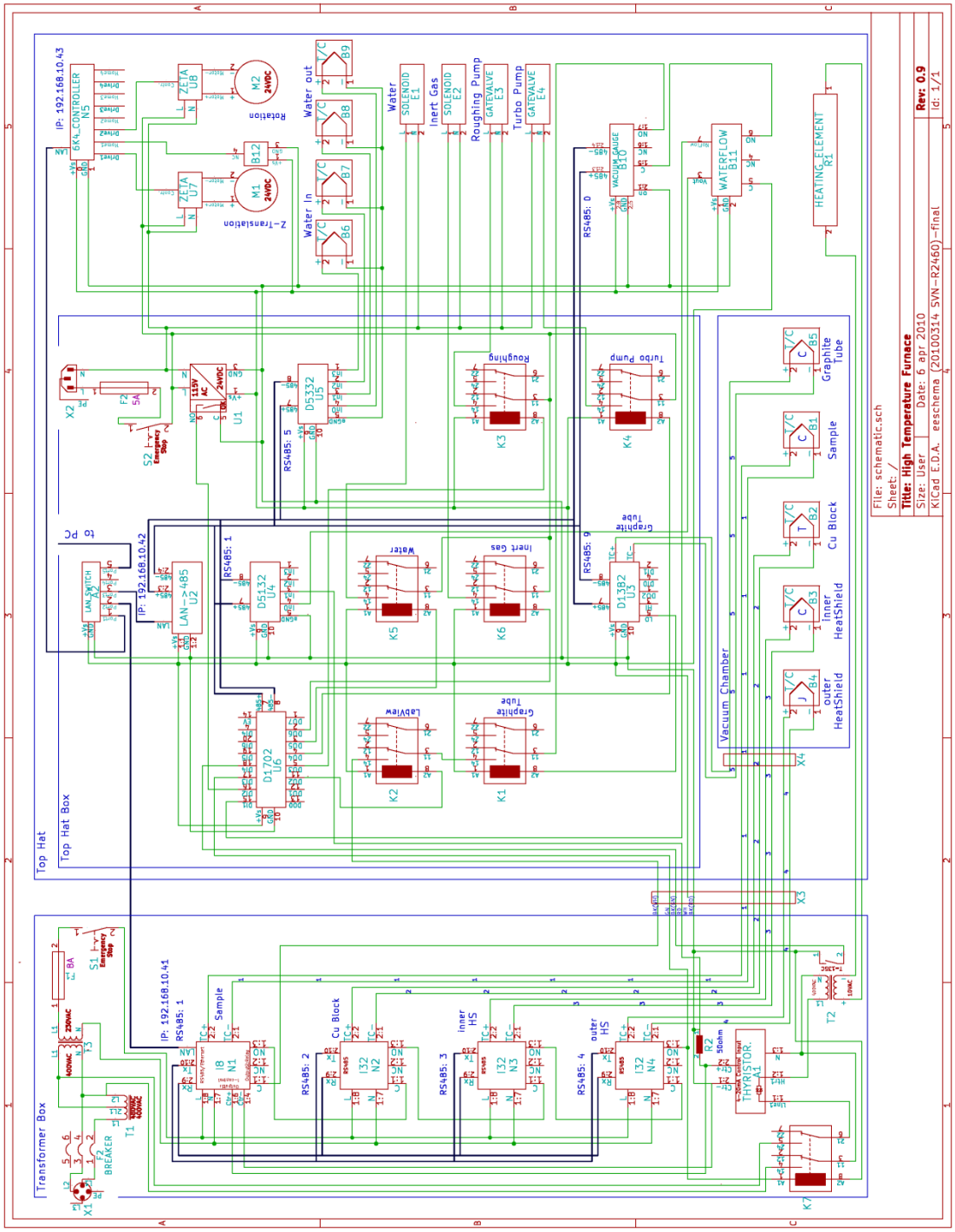

Figure 4.11: Schematic of control and power electronics employed in the furnace.

A variety of thermocouples, a water flow gauge 0808SN15 from *Proteus Industries Inc.* and a *Terranova* vacuum gauge system from *Duniway Stockroom Corp.* are also connected to D-series D/A modules from *Omega* featuring a RS-485 interface. All components on the RS-485 bus have assigned addresses and communicate to the EIS-2B RS-485-to-ethernet converter, marked U2, from *Omega* forwarding the messages via TCP/IP to the LabVIEW software, with a screenshot of the graphical user interface (GUI) shown in Figure 4.12.

Similar to the creep furnace, redundant hardware and software interlocks ensure safe operating conditions. The power to the graphite tube is interrupted by relay K7 (Figure 4.11) if the vacuum is breached, one of four monitored temperatures of thermocouples B1 through B4 exceeds a predefined limit, the flow rate of cooling

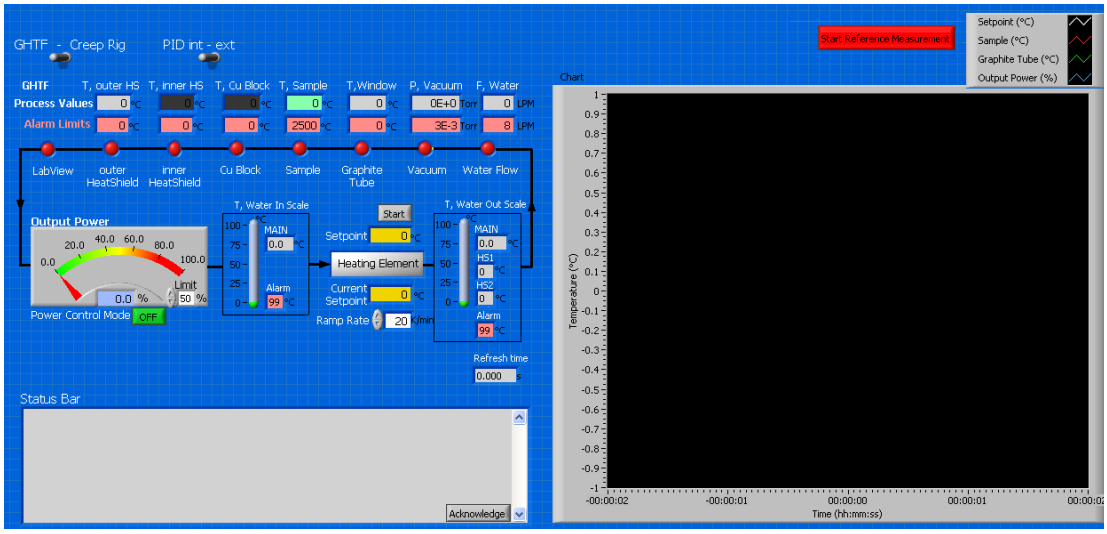

Figure 4.12: My LabVIEW graphical user interface provides a live chart of process variables, such as set point, current temperatures and output power on right. Red or green lights indicated the status of individual safety loop prerequisites for heating to occur (top left) and general feedback is detailed in a status bar (left bottom).

water is insufficient or communication with the controlling LabVIEW program is unsuccessful for more than 45 seconds.

I developed robust control software at LANSCE using LabVIEW to provide an interface for the thermometry, water and vacuum gauges and motion control units, as well as communication with the main DAQ computer using EPICS. The EPICS interface allows experiment automation in order that diffraction data can be accumulated up to a specified integrated beam current before a sample is rotated, aligned in height or heated to the next measurement point. As with the creep furnace, an ample error detection routine identifies common errors (e.g. communication problems) and suggests a series of solutions to users, in cases where an automatic solution could not be implemented. The sample temperature is controlled by LabVIEW with an advanced PID controller, which features a rate limiter and an optional ramp rate. The values for the proportional (P), integral (I) and differential (D) coefficients have been calculated, experimentally refined, and are changed during operation based on a temperature dependent table, because the heat loss in the furnace and thus its thermal system response is according to Equation 3.2 highly temperature dependen. LabVIEW further interfaces via TCP/IP with an EPICS module to manipulate the MDrive Hybrid integrated motor systems from *Schneider Electronic* to control vertical height and rotation of the sample.

Typically, the LabVIEW program is remotely controlled by a Perl script, which runs on HIPPO's main DAQ computer and processes a simple spreadsheet with details of the current sample and the desired sample positioning and temperature

profile. During normal operation, the user is assumed to be away from the local screen and the LabVIEW program will send a message to a pager and/or cell phone to communicate occurring issues from which a recovery without human intervention is impossible. The status of the furnace is also tied into the instrument status web page for routine monitoring.

4.3.4. **Conclusion and Outlook**

I successfully confirmed the temperature accuracy of the furnace by comparing thermal lattice parameter strains and carbothermic reduction of uranium dioxide with published results of conventional furnaces and literature values, detailed in Chapter 6.0. Juarez-Arellano et al. [87] published a successful experiment on the formation of rhenium carbide using this furnace.

This novel apparatus provides new opportunities to study the texture at temperatures up to at least 2200˚C, limited by the 20 kVA transformer. I recently redesigned the graphite tube to provide a larger electrical resistance ratio of hot-zone to the adjacent clamped ends of the graphite tube. Thus, more energy is deposited into the hot-zone, which should lead to slightly higher temperatures, not yet quantified. The temperature limit of 2320˚C of the employed thermocouple type C could therefore be reached soon. A method to measure temperatures outside the measurement range of a thermocouple could be done by adding a supplemental pyrometer. Alternatively neutron resonance spectroscopy (NRS) based on Doppler broadening can be incorporated in order to measure the sample temperature within a

1% accuracy [88]. As Yuan et al. [89] have shown, NRS can provide sample temperature information from a neutron pulse with a duration as short as 1 μs. This technique also guarantees that the temperature is derived from the same volume the diffraction data is acquired, as compared to surface temperatures using pyrometry or originating from an adjacent measurement point with time lagged response in case of thermocouples.

Due to an observed divergence in the neutron beam from the incident collimator to an image plate behind the sample position, I propose to integrate a heat tolerant boron carbide collimator into the heat shield. Such a nearby collimator would allow for a larger beam spot at the sample position, preventing accidental diffraction of adjacent furnace parts and thus provide better statistic and time resolution. Future enhancements could further include calorimetry, allowing a unique combination of *in situ* diffraction and calorimetric measurements. Only minor modifications are necessary to incorporate gas quenching enabling the study of phase transitions in e.g. uranium-niobium alloys or steel.

As a final improvement, we are investigating the application of other heat sources. A graphite heating element imparts the disadvantage of carbon vapor potentially reacting with the sample, which can be minimized by preceding heat cycling. Advantages are a longer lifetime (ca biannual exchange) and more cost effective replacement elements (< $200 for our graphite heating element from Figure 4.8). Heating elements made of tungsten alloy sheets would allow for similarly high temperatures, but lower partial pressures of the heating element material and

potentially equivalent lifetime based on the grain-growth inhibiting contribution of the alloyed material. Alternatively we are exploring the option of inductively heating the sample, which holds challenges such as selecting sample containers for materials with low electrical conductivity and determining a suitable balance for the water-cooled RF-coil diameter. A reduction in diameter increases the energy coupled into the sample and, thus, the maximum temperature that can be achieved, but has the downside of increasing the solid angle holding attenuating water which obstructs diffracted neutrons.

5.0 *IN SITU* HIGH-TEMPERATURE DEFORMATION OF Zr-2.5Nb

In this chapter, I present results for Zr-2.5wt%Nb under sample conditions previously inaccessible for neutron diffraction techniques. I describe *in situ* high-temperature deformation measurements, in particular characterizing texture using neutron diffraction at elevated temperatures achieved by the creep furnace (section 4.2). Zr-2.5wt%Nb is a material used for pressure tubes in CANDU® (section 2.4.1) pressurized heavy water reactors (PHWR), and anticipated to be used in the fourth generation supercritical-water-cooled reactor (SCWR) [23], that act as the primary containment vessel of high temperature D_2O inside the core [4], [90].

5.1 Motivation

Zr-2.5wt%Nb plays an important role in the nuclear industry because of the combination of low neutron absorption cross-section, good mechanical properties, low hydrogen/deuterium uptake and corrosion resistance. This alloy exhibits a phase transformation from the low-temperature α-phase to the high-temperature β-phase at ~860˚C [4]. Since the β-phase transforms back to the α-phase upon cooling, direct observations at elevated temperature, in particular during deformation in the β regime, provide information uniquely accessible by utilizing the creep furnace described in section 4.2. Existing work [4], including very recent results published in 2012 [91], [92], is limited to elevated temperatures without deformation making statements about stress effects e.g. from manufacturing processes ambiguous.

Being capable of modeling and predicting the performance and life time of these pressure tubes is paramount for the application in nuclear power plants, as premature failure may come at substantial economic and/or human cost. The difficulty and cost associated with replacing activated components of reactors during their serviceable life is large; as such, pressure tubes are intended to last for up to 30 years. Therefore, pressure tubes must not only have good strength, but also exceptional creep and corrosion resistance.

As it is of interest to understand the development of texture throughout deformation and phase changes resulting from various thermo-mechanical processing steps during fabrication, performing *in situ* heating and deformation in a neutron beam to probe texture and strains is of great interest [4], [93].

5.2 Metallurgical Characteristics and Background

Group IV transition elements, Ti, Zr and Hf, exhibit an hcp (α) crystal structure (Figure 2.7) at ambient temperature and pressure, which transforms into a bcc (β) structure at high temperatures. For Zr-2.5Nb, this phase transformation occurs at a temperature of ~860˚C [4]. Oxygen impurities can stabilize the α-phase, and thereby increase the transformation temperature as far as 920˚C [94].

Even small quantities (0.7 to 18.7 at%) of Nb alloyed into the Zr matrix can stabilize the Zr β-phase at lower temperatures, as shown by the binary phase diagram in Figure 5.1. According to this phase diagram the Zr in Zr-2.5wt%Nb (equal to Zr-2.54at%Nb) is in the β regime between 1810˚C and 815˚C. The range of 815˚C to

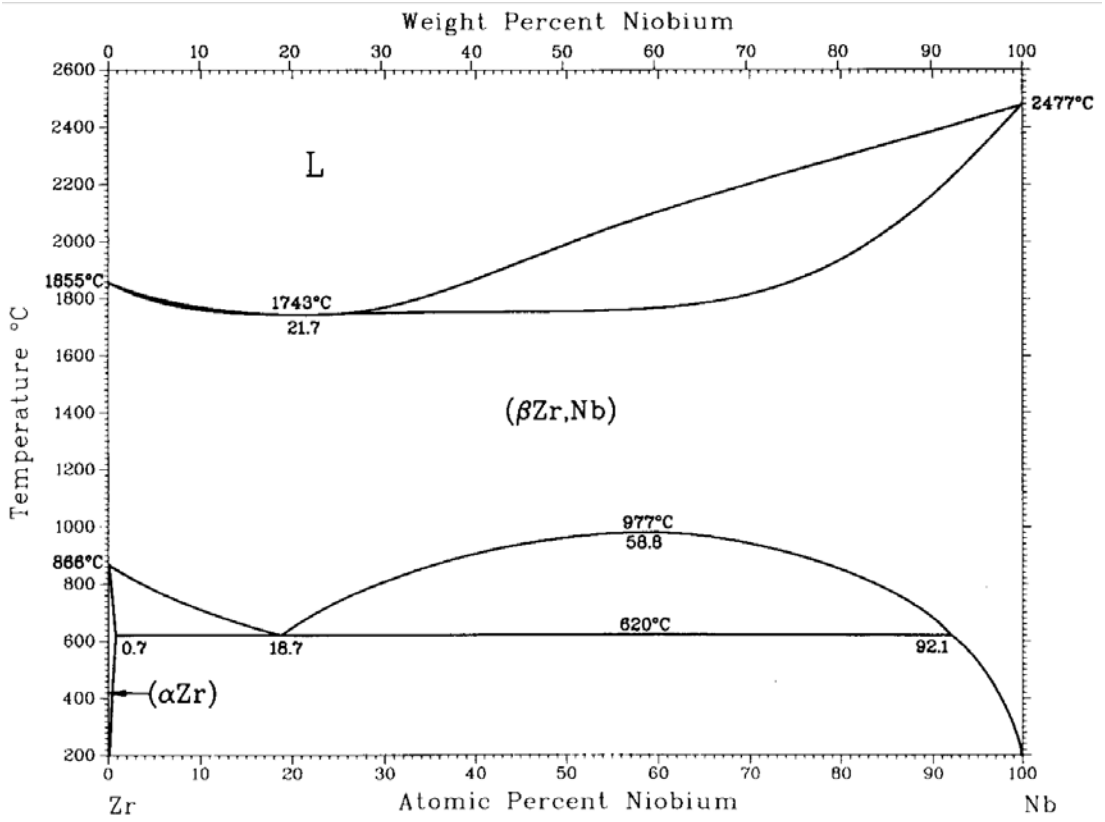

Figure 5.1: Zr-Nb phase diagram according to Okamoto [96].

620˚C denotes a two phase area of α-Zr and (β-Zr, Nb). The phase fraction of α-Zr increases with dropping temperatures in this two phase area. The (β-Zr, Nb) denotes a solid solution between Nb and the Zr β-phase, where Nb creates a slight β-Zr lattice distortion. Nb maintains in its bcc single phase up to the melting point of 2477˚C. Below the monotectic temperature of 620˚C, the α-Zr and (β-Zr, Nb) maintain nearly constant volume fractions [95].

Based on the lever rule and Figure 5.1 this fraction results in 2.42at% (β-Zr, Nb) for ambient conditions. However, even when Zr-2.5wt%Nb is not actively cooled, the

typical cooling rate is too fast to reach this equilibrium condition, with the diffusion of Nb being the rate-limiting factor. Hence, a significant portion of the β-Zr does not revert to α-Zr and typically leads to slightly less than 10wt% of metastable (β-Zr, Nb) in Zr-2.5wt%Nb at ambient conditions, with the Nb mostly concentrated in the β-Zr (< 1 wt% in α-Zr and ~20 wt% β-Zr). As the Nb content is very low with 2.5wt%, I will refer to the solid solution of (β-Zr, Nb) simply as β-Zr in the remainder of the chapter.

During the conventional manufacturing process of these pressure tubes for nuclear reactors a cylindrical ingot of raw material is forged at 1000˚C reducing its diameter from 58 cm to ~20 cm. The resulting logs are machined into hallow billets, preheated and then extruded at approximately 815˚C, with an extrusion ratio of approximately 10:1. Then the billets are cold drawn ~30% in a single step, or multiple steps being quenched in between, and finally stress relieved at 400˚C. These tubes are hollow cylinders of approximately 112 mm OD and 104 mm ID where they contain the fuel bundles and primary D_2O coolant. In order to maximize the thermodynamic output of the reactor, the coolant (from which steam is generated) is pressurized to 10 MPa (resulting in a hoop stress of 135 MPa on the inside of the pressure tube) in order to reach the operating temperature of about 250 to 310˚C in CANDU® reactors. For SCWR reactors, the anticipated operating conditions are above the critical point of water of 374˚C at 22.1 MPa, resulting in a hoop stress of 300 MPa on the inside of the pressure tube.

5.3 Experimental Setup

Experiments were conducted using the creep furnace (section 4.2) inside the HIPPO diffractometer (section 3.1) to replicate processing steps during high-temperature deformation in a 6 mm in diameter and 20 mm long sample of Zr-2.5wt%Nb-0.1wt%O-0.1wt%Fe (further referred to as Zr-2.5Nb). In order to compare data recorded in the novel creep furnace, reference measurements before and after the experiment are obtained in the sample changer (section 4.1), representing a known sample environment. A temperature of 250˚C as the start and end point of the furnace experiment was chosen as a reference to the room temperature data because no noteworthy microstructure changes are expected in the sample at this temperature [97] and multiple samples could be measured successively without using expensive neutron beam time waiting for a complete cooling of the creep furnace. To ensure the sample reached its full β regime, the highest temperature in the experiment was chosen to be 975˚C, at which I compressed the sample uni-axially by 3 mm, equivalent to 20% total compressive strain. This strain was applied at a constant temperature of 975˚C using a constant displacement rate of 0.32 mm/s (an approximate strain rate of 0.016/s at the start of the test, rising to 0.04/s by the end of the test), which is important because the results are strain rate dependent [98].

Data acquisition periods of 10 min at each of four sample orientations (0°, 45°, 62°, and 78° around the vertical axis) was sufficient to obtain texture. Data were analyzed using the E-WIMV algorithm implemented in MAUD to obtain an ODF [43]. Individual pole figures calculated from the ODF are plotted using pod2k [48].

Reported lattice parameters were calibrated based on α-Zr with the crystallographic a-axis length of 3.229 Å and c-axis length of 5.148 Å. These reference lattice parameters were determined from X-ray analysis of Zr-2.5Nb published by [99]. The necessity thereof is described in section 3.4.

5.4 Room Temperature Results from Sample Changer

Using MAUD, I calculated the Rietveld fit of room temperature data merged into 45 histograms. One histogram recorded by a 90˚ detector panel of HIPPO including peak fit is portrayed in Figure 5.2. The peak fit used either α-Zr (red) or β-Zr (green) to match all recorded diffraction peaks. The α-phase is given with four indices as its

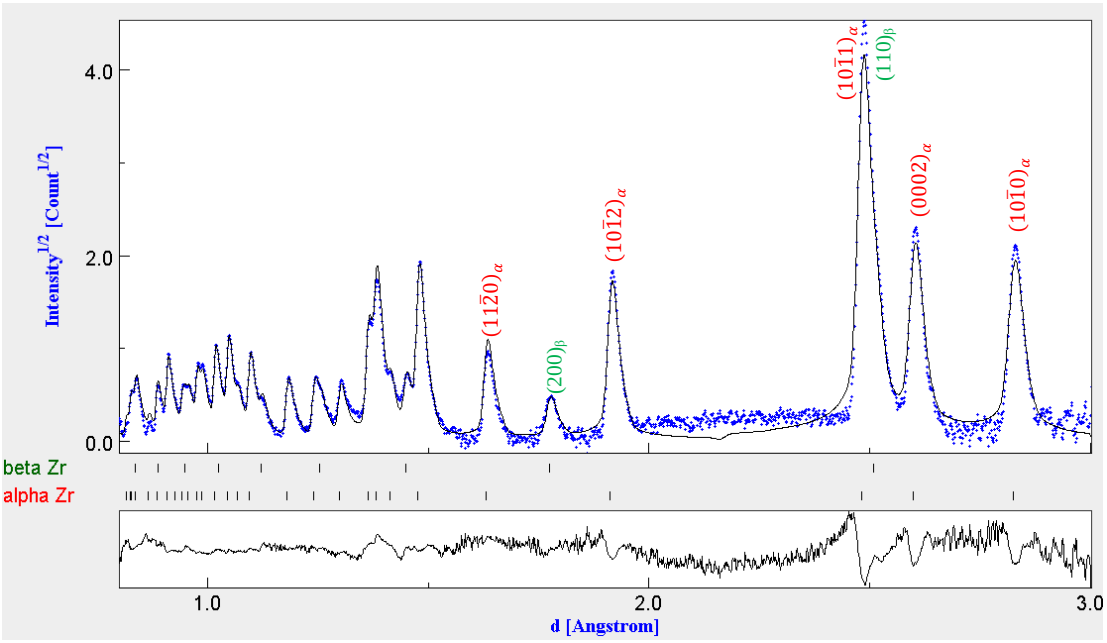

Figure 5.2: Diffraction spectrum of recorded neutron data from one 90˚ detector panel of Zr-2.5Nb in sample changer drawn with blue dots (top). The overlaid black line represents the peak fit calculated with MAUD. For d-spacings >1.5 Å the Miller indices of α-Zr (red) and β-Zr (green) are shown. The difference between data and fit is plotted on the bottom.

structure is hexagonal closed packed (hcp). A list of the calculated reflections for both phases is given in Table 5.1. The Rietveld data analysis determined a sample composition of 93±1 wt% α-Zr and 7±1 wt% β-Zr, which is identical to 93.37±1 vol% α-Zr and 7.03±1 vol% β-Zr.

Figure 5.3 shows $10\bar{1}0$ poles (i.e. poles of the prismatic crystal faces) and 0002 pole figures (i.e. hcp c-axis) of α-Zr in the left column and 110 (i.e. face diagonal) and 222 (body diagonal) pole figures of β-Zr in the right column for this sample. The top row represents the sample in as-received condition, whereas the bottom row was recorded at the end of the experiment. These data, recorded in the sample changer representing a known sample environment, serve as a reference for the following dataset recorded in the novel creep furnace. Comparing only these pole figures of

Table 5.1: List of ten largest Bragg reflections in Angstrom for α-Zr (left) and β-Zr (right) with Miller-Bravais indices. Lattice parameters that form the basis of these reflexes were calibrated with X-ray data from [99].

α Zirconium (hcp)						β Zirconium (bcc)				
No.	h	k	i	l	d-spacing	No.	h	k	l	d-spacing
1	1	0	-1	0	2.79640	1	1	1	0	2.48383
2	0	0	0	2	2.57400	2	2	0	0	1.75634
3	1	0	-1	1	2.45727	3	2	1	1	1.43404
4	1	0	-1	2	1.89384	4	2	2	0	1.24192
5	1	1	-2	0	1.61450	5	3	1	0	1.11080
6	1	0	-1	3	1.46258	6	2	2	2	1.01402
7	2	0	-2	0	1.39820	7	3	2	1	0.93880
8	1	1	-2	2	1.36772	8	4	0	0	0.87817
9	2	0	-2	1	1.34932	9	4	1	1	0.82794
10	0	0	0	4	1.28700	10	3	3	0	0.82794

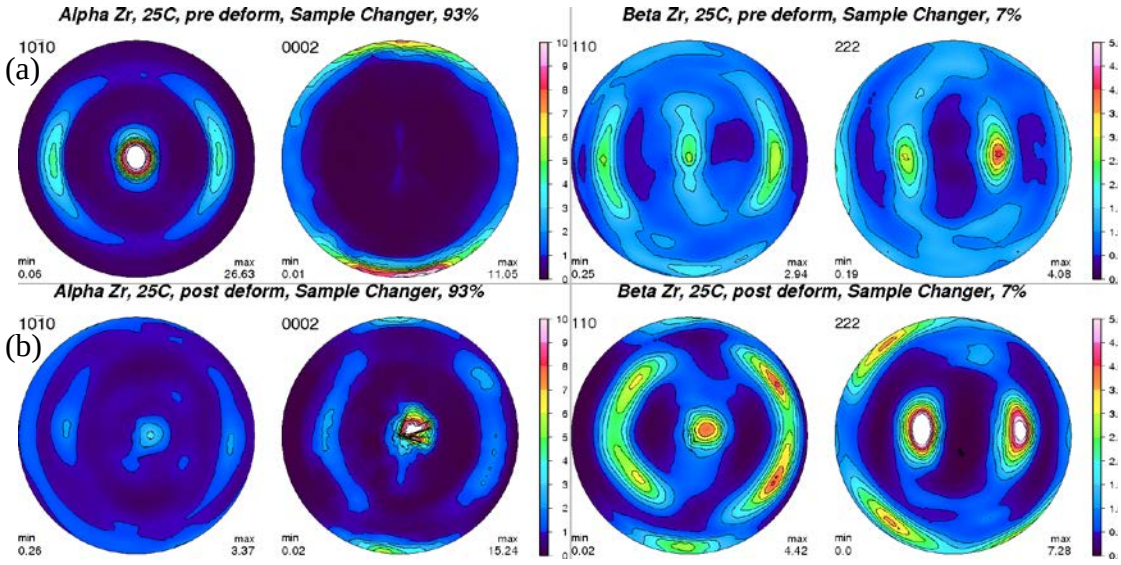

Figure 5.3: Room temperature results of α-phase (left column) and β-phase (right column) of Zr-2.5Nb measured with the sample changer (a) before and (b) after heating and 20% strain in the axial direction, which is the original extrusion direction shown about the center. The radial direction is horizontal and the hoop direction vertical.

Figure 5.3 individual factors such as heating, phase transition, compression, and cooling cannot accurately be differentiated and as such their individual influence on texture evolution remain ambiguous.

5.5 Results from Elevated Temperatures using the Creep Furnace

As a qualitative overview of the experimental results conducted in the creep furnace Figure 5.4 construes recorded neutron intensity as a function of d-spacing and experiment progression. I obtained the intensity by integrating over both, all 90˚ detectors (Figure 3.2) and all four sample orientations. A magenta colored bar in the top left corner of this figure indicates a recorded spectrum with 20% compression applied to the sample.

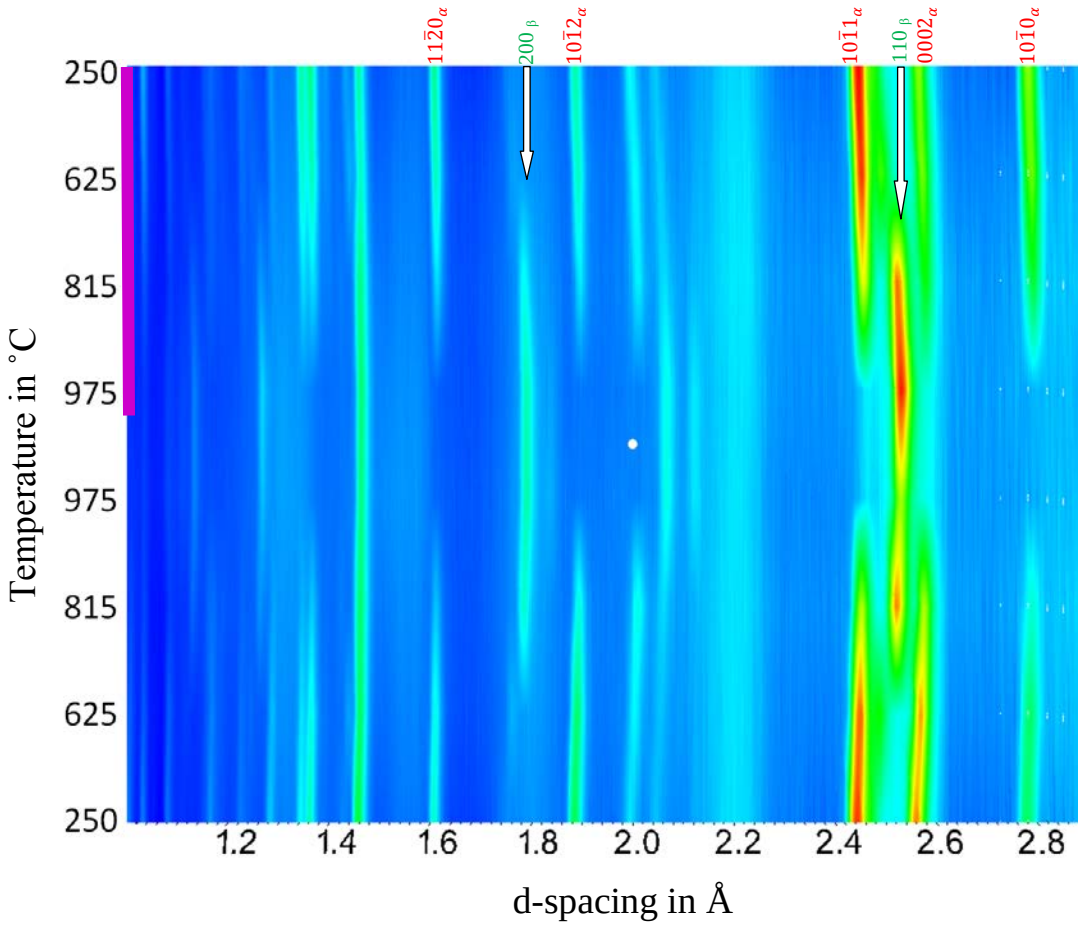

Figure 5.4: Peak intensity as a function of temperature and lattice parameter spacing of Zr-2.5Nb integrated over all 90˚ detectors and all sample orientations. The top half of the plot (marked with the magenta bar on left) represents data after compression.

We can nicely see the β-phase emerging between 625˚C and 815˚C as, for instance the 200 β-phase Bragg reflection appears. During compression and dropping temperatures, the β-phase disappears again between 815˚C and 625˚C. Similar, between 815˚C and 975˚C the α-phase disappears, as indicated by e.g. its $10\bar{1}1$ reflection vanishes and reappears during cooling in the same temperature range. As an effect of the sample compression at 975˚C the 110_β reflection intensifies.

For a more comprehensive investigation of the crystallographic changes in the sample, it is advantageous to look at each detector panel individually, so we obtain 45 histograms, i.e. individual observation directions, as compared to five from the five detector rings (see section 3.1). By rotating the sample around its vertical axis to four distinct angles, we obtain $4 \cdot 45 = 180$ unique histograms from which we obtain the ODF and thus the texture of the sample material. Figure 5.5 shows this texture for the α-phase in the left column and for the β-phase phase in the right column. The Zr-2.5Nb was measured at room temperature with the sample changer (a) before and (f) after heating and 20% strain in the axial direction, which is the original extrusion direction shown about the center. The radial direction is horizontal and the hoop direction vertical. Revelation of critical factors influencing this material's texture is provided by *in-situ* measurements (b) through (e) using the presented creep furnace. Pre- and post-treatment conditions of the sample are confirmed in (a/b) and (e/f), respectively. The Burger orientation relationship determines the transition of $(0002)_{hcp/\alpha}$ to pole density maxima in $(110)_{bcc/\beta}$ during a temperature increase to 975˚C. The resulting textures at high temperature are shown in (c). The $\{222\}_{\beta}$ planes align with the applied compression direction (d).

Lattice parameters for both phases and their weight fraction are recorded in Table 5.2, which have been calibrated with X-ray data from [99]. These X-ray room temperature data were extrapolated using phase and axis specific thermal strain values published in the literature [100].

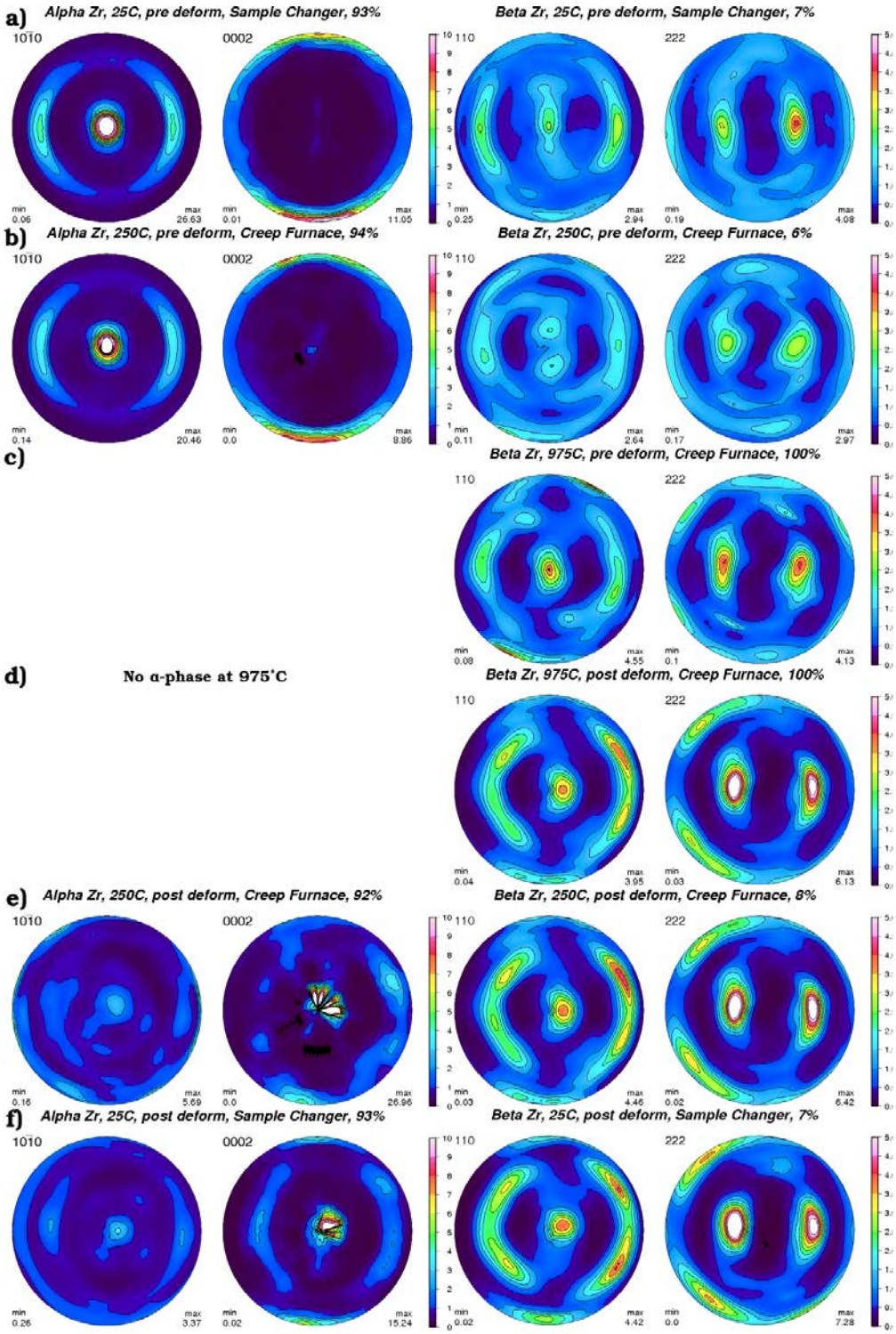

Figure 5.5: Texture evolution of α-phase (left column) and β-phase (right column) of Zr-2.5Nb throughout the heat and stress treatment. Figure originally published in my paper [79].

Table 5.2: Lattice parameters and volume fractions of both phases as a function of temperature and uni-axial stress are tabulated, calibrated by X-ray data from [99]. Only significant digits of lattice parameters are shown, as analysis error < 10^{-4}.

	As Received				20% Uni-axial Compression			
Temperature	250˚C	625˚C	815˚C	975˚C	975˚C	815˚C	625˚C	250˚C
α phase a-axis in Å	3.2327	3.2390	3.2409	--	--	3.2460	3.2414	3.2342
α phase c-axis in Å	5.1576	5.1766	5.1937	--	--	5.1894	5.1824	5.1638
β phase a-axis in Å	3.5218	3.5498	3.5985	3.6100	3.6119	3.5996	3.5519	3.5286
β phase wt. fraction	0.06	0.08	0.38	1.00	1.00	0.44	0.14	0.08

5.6 Discussion

The α-phase texture in the sample changer (Figure 5.5, (a) and (f)) reveals the same features as the 250˚C measurement conducted in the creep furnace, ibid (b) and (e). The β-phase texture varies slightly, likely more noticeable due to its low phase fraction of 7 ± 1 wt% at this temperature, and, as such, exhibits higher statistical fluctuations. Sample composition at room temperature and 250˚C was determined from the Rietveld data analysis of the experimental data to be 93 ± 1 wt% α-Zr and 7 ± 1 wt% β-Zr. This agrees with previous results from Li et al. [94] and Fong et al. [92] who found a β-Zr weight fraction slightly below 10% for this sample material below ~620˚C. Heating this sample to 975˚C reveals the complete transformation to the β-phase (as predicted by [101]) in conjunction with a sharpening of the β texture relative to the ambient results. This phase transformation proceeds according to the Burger orientation relationship (BOR), where $\{0002\}_\alpha$ planes transform into $\{110\}_\beta$ planes [51], visible, for instance, by the pole density maxima along the rim at 1 and 7

o'clock of the 0002_α pole figure in (b) and 110_β in (c). The strong 110_β axial component that appears, shown in (c), indicates variant selection due to the internal stresses, as discussed in [4], though here potentially also slightly influenced by the light external clamping and holding force on the order of 30 N. Data acquisition was carried out immediately after applying 20% strain at a constant displacement rate of 0.32 mm/s (an approximate strain rate of 0.016/s at the start of the test, rising to 0.04/s by the end of the test) at a constant temperature of 975˚C. The {111} lattice planes realign toward the compression direction, visible in the β-phase 222 pole figure in (d). This is expected for a bcc material deforming predominantly by ⟨111⟩ slip [51]; simulations constrained by our experimental data will be required to determine the relative contribution of climb and diffusion in accommodating the deformation. On subsequent cooling the β-phase reverts back to its original 7 ± 1% weight fraction, but maintains the same texture as at 975˚C, suggesting that all β orientations transform with a near equal probability back to α. Also all of the six observed diffraction maxima in the 110_β pole figure, emphasized in (e) revert back to the strong 0002_α component in (e) and (f) according to BOR, but with a preference for the loading and clamping direction. This means, variant selection occurs during cooling. Even in absence of a clamping force a similar selection occurs [4].

Slightly higher β-phase weight fractions during cooling (Table 5.2) are likely due to a hysteresis effect, probably associated with diffusion of Nb. The weight fractions agree with data published by Fong et al. [92]. With time-of-flight neutron diffraction

relative changes in the lattice parameter can be determined rather precisely, as can be seen by the small standard deviation (Table 5.2) calculated by MAUD.

Thermal strains computed from the lattice parameters in Table 5.2 are shown in Figure 5.6 and compared with experimental results on the same alloy reported by Fong et al. [91], as well as with literature values for the thermal expansion of the crystallographic *a* and *c* axes of pure Zr. Combining the new information gained from the compression with the lattice parameter from the β-Zr, we obtain Figure 5.7. For comparison purposes I down-scaled the β-phase by a factor of three. As this figure is based on the lattice parameters of Table 5.2, derived from a Rietveld fit of all detector

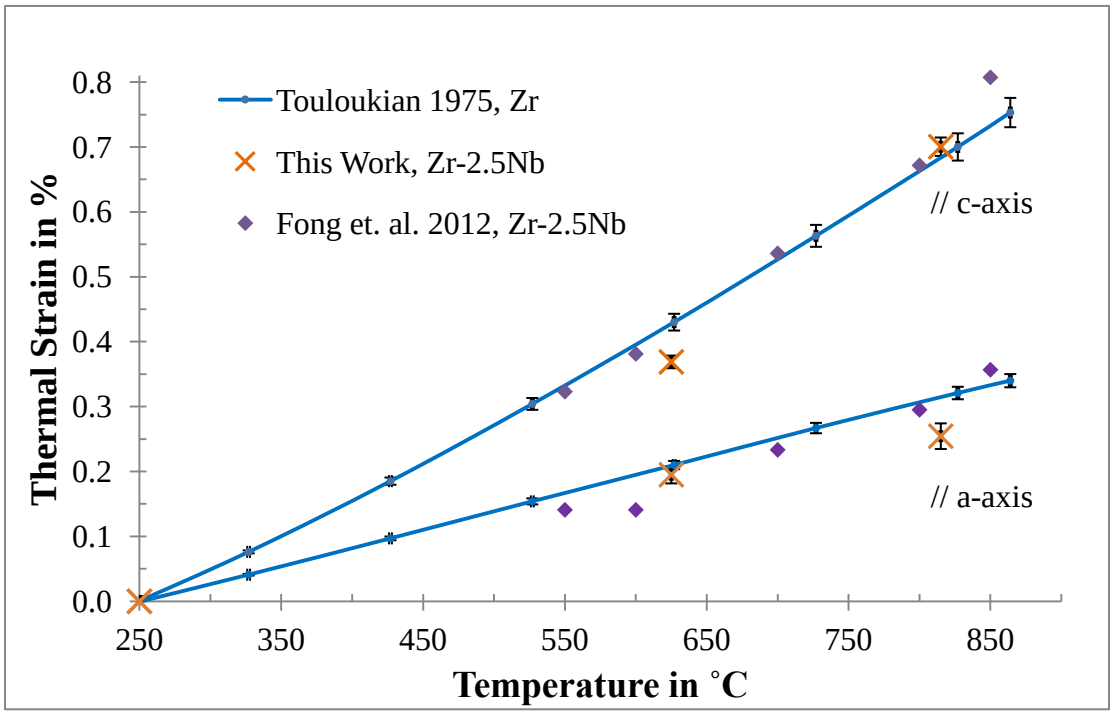

Figure 5.6: Relative changes of lattice parameter for a-axis (bottom) and c-axis (top) of α-Zr given in Table 5.2. The experimental results of Zr-2.5Nb from this work are in good agreement with Fong et al. [91] and literature values for pure Zr [100]. Figure originally published in my paper [79].

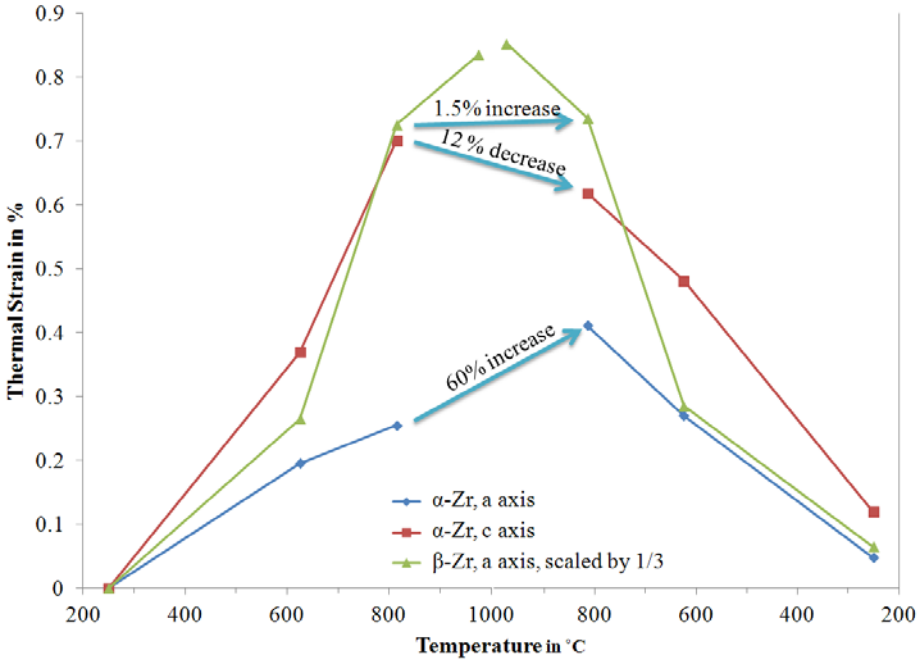

Figure 5.7: Thermal strain for the crystallographic *a* and *c* axes of α-Zr. The β-Zr *a* axis is also shown, but downscaled by a factor of three for comparison.

angles, it is noteworthy that the resulting thermal strains are not direction (or hkl) dependent, but rather represent an average over the bulk polycrystal.

Comparing the strains at 250˚C at the end of the experiment with those from the beginning, an average deviation of 0.077% is apparent. A similar offset can be noted in the β-phase at 975˚C, comparing strains before and after the compression. Both of these offsets can be explained with the observed buckling of the sample. Therefore, the amount of deviation introduced by buckling in the system is of the order of 0.1% strain. Distortions in the α-phase at 975˚C obtained by comparing strains before and after compression clearly exceed this value. It is of particular interest to note the opposite changes of both axes. While the thermal strain of the *a* axis increases by

60%, a 12% decrease in the *c* axis of the hcp crystal occurs. Reasons for this behavior need further modeling to resolve the underlying mechanisms.

5.7 Conclusion and Outlook

The room temperature measurements, before and after deformation at high temperature, clearly demonstrate the necessity of such a sample environment as the creep furnace, capable of investigating phase transitions at elevated temperatures and deformation-related texture evolutions *in situ.* This allowed for experimenters to deconvolute the contributions of heating, phase transformation during heating, deformation at temperature in the β field, and phase transformation during cooling. Comparing only the pole figures of Figure 5.3, those recorded with the sample changer at room temperature, individual factors such as heating, phase transition, compression, and cooling cannot accurately be differentiated and as such their individual influence on texture evolution would remain ambiguous.

Variant selection has been observed during the α→β transformation due to anisotropic thermal expansion of the α–phase, as well as during the β→α transformation due to sample compression during the experiment, simulating extrusion. Texture changes of individual thermo-mechanical manufacturing steps have been quantified and can be used to benchmark and constrain future mechanical models in order to predict the material behavior. Thermal strains of the α–phase have been calculated from the Rietveld fit and agree with values published by Fong et al. [91] for this alloy, as well as literature values for pure Zr [100].

In general, *hkl* dependent lattice strains (with *hkl* being the Miller indices of the lattice plane), i.e. the tracking of reflection dependent peak shifts, provide the foundation of strain pole figures [102] which grant insight into the three-dimensional mechanical response of a polycrystalline aggregate and represent an extremely powerful material model validation tool. From these lattice strains one can also derive the macroscopic average stress and strain tensors [103], [104], [105], [106]. Such *hkl* dependent lattice strains are available from each detector panel recording diffraction data. Our setup therefore probes a large number of sample directions, providing a vast amount of constraining experimental data for such models.

Areas that can be improved are the signal-to-noise ratio as can be seen e.g. from Figure 5.4. As the sample expands during heating, the lattice planes expand and hence diffraction peaks shift to higher d-spacings creating a curvature. Also, as the sample experiences a phase transformation, peaks from the low-temperature phase disappear and those of the new phase emerge. Hence, diffraction peaks that are on a straight continuous line throughout the entire experiment are not from the sample and need investigation to be avoided. Examples are the strong peak at 1.42 Å in Figure 5.4 or less intense peaks at ~2.2 Å.

Due to the sample's large heights to diameter ratio of 20 mm / 6 mm = 3.33, the sample buckled when compressed by 20%. Future samples should be chosen to have a ratio of ~1 when 20% strain is desired.

6.0 *IN SITU* CARBOTHERMIC REDUCTION OF URANIUM DIOXIDE

For the first time, a redox reaction between uranium dioxide (UO_2) and graphite powder is observed with neutron diffraction *in situ* up to temperature of 2000˚C by utilizing the novel high-temperature furnace described in section 4.3 in combination with the HIPPO diffractometer (section 3.1). UO_2 is reduced between 1441 and 1650˚C and forms uranium monocarbide (UC). Upon further heating, more carbon diffuses into the NaCl-type crystal structure forming a cubic UC_2 lattice. Above 1800˚C, a novel experimental observation is made suggesting a second order order-disorder transition with broad transition region. Based on an innovative synthesis using uranyl acetate and calcium as the reducing agent, the employed UO_2 powder is comprised of ~80 nm particles, which seems to raise the UC formation temperature.

6.1 Motivation

Thermodynamic properties of uranium carbides (UC_x) are of special interest for a deeper understanding and the prediction of in-reactor fuel performance as well as reactor safety calculations for current nuclear reactors and future Generation IV reactors. Temperatures in excess of 1850˚C have been predicted [22], [23] as the fuel centerline for these reactors, which demands extensive study of the fuel properties at these temperatures. The interest in uranium carbides is based on their high melting points, lack of phase transformations at normal operating temperatures and dimensional stability under irradiation (all of which apply also to UO_2) coupled with

a considerably higher thermal conductivity (Figure 6.1) and higher fissile density than UO_2 [107]. Metallic uranium is typically avoided as a nuclear fuel due to its low melting point of 1135˚C as compared to UO_2 and UC_x with melting points in excess of 2500˚C.

Neutron diffraction was recommended by various authors as the probe of choice for UC and UO components. Martin [110] reviewed 15 different studies regarding the coefficient of thermal expansion (CTE) of UO_2 measured by macroscopic length changes and lattice parameter measurements using X-ray and neutron diffraction. He determined results of studies performed with the latter technique to be most accurate. Frost [107] confirms that the position of the carbon ions in uranium carbide are easier to determine with neutron diffraction, as opposed to XRD, since both materials scatter

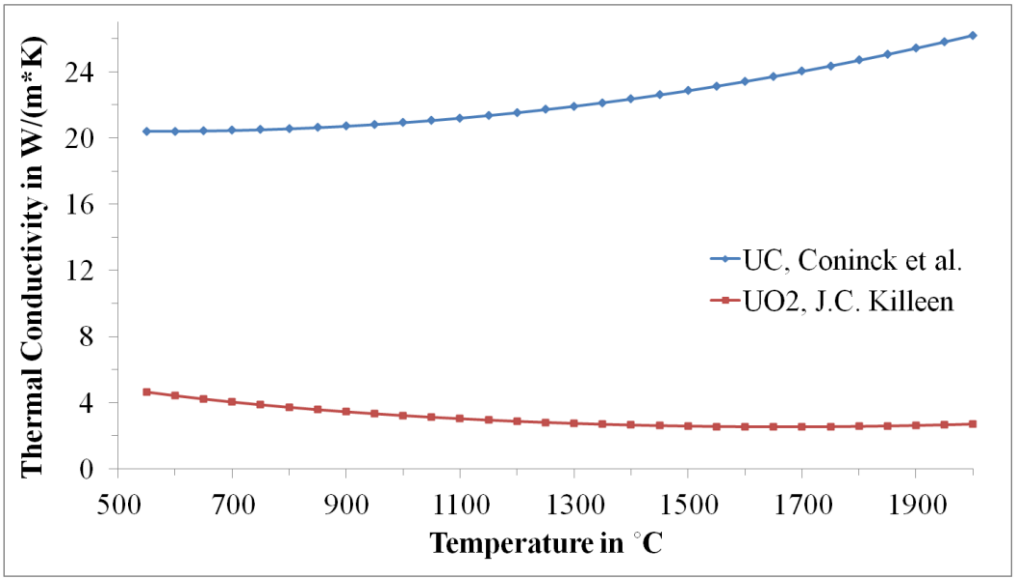

Figure 6.1: Thermal conductivity of stoichiometric UC and $UO_{2.0}$ (fully dense) as a function of temperature, based on [108] and [109].

slow neutrons about equally well (coherent cross section for natural U is 8.9 b and natural C is 5.5 b). Thus, neutron diffraction is the investigative tool of choice to examine crystallographic changes in the carbothermic reduction of UO_2 to form UC_x. This chemical approach has the additional benefit of avoiding pyrophoric hazards involved when handling metallic uranium powders.

Avoiding structural changes of the fuel during its lifetime is beneficial as internal stresses, cracks, etc. are reduced. Within a 100 to 200 μm thick outer layer of reactor fuel pellets, originally 10 to 20 μm large UO_2 grains subdivide into ~1000 grains of less than 1 μm size after about $2 \cdot 10^{21} \frac{fissions}{cm^3}$ (about 8.5% burnup) at low temperatures [111]. Because the physical and chemical properties of UO_2 powders is expected to be particle size dependent [112], we studied the behavior of nanoparticle UO_2 fuel pellets. Our novel approach of using uranyl acetate to synthesize UO_2 powder without the use of irradiation [113], [114] or nitrates [115] is also different from the reaction by Wang et al. [116] in that we used calcium instead of ethylenediamine as the reducing agent. Benefits are a highly stoichiometric result of the synthesis in combination with the ability to produce larger quantities.

In situ high temperature data for uranium carbide are sparse. The *Inorganic Crystal Structure Database* (ICSD) collected by *Fachinformationszentrum* (FIZ) Karlsruhe [82] lists 51 entries of uranium carbide structures, 15 of which refer to the high-temperature UC_2 structures. Whereas 12 describe the quenchable tetragonal UC_2 ε-phase; only three deal with the non-quenchable [117] cubic UC_2 δ-phase stable between 1769˚C and 2560˚C. Remarkably these three experiments by Bowman et al.

[118] (investigated using neutrons), Wilson [119] (X-ray diffraction (XRD)) and Bredig [117] (XRD) originating in the early 1960's reveal conflicting results which have not been clearly resolved. Despite these works being the basis for nuclear reactor-relevant thermodynamics calculations [120], [121], there has not been (to the best of my knowledge) a more recent study to unambiguously determine the crystal structure of the cubic UC_2 δ-phase.

As X-rays are not very sensitive to the carbon sublattice in the presence of uranium atoms, neutrons are the preferred choice, which I illustrated by comparing simulated diffraction patterns with a unit cell size of 5.41 Å in Figure 6.2. With the high-temperature furnace described in section 4.3, I can achieve the required temperature range *in situ* and determine which of these three published structures is correct.

6.2 Metallurgical Characteristics and Background

Carbon occurs in its stable form at ambient conditions as diamond, graphite and various fullerenes. In diamond, the bonding throughout the crystal is covalent with the tetrahedral sp^3 hybridization. In graphite and in the fullerenes, covalent bonds with sp^2 hybridization hold the atoms in the layers or molecules while van der Waals forces hold layers and molecules together. While the atoms of graphitic layers (graphene) are constrained in a hexagonal lattice, different polytypic forms are possible that differ in the way the layers are stacked over one another. There are four distinct polytypes of graphite, known as 1H, 2H', 2H, and 3R, but only the latter two

(Figure 6.3) have been found in nature. The hexagonal unit cell of 2H graphite consists of four atoms, whereas the rhombohedral unit cell of 3R has only two.

Metallic uranium between ambient conditions and 668˚C forms the orthorhombic α-phase. The tetragonal β-phase changes into the bcc γ-phase at 776˚C before

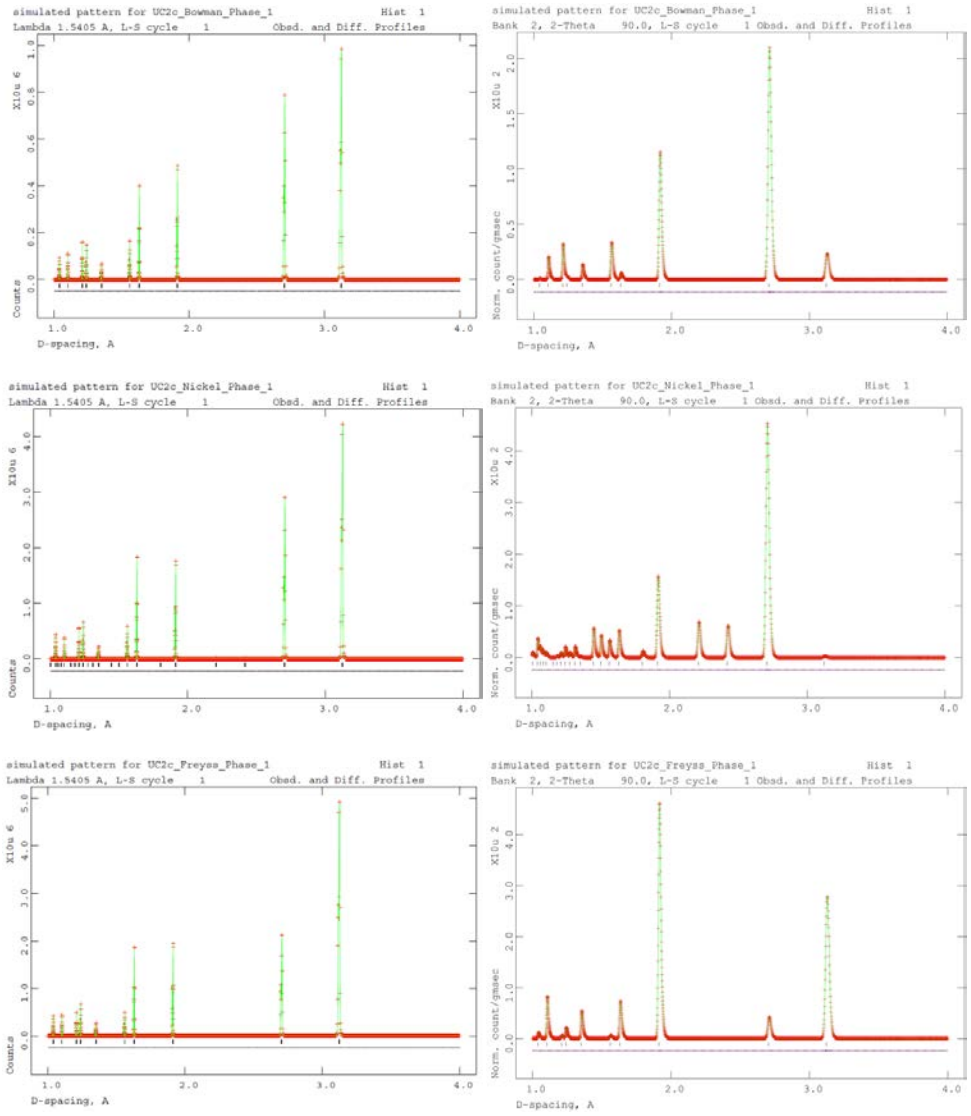

Figure 6.2: Simulated XRD (left column) and neutron diffraction (right column) patterns for cubic UC_2 according to Bowman et al. (top), M.A. Bredig (middle) and W.B. Wilson (bottom) showing the superiority of neutron diffraction to determine the structure of the cubic UC_2 phase

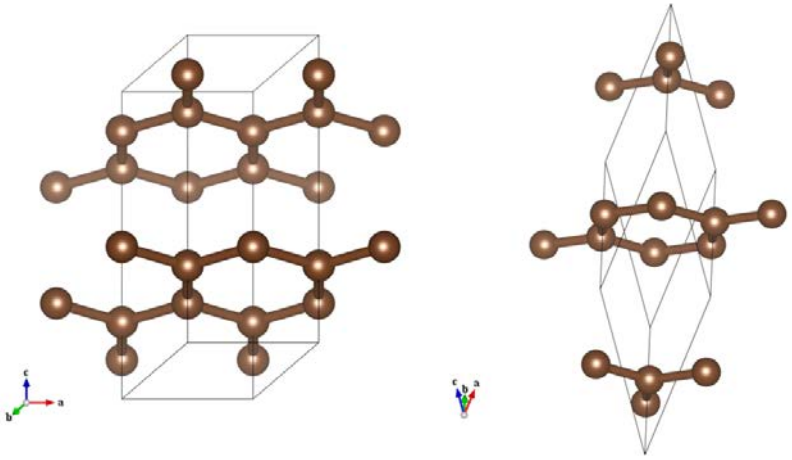

Figure 6.3: Crystal structure of graphite 2H (left) and 3R (right). Excess atoms beyond the unit cell (black outline) are drawn to aid visualize the layered structure.

uranium melts at 1135˚C. More details to metallic U are covered in section 2.4.2.

Binary carbides, the group of compounds of which UC_x is a member, exhibits a unique combination of metallic transport properties with very high melting points, brittleness and hardness characteristic of ceramics. These can be fabricated by casting or, more commonly, sintering (solid state compaction). Casting produces grain sizes larger than 100 μm, high density (98-99% theoretical) and low interstitial impurity content (~ 100 ppm), while sintered powders have a finer ~ 10 μm grain size, lower density (90-95% theoretical) and a higher interstitial impurity content (~0.1-0.5%) [107]. With 75 at% carbon in our sample we are in the carbon rich, right side of the uranium-carbon phase diagram in Figure 6.4. During the reaction of UO_2 forming UC, carbon is lost in the form of CO_2, as shown later, reducing the sample carbon content to 67at%. Uranium carbide phases are given in Table 6.1.

Table 6.1: Structures of uranium carbide phases

Phase	Structure Form	Space Group	Structure Type	Structure
δ	UC_x	$Fm\bar{3}m$	NaCl	Face centered cubic
ζ	U_2C_3	$I\bar{4}3d$	Pu_2C_3	Cubic
ε	UC_2	$I4/mmm$	CaC_2	Body centered tetragonal

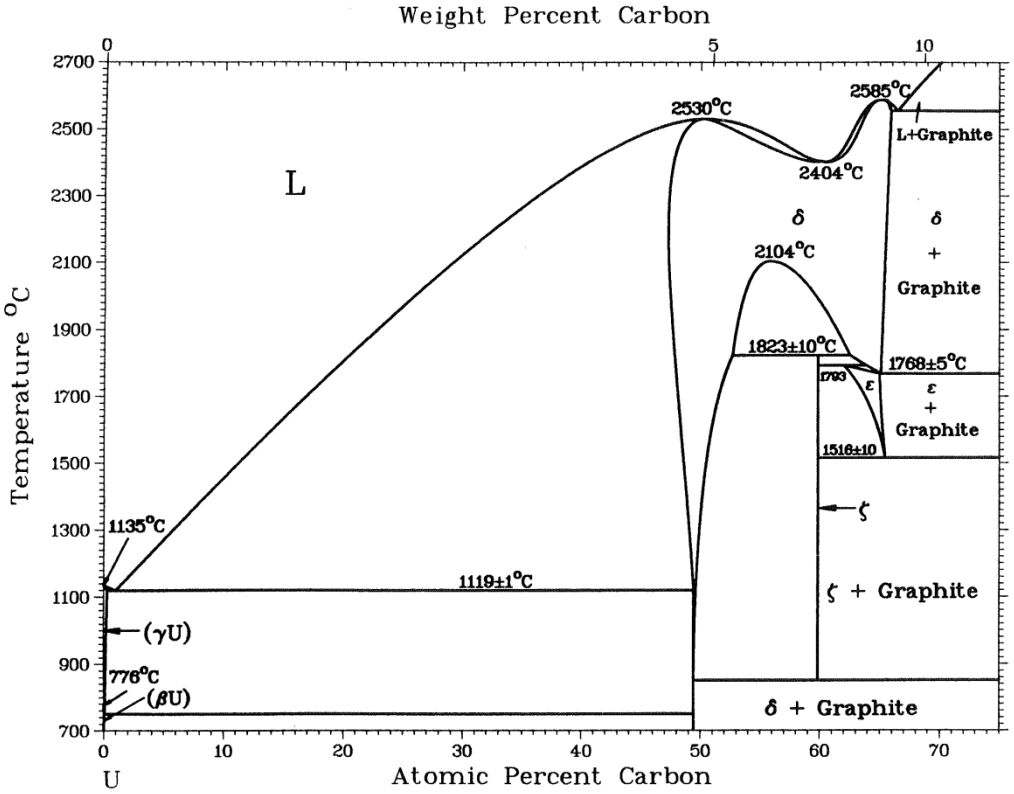

Figure 6.4: U-C Phase diagram showing the tetragonal ε-UC_2 phase and the cubic δ-UC_x phase on right [122].

Simulated neutron diffraction patterns for UC_x and UO_2 specific for the HIPPO diffractometer together with their unit cell structures are shown in Figure 6.5.

The δ-phase exists for UC_x as a solid solution, with *x* varying between 0.9 and 1.95, according to the phase diagram. For the temperature range between 1768˚C and 2560˚C, three opposing crystal structures for this phase have been published in ICSD listed in Table 6.2 with their unit cells shown in Figure 6.6. The fluorite-type structure, first proposed by Wilson in 1960, is sometimes attributed to two other names; Chang [123] who in 1961 solely reiterates Wilson's results or Freyss [121]

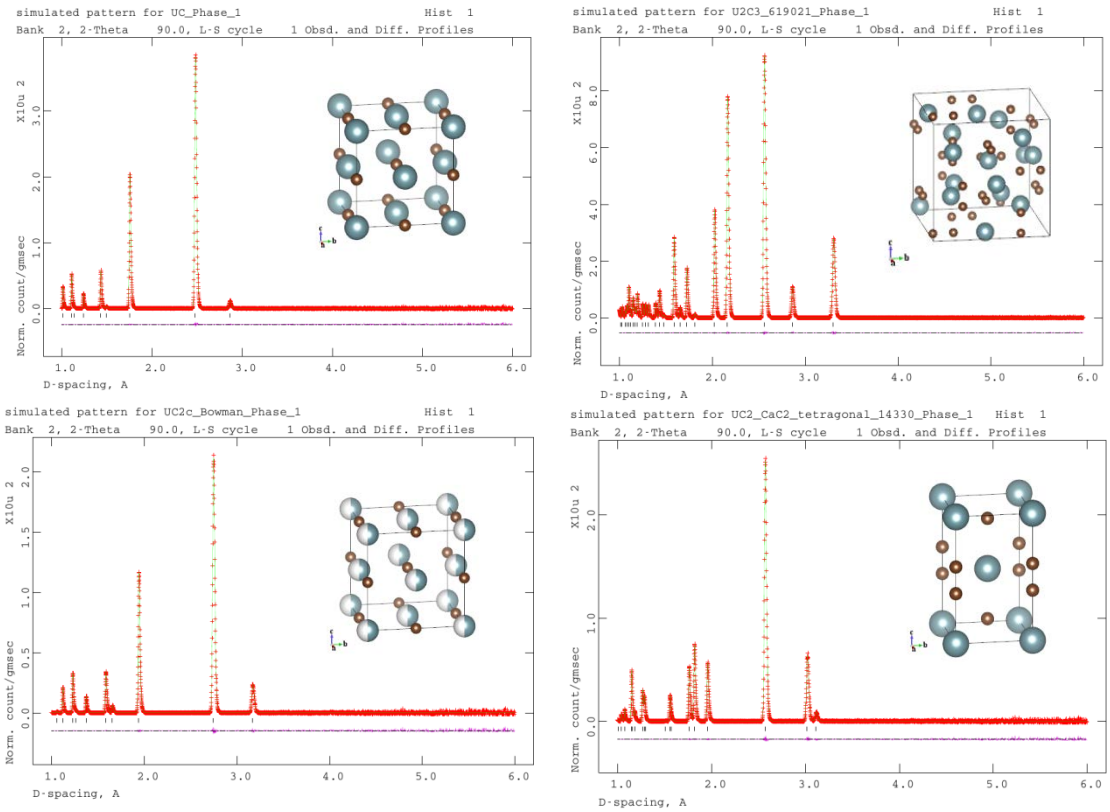

Figure 6.5: Overview of simulated diffraction patterns with unit cell structure of (clockwise, starting top left) UC, U_2C_3, UC_2 tetragonal, UC_2 cubic (according to the ICSD approximation of results from Bowman et al.).

Table 6.2: List of all experimentally 'identified' and published structures for the cubic UC_2 phase collected by ICSD. Wilson is listed as Freyss; Bredig as Nickel and Saeger.

	Space Group	Structure Type	Pearson Symbol	Cell Size	Observation Temperature
Bowman et al.	$Fm\bar{3}m$	Defect NaCl*	cF8	5.488 Å	1900˚C
Wilson, W.B.	$Fm\bar{3}m$	CaF_2	cF12	5.410 Å	1820˚C
Bredig, M.A.	$Pa\bar{3}$	FeS_2	cP12	5.472 Å	1820˚C

*Although listed as $U_{0.5}C$ in the ICSD, Bowman actually proposed UC_2 with C_2 molecules on the C sites of the NaCl structure, following the motion of a free rotator model or a random disorder model (oriented along [111] direction).

who in 2010 calculated a first-principle study listed in ICSD. The pyrite-type structure, first proposed by Bredig in 1960, is listed in ICSD as Nickel and Saeger [124] who in 1968 lists this structure-type.

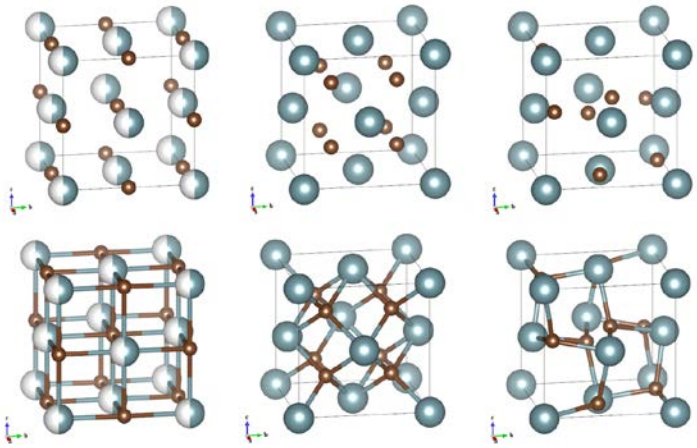

Bowman et al. Wilson,W.B. Bredig, M.A.

Figure 6.6: Unit cells with uranium (turquoise, large) and carbon (brown, small) atoms of three different crystal structures published for the cubic UC_2 phase both with (bottom) and without (top) bonds emphasized. Uranium atom positions in defect NaCl crystal structure published by Bowman et al. (left) as approximated by ICSD are only half occupied.

In the database of American Society for Metals (ASM) International, only Bowman's rock-salt (NaCl) type structure is referenced and joined to all listed works, including e.g. Wilson, who actually proposed the fluorite type-structure.

The UO_2 unit cell with space group $Fm\bar{3}m$ possesses a fcc cation lattice with eight interstitial oxygen ions of the CaF_2 structure type. Partial oxidation at ambient conditions leads to the coexistence of the U_4O_{9-y} phase (Figure 6.7), which denotes a derivative of the fluorite type structure, where clusters of interstitial oxygen atoms

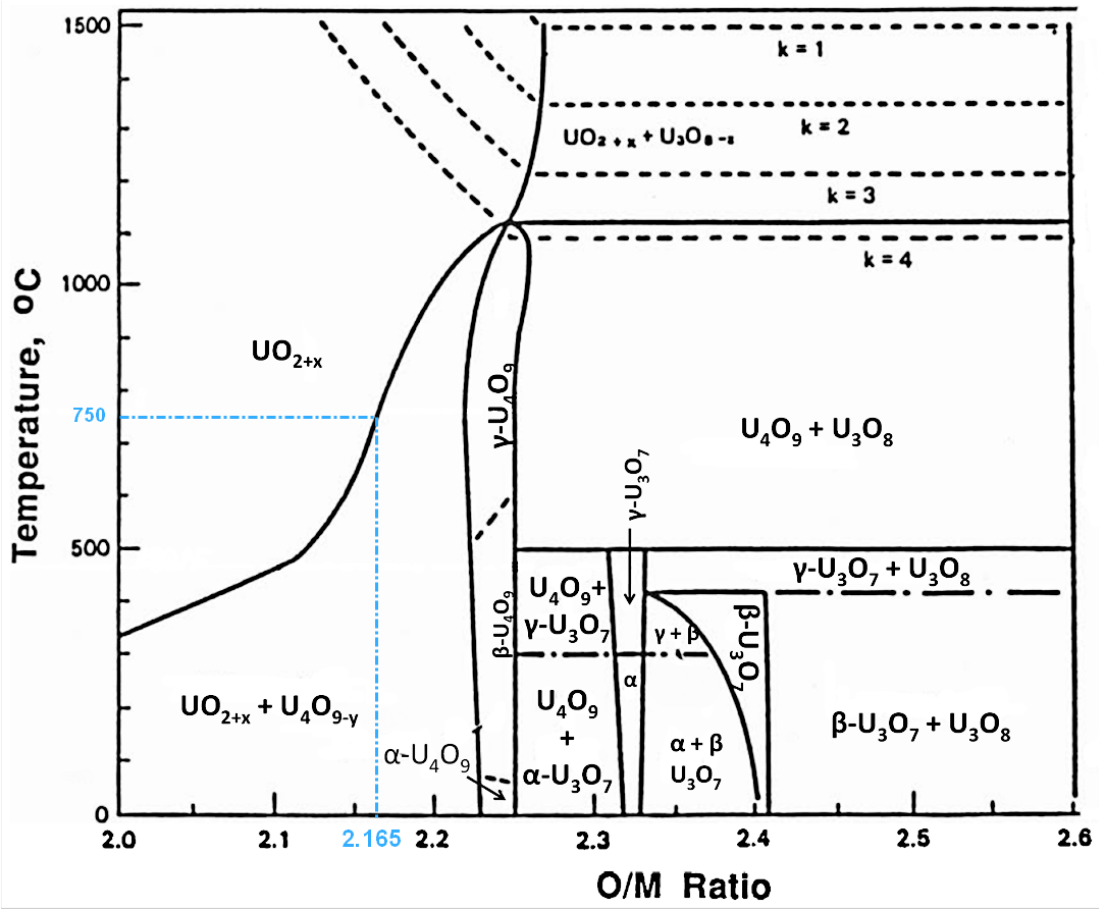

Figure 6.7: Oxygen to metal ratio as a function of temperature for urania [125]. The observed transition temperature for my sample with corresponding O/M ratio is marked with the dashed blue line.

center on unoccupied cubic sites in the lattice, with accompanying displacement of neighboring U atoms [126]. Formation of U_4O_9 from UO_2 involves a volume reduction of ~2.04%. This has been calculated from the ratio in unit cell volume of U_4O_9 with 10260.75 $Å^2$ [127] over UO_2 with 163.67 $Å^2$. The latter volume has to be multiplied by 64, as there are four replications of the UO_2 unit cell along each side of the U_4O_9 unit cell.

A summary of Bragg reflections for a d-spacing range larger than 1.5 Å is provided for the relevant phases of this experiment in Table 6.3. This will aid understanding and a single point of reference for the following discussion of results.

Table 6.3: List of Bragg reflections >1.5 Å for ambient conditions with d-spacing in Angstrom in combination with Miller indices for the relevant phases.

	h	k	l	d-spacing
2H Graphite	0	0	2	3.35550
	1	0	0	2.13389
	1	0	1	2.03356
	1	0	2	1.80063
	0	0	4	1.67775
	1	0	3	1.54405
3R Graphite	1	1	1	3.38468
	1	0	0	1.95131
	1	1	0	1.85144
	2	2	2	1.69234
	2	1	1	1.56534
UO_2	1	1	1	3.15811
	2	0	0	2.73500
	2	2	0	1.93394
	3	1	1	1.64927
	2	2	2	1.57905
UC	1	1	1	2.86423
	2	0	0	2.48050
	2	2	0	1.75398

6.3 Experimental Setup

A. Sample Preparation

Applying a force of 450 MPa generated by a weight of ~ 9 tons (20,000 lbs), a mechanically mixed sample was pressed into a 16 mm in diameter and 4 mm high pellet consisting of 12.5 mmol UO_2 powder (3.375 g) and 37.5 mmol graphite powder (0.45 g). Thus, a mixture of UO_2 and 75 at% or 13.15 wt% C with a mole ratio of C/UO_2 = 3 was achieved. To increase structural integrity, 60 mg of Naphthalene ($C_{10}H_8$) were added to the sample. The 99.999% pure graphite with grain size < 7 μm was obtained from Alfa Aesar. The UO_2 powder was synthesized at LANSCE as a result of preparing an aqueous solution of uranyl acetate by dissolving 4.24 g (10 mmol) of uranyl acetate dihydrate in 100 ml of H_2O. A stoichiometric amount of calcium (4.1 g, 10 mmol) was slowly added to the uranyl acetate solution under vigorous stirring. Uranium trioxide precipitated as an orange solid while Calcium acetate remained in solution. After filtration and washing with water, the orange cake of uranium trioxide hydrate was re-suspended in a small amount of boiling water, filtered and washed again. Suspension in boiling water followed by filtration was repeated until no more calcium was detected in the filtrate. The solid material was then placed in a vacuum oven at 120˚C overnight to produce anhydrous uranium trioxide. This material is a fluffy orange powder, which is largely amorphous to X-ray. The yield is nearly quantitative upon precipitation, but a substantial amount of

material is lost during washing and filtration owing to the slight solubility of UO_3 in water.

UO_3 was reduced to UO_2 by placing it into an alumina boat and heating it to 400-500˚C in a tube furnace under a gentle stream of 6% hydrogen in argon gas mixture. Heating was continued for a minimum of 4 hours. The (mostly black) powder in the alumina boat was then stirred in the boat and placed back in the tube furnace for an additional 2 hours at the same temperature under H_2/Ar gas flow. The resulting powder was extremely fine and showed only uranium dioxide under X-ray diffraction. X-ray fluorescence showed no residual calcium. The material oxidizes over time from standing in air and could end up being slightly hyperstoichiometric, at the time of the experiment.

In order to determine the particle size of the UO_2 powder we dispersed less than 1 mg substance on a double sided Cu tape joined to an Al SEM slab. The SEM was conducted in a model Magellan^3 400 build by FEI Company. A 'cauliflower structure' (Figure 6.8) indicating nano-scale particles is observed equivalent to UO_2 fuel with 45GWd/t burn-up [111]. Thus, a second sample for a TEM investigation was prepared by suspending less than 1 mg of UO_2 in HPLC grade acetone. Sonicating the sample in a glass veil immersed in an ultrasonic bath dispersed the nano particles evenly in the liquid. A 3.05 mm in diameter Cu grid with a carbon coating on the opposite side was wetted four times and evaporated. The TEM analysis in a model Tecnai G^2 F30 from FEI Company confirmed the particle size to be ~80 nm (Figure 6.9).

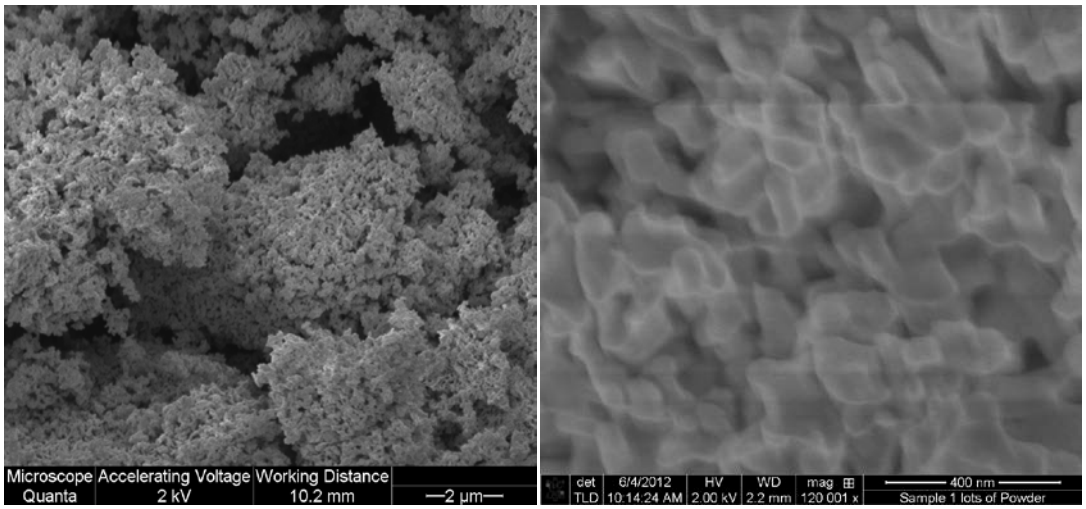

Figure 6.8: SEM of UO_2 powder sample prior to high-temperature experiment showing 'cauliflower' structure (left) and particle sizes of ~80 nm (right).

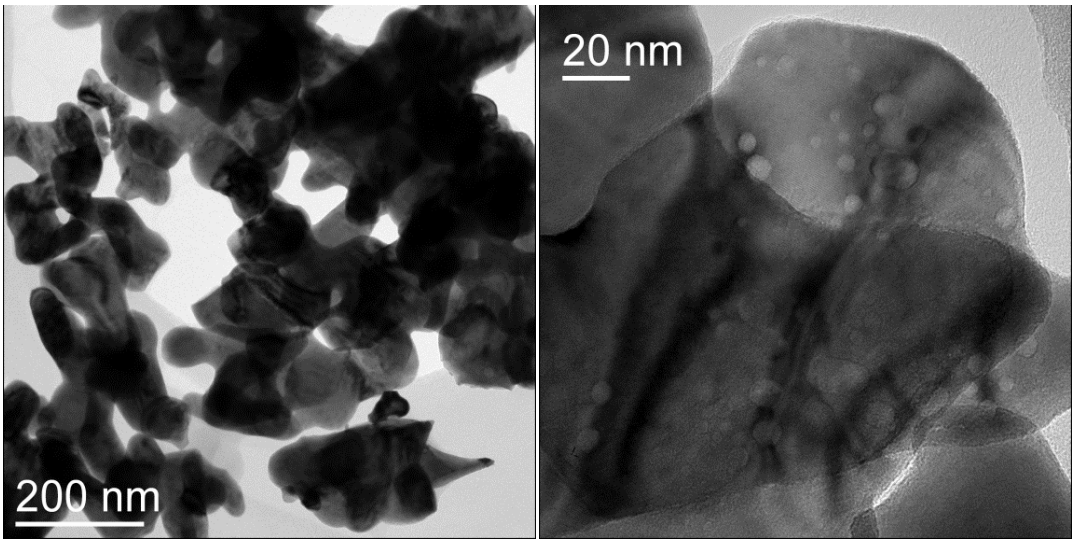

Figure 6.9: TEM of UO_2 powder sample prior to high-temperature experiment confirming particle sizes of ~80 nm (left) and revealing inclusions or void spheres of ~8 nm diameter (right).

B. Furnace Preparation

The high-temperature furnace described in section 4.3 was carefully aligned using neutron radiography in combination with the image plate portrayed in section 3.4. A collimation of the neutron beam to 4 mm diameter using borated poly provided a beam spot of ~7 mm at the ~1 m distant sample position caused by beam divergence. The absorption cross section for natural boron is 767 b due to the natural abundance of 20% of the isotope ^{10}B with 3835 b, and thus, represents an excellent collimator material. This setup produced the best signal-to-noise results and was chosen to remain in place for the entire experiment. Figure 6.10 shows four neutron

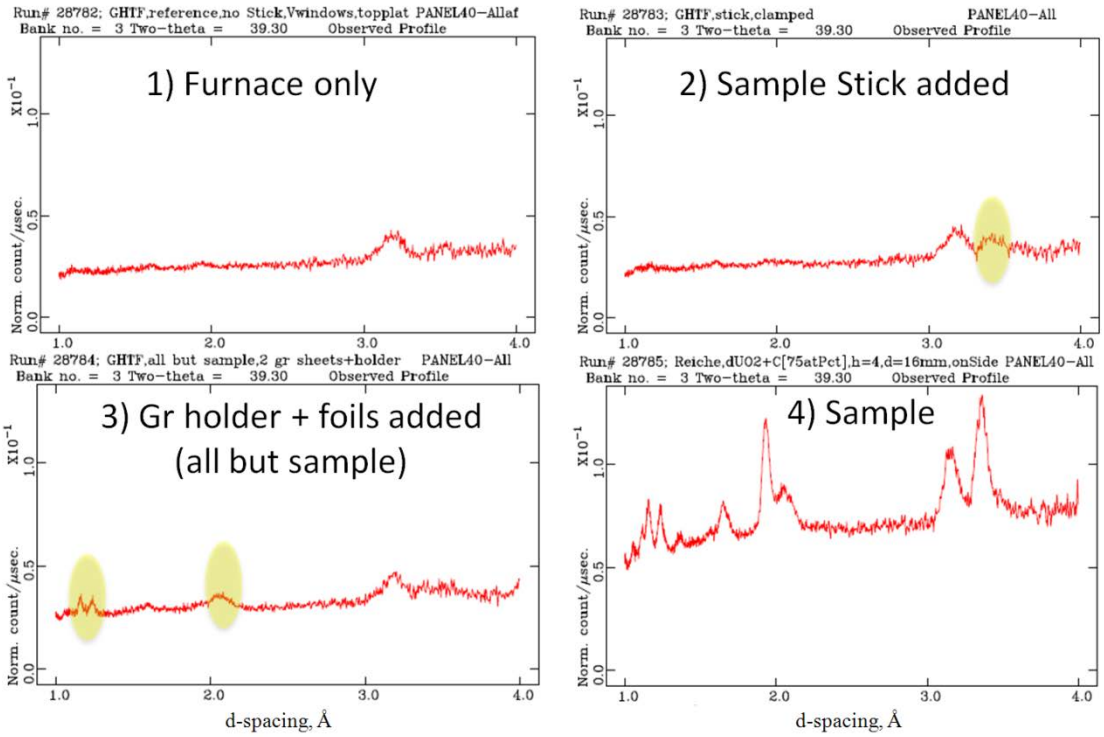

Figure 6.10: Raw neutron spectra of sample alignment, highlighting (yellow) small contamination of sample stick (top right) and graphite sample holder (bottom left).

diffraction spectra as a reference for the degree of alignment. First, I obtained a spectra for the bare furnace (1), sequentially adding the sample stick (2), which provides a graphite platform for a custom machined graphite holder and a pair of thin (0.25 mm) graphite foils (3) positioning the sample (4) on its side, coaxially to the neutron beam. While the holder features a convex slit that prevents the sample from rolling out of position, the foils sandwich the sample to prevent accidental contamination of the furnace in case the sample fractures or melts. As the alignment shows, despite the foils being irradiated by the direct neutron beam, the diffraction contribution appears to be tolerable.

I collected isothermal diffraction data for 30 min every 250˚C between 250˚C and 2000˚C. The 30 min were collected as six 5 min data sets to enable the study of kinetics. During heating with 10˚C/min, data in 2 min intervals were collected. The previously achieved *ex situ* temperature of 2200˚C was not reached owing to a chiller malfunction which dictated to terminate the experiment prematurely during the 2000˚C measurement. The actual experiment, excluding setup and alignment, was completed in ~11 h.

C. Data Analysis

As most of the data sets have been collected during non-isothermal conditions, with a mere two-minute of neutron integration time, the statistical error was minimized in two ways. For the data refined with gsaslanguage [39], we employed a moving average over five data sets prior to the refinement process as shown to be

effective by [128]. Single peak fits, on the other hand, are calculated from individual, not averaged data sets followed by a median. This five-value wide filter sorts the recorded neutron counts of the same d-spacing range of five successive runs and returns the middle, i.e. third element. As a result, no new values are created and events (e.g. the formation of a new phase, indicated by a sudden rise in intensity) are not smeared out, but remain untouched at the temperature originally recorded. Noise less than three values broad is not flattened but eliminated which smoothes the graph significantly, as proven by Vogel et al. [129].

Data were analyzed using Rietveld refinement. Individual runs at isothermal conditions were integrated to increase statistics and analyzed with the MAUD package. A total of 147 recorded data sets were analyzed utilizing a script-based approach in combination with either SMARTSware [130] code which utilizes GSAS to perform a single peak fit or gsaslanguage to refine the entire spectrum. The latter custom sequential script models up to four phases simultaneously, namely 2H graphite, 3R graphite, UO_2 and U_xC with the site occupancy x ranging between 0.5 and 1, describing UC_2 and UC respectively. The intermediate phases U_2C_3 and the tetragonal UC_2 phase were not found (which is in agreement with [124], [131]) and thus removed from the final script. To make the fit more robust we constrained the isotropic thermal motion parameter U_{ISO} of both graphite phases to move alike, which is reasonable to assume as they describe identical atoms in similar local environments. The thermal motion of the uranium atoms in UO_2 and UC are constrained, as well as oxygen and carbon ions of the two aforementioned phases as

they only vary by 3 u in atomic number. Moreover, the analysis refines lattice parameter and thus, unit cell volume, phase fraction and peak width of each phase. Results of one data set initialize the refinement of the next set. To increase the credibility of the sequential analysis, an additional calculation in reverse order (data set 147 to 1) was also performed. I chose to show results of only one analysis direction, because the final results usually are virtually identical, and to improve figure clarity. The most robust refinement was achieved by first varying the phase scales followed by the lattice parameters in sequence of declining weight fraction or phase scale. A third refinement step varies the peak width for each phase in an equally sequenced fashion. A forth step refines the thermal motion parameters and lastly, the uranium site occupancy in the U_xC phase.

6.4 Post Heating Results from the Sample Changer

From a first Rietveld analysis including texture refinement I concluded that the grains were randomly oriented, as very minimal texture was evident from the results. This is expected, because the sample was formed from powder at a uniform temperature without introducing anisotropic external stimuli during the experiment. Thus, I merged the diffraction spectrum recorded at room temperature into five histograms, equivalent to the five detector rings of the diffractometer. A histogram recorded by the 150˚ backscattering detector panels of HIPPO, including Rietveld fit, is shown in Figure 6.11. The Rietveld refinement determined a sample composition of 96 wt% UC, 3 wt% UC_2 tetragonal phase with rest 2H graphite. It is likely that the

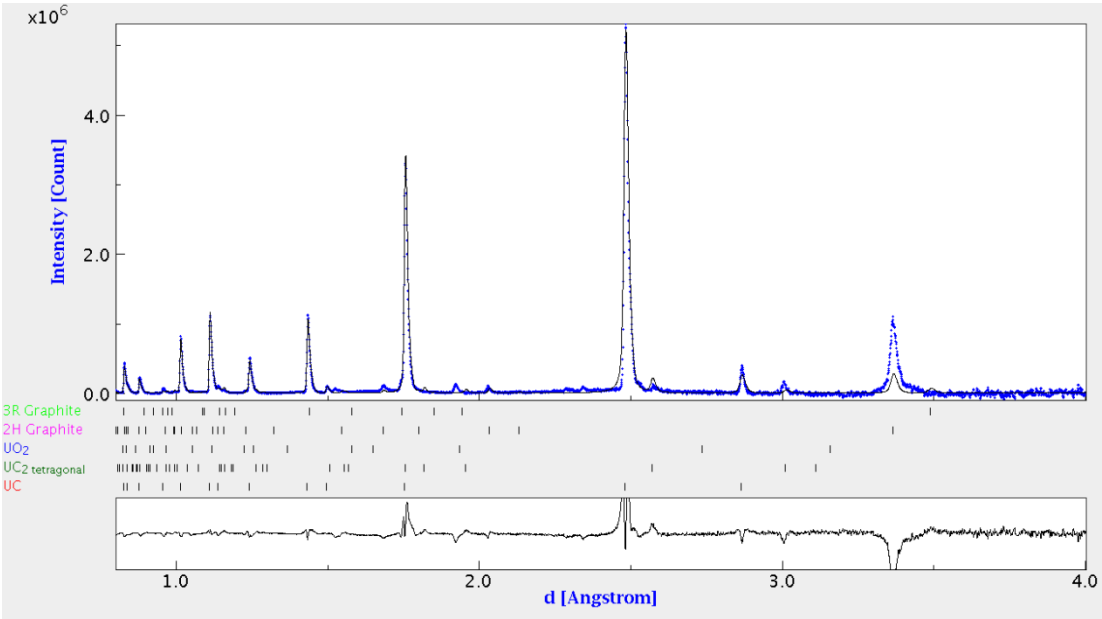

Figure 6.11: MAUD refinement for post-heat data of 145˚ detector (interpreted analogous to fit in Figure 5.2).

observed 1 wt% 2H graphite originates not from the sample itself, but one of the two graphite foils to sandwich the sample. One of these reacted with the sample and could not be fully removed before the measurement in the sample changer. No cubic UC_2 phase can be detected in the sample confirming that this phase is not quenchable as predicted by Bredig [117]. Neither UO_2 nor 3R graphite is found in the sample as both fully transformed to UC.

6.5 Results from Elevated Temperatures using the High-Temperature Furnace

As a qualitative overview of the experimental results conducted in the high-temperature furnace serves Figure 6.12. Recorded histograms from the 40˚ detectors are normalized, reflections color coded and accumulated, one line representing one

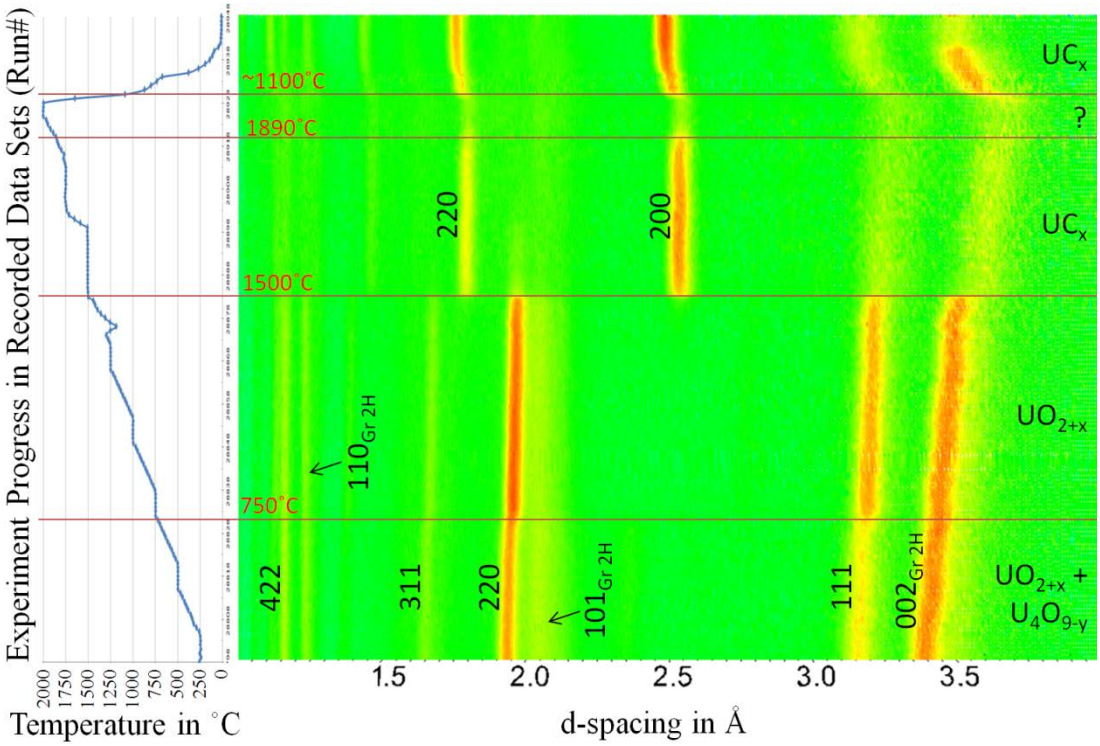

Figure 6.12: The contour plot shows observed intensity as a function of experiment progress (y-axis) and d-spacing based on data recorded form the 40˚ detectors. The graph on left correlates experiment progress with the sample temperature.

data set. The transition temperature where graphite and UO2 reflections disappear and UC reflections emerge is evident ~1500˚C. Reasons for the vanishing of the UC peaks around 2000˚C will be elaborated in the next section.

6.6 Discussion

A. The cubic UC_2 structure

For an unbiased interpretation which crystallographic structure best describes the phase between 1768 and 2560˚C, I integrated all recorded neutron diffraction data at 2000˚C. Using MAUD, I entered all three reported UC_2 structures in combination

with the UC phase with an equal share of 25 vol%. As the UC structure is very similar to the UC_2 Bowman structure, both are added to avoid that a possibly existing UC phase in the sample is misinterpreted and fitted with the UC_2 Bowman model. To provide an equal basis, I matched the lattice parameters for all phases to 5.08 Å, letting the strong 200 reflection of all four phases overlap, as well as setting the thermal motion (*B-factor)* in MAUD to 1 $Å^2$. Figure 6.13 (top) shows the region of interest recorded by the 40˚ detectors, as these phases predict different peak intensities and peak positions for the d-spacing range between 2.2 Å and 3.1 Å. A phase fraction refinement of the entire data set (full d-spacing and detector coverage) with lattice parameters constrained, results in a sample composition of 78wt% of Bowman's NaCl type structure, 12 wt% UC, 9 wt% Wilson's fluoride and 1 wt% Bredig's pyrite type structure. Additional refinement, allowing the lattice parameters to vary as well, results in 97 wt% of Bowman's structure (Figure 6.13) with a lattice parameter d = 5.071 Å and the remaining 3 wt% almost equally distributed over the remaining phases. This result can be explained as only the Bowman phase has a high intensity reflection, the 200 at 2.72 Å and a lower intensity reflection, the 111 at 3.14 Å in the adequate relation to fit the recorded data.

The CaF_2 type structure proposed by Wilson also seems to be very improbable on chemical grounds, as it would imply a breaking of the C-C bonds of the C_2 ions that exist with an interatomic distance of 1.34 Å in the tetragonal phase [132]. If such breakage occurred in the cubic phase, where the C-C distance is 2.72 Å, the cubic structure should be quenchable as the formation of the bond represents a major

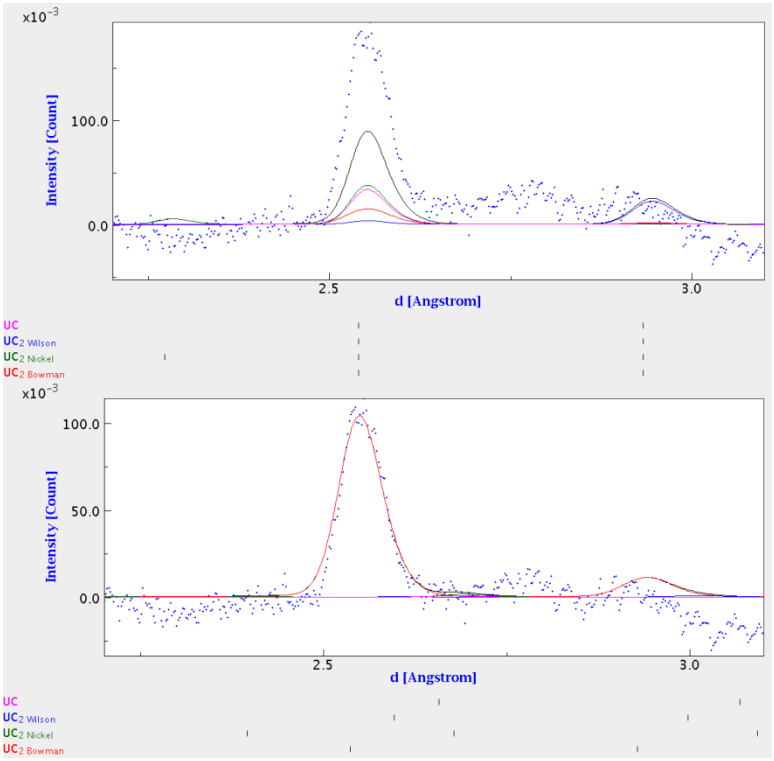

Figure 6.13: Neutron intensity as a function of d-spacing scaled from 2.2-3.1 Å to show details of the significant peaks of the uranium carbide sample at 2000˚C. The three proposed structures for cubic UC_2 plus UC start equally with 25vol% (top). MAUD refinement results in 97wt% of Bowman's NaCl structure (bottom).

crystallographic change in the solid [117], which has not been observed. The existence of the solid solution between UC and the cubic UC_2 phases further substantiates this argument of similitude between these phases, both of the NaCl-type structure.

B. Uranium Sesquicarbide and Tetragonal Uranium Dicarbide

Phase diagrams describe the formation of phases at a specified temperature after equilibrium conditions are achieved. Equilibrium phases will only materialize if the

temperature remains inside a phase formation regime long enough to satisfy the reaction kinetics.

Between 850˚C and 1516˚C the phase diagram indicates a formation of uranium sesquicarbide ($U_2C_{3)}$, the ζ-phase; however this reaction proceeds with a very slow rate. Nickel et al. [124] observed with a high carbon content sample of 8.9 wt%, closest to our sample with 13 wt%, no detectable amount of U_2C_3 after 1.5 h at 1350˚C, 'some' after 70 h and 'a lot' after 235 h. Because the UO_2 was not reduced until 1500˚C, the remaining ~1 h at a temperature within the ζ-phase range was insufficient to form U_2C_3.

Between 1516˚C and 1768˚C the phase diagram predicts the formation of tetragonal ε-phase UC_2. The sample traversed this temperature range within 55 min without showing detectable evidence of the UC_2 tetragonal phase. In agreement with this observation, Mukerjee et al. [131] reports for an identical sample composition of mole ratio $C/UO_2 = 3$ no occurrence of this phase after 15 h.

C. Graphite and Contamination

Based on the lattice parameters refined from the sequential analysis, we obtained *a* and *c* lattice parameters of both graphite phases (Figure 6.14). Pyrolytic graphite from the literature seems to describe a good middle of these phases.

At the commencement of the experiment both forward and reverse Rietveld analysis determine a total of 10.5 wt% graphite (6.1 wt% 2H and 4.4 wt% 3R) for the sample at room temperature. This matches the sample composition of 13.15 wt% (75

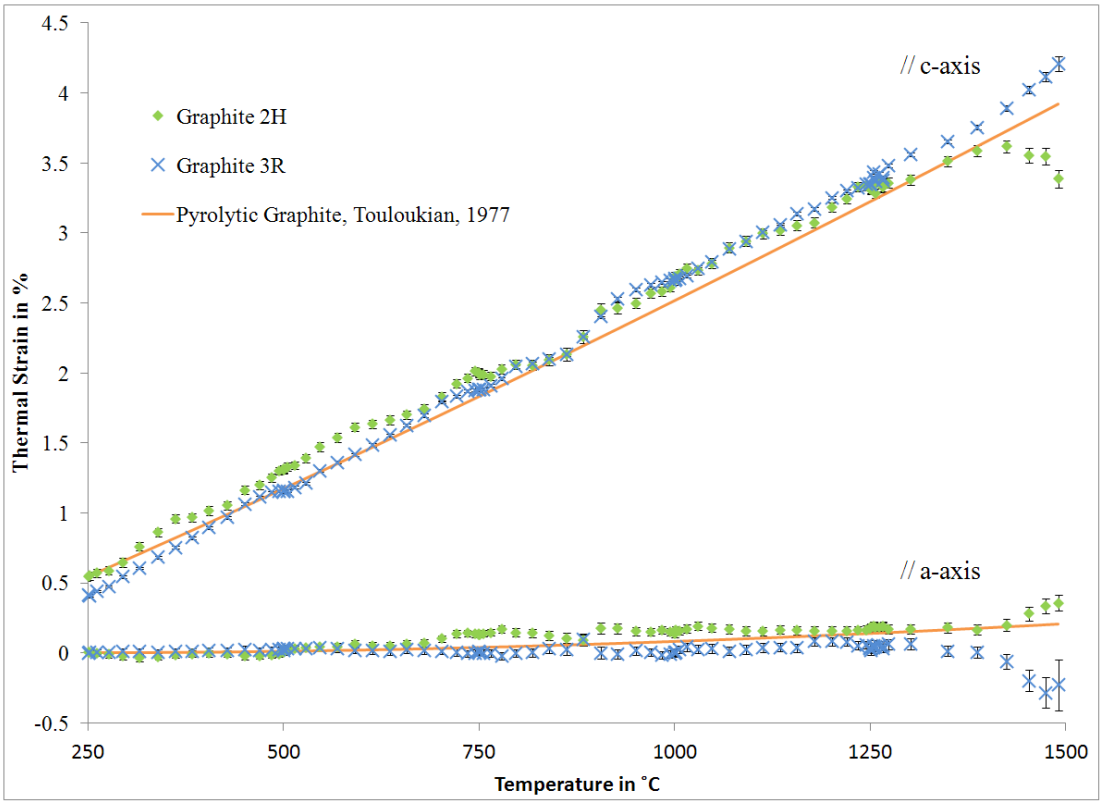

Figure 6.14: Thermal strain of lattice parameter for in-plane a-axis (bottom) and out-of-plane c-axis (top) of observed graphite phases 2H and 3R compared with literature values [133] for pyrolytic graphite.

at%) graphite closely. This, in combination with the earlier discussed alignment (Figure 6.10), further confirms that the graphite foils employed to secure the sample in place, have a small contribution to the diffraction pattern.

The two reflections above 3 Å in the overview plot that are present throughout the entire experiment (Figure 6.12) do seem to stem from graphite contamination, either a 002 reflection of 2H graphite or a 111 reflection of 3R graphite. Prior to the uranium carbide formation at ~1500˚C these are overshadowed by the sample materials, a 111 UO_2 reflection and a 002 2H graphite reflection. Since the undesired

~3.4 Å reflection is so close to the 2H graphite reflection of the sample, it seems likely for these two materials to be spatially adjacent to each other, as neutrons diffracted not from the sample position, are detected with a noticeable shift in d-spacing. A confirmation for this reflection to originate from the platform of the sample stick is that it first appeared when the sample stick was measured empty during alignment (Figure 6.10, top right). The second undesired reflection at ~3.2 Å seems to originate from the graphite heat shield in the furnace, as it was visible even in the empty furnace pattern (Figure 6.10, top left). The peak is shifted by ~0.2 Å relative to the aforementioned possible graphite reflections. According to Equation 3.3, this d-spacing shift recorded in the 40˚ detectors correlates to a displacement of 8 cm away from the sample. Due to the strong angle dependence of Equation 3.3, this d-spacing shift should vary with the recorded detector bank if it really originates from a displacement error. The shift in the 145˚ backscattering detectors should be as little as 0.07 Å and as much as 0.27 Å in the 60˚ detectors. This prediction indeed matches the recorded data confirming the origin of the 3.2 Å reflection to be the downstream heat shield, i.e. between sample and beam stop.

D. Uranium oxides

The two dominant urania reflections 111 and 220 at 3.158 Å and 1.934 Å respectively, increase in intensity around 750˚C as shown in the overview plot (Figure 6.12). The reason for this is that UO_2, when stored under atmospheric conditions, slowly becomes hyperstoichiometric (UO_{2+x}) and even forms U_4O_{9+y} as a

second phase at ambient condition. Depending on the composition, it reverts back to the single phase UO_{2+x} at a unique temperature depending on the oxygen to metal ratio (O/M) shown in diagram (Figure 6.7). As simulated neutron diffraction patterns in Figure 6.15 prove, the transformation of U_4O_9 to UO_2 is indeed characteristic of an increase of the two aforementioned reflections. Further, as two phases (UO_{2+x} and U_4O_{9+y}) merge, a likely slight offset of their reflections converges, resulting in increased intensity and a more narrow peak width of the new single phase reflections.

The exact transition temperature is determined by a single peak fit of the region ±0.3 Å surrounding the 220 reflection. In order to accurately subtract the background, the neighboring 101 reflection of the 2H graphite phase needs to be fitted simultaneously, but only the results of the UO_2 peak are incorporated into the calculation and shown in Figure 6.16.

A first intensity increase of the urania peaks occurs at 720˚C, with the completion of the process 24 min later at 750˚C. According to the O/M diagram

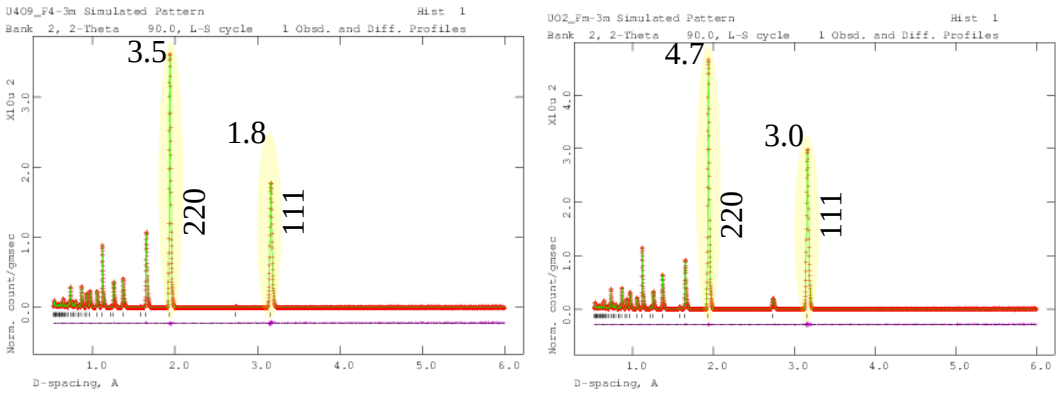

Figure 6.15: Simulated diffraction pattern for U_4O_9 (left) and UO_2 (right). The two significant diffraction peaks are stronger in the UO_2 pattern, namely reflection 111 by 34% and 220 by 67%.

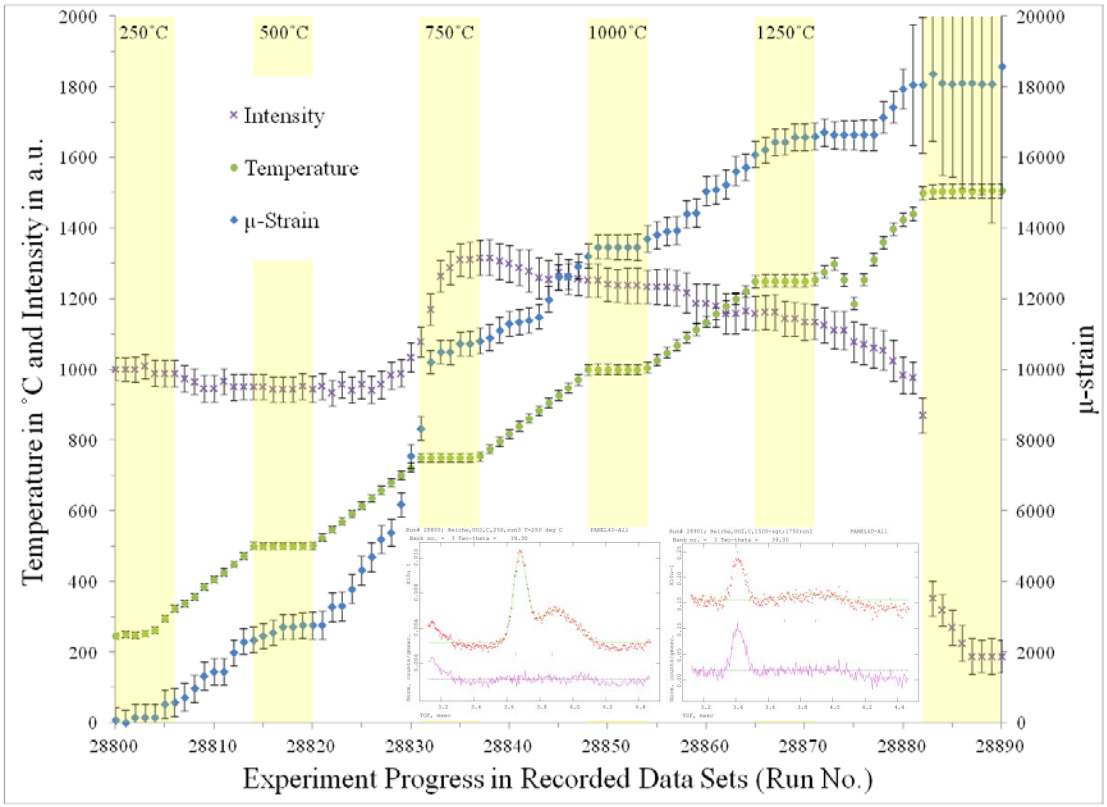

Figure 6.16: Results from single peak fit for 220 reflection at ~1.9 Å of UO_2 with temperature profile showing isothermal measurements shaded in yellow. Reduction of UO_{2+x} and U_4O_{9-y} to single phase UO_{2+x} occures around run 28834 at 750˚C and transformation into UC around run 28883 at 1500˚C. The left inset shows the Rietveld fit at the beginning of the graph (run 28800, 250˚C), with the tall 220 UO_2 peak and the broader 101 Graphite 2H peak to its right. By run 28901, 1650˚C, both have vanished and the material formed UC, evident by the 220 UC peak in the right inset.

(Figure 6.7) we can conclude that the maximum oxygen content of our sample is therefore UO_{2+x} with $x \leq 0.165$. The value cannot be larger, as the transformation of U_4O_{9+y} to UO_{2+x} is complete at 750˚C. The value of *x* could be smaller, as possibly the reaction is slow and perhaps started unnoticed at a lower temperature.

Thermally activated, oxygen atoms diffuse out of the urania crystal causing an increase in both volume and thus lattice parameter, as indicated by the increasing µ-

strain in Figure 6.16 and in accordance with [134], [135]. The sequential analysis substantiates this transition temperature by a sudden increase in d-spacing as well as a drop in the thermal motion parameter U_{ISO} (Figure 6.17). The drop occurs as the sample oxygen content approaches stoichiometry represented by the model used for the fit. A lattice parameter increase of 0.44% (error < 10^{-4}) is manifest at 750˚C which corresponds to a volume increase of 1.314%. As mentioned in section 6.2 the volume increase from pure U_4O_9 to UO_2 is 2.04%. Thus we can conclude to have 1.314 / 2.04 = 64.3% U_4O_9 in our sample below 750˚C. Since U_4O_9 can be re-written as $UO_{2.25}$ we have a sample stoichiometry of $0.643 \cdot 2.25 + (1-0.643) \cdot 2.00 = 2.1608$ based on the observed volume increase; very similar to the aforementioned U/O ratio of 2.165 based on the UO_{2+x} reduction temperature.

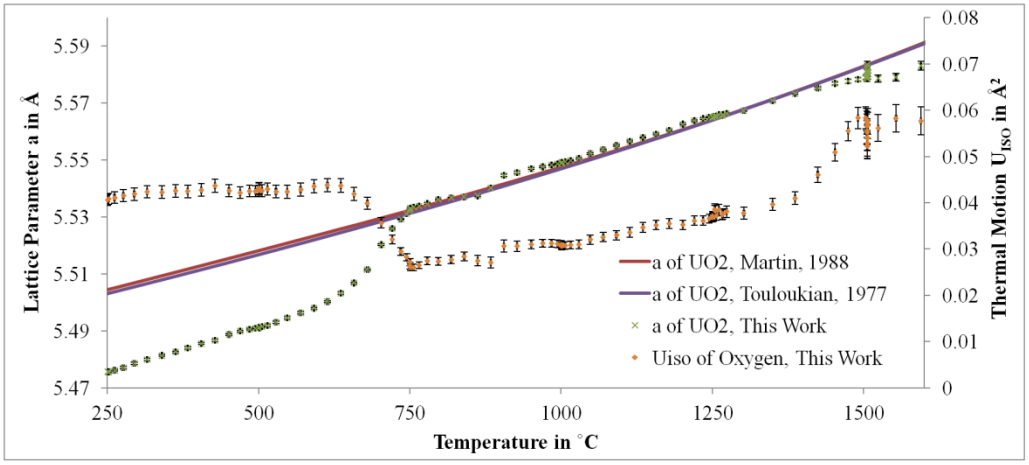

Figure 6.17: Reduction of UO_{2+x} with x~0.16 to UO_2 at 750˚C is evident through a volume increase and thermal motion decrease of the UO_2 model. Thermal expansion of UO_{2+x} (750-1500˚C) matches literature values from Martin [110] and Touloukian [133] closely.

The thermal expansion in the range of single phase $UO_{2.16}$ (750 to 1500˚C) is compared with a review by Martin [110] and literature by Touloukian [133] in Figure 6.17. The recommendation by Martin is valid only for a stoichiometry of UO_{2+x} with *x* values in the range of 0-0.13 and 0.23-0.25. For the temperature range 750 to 1500˚C our CTE values for UO_{2+x} match the literature well. Below 600˚C, I fitted a linear function determining the CTE of our two phase urania to be $\alpha=6.3601\cdot10^{-5}\ K^{-1}$.

An SEM prior to the experiment (Figure 6.8) reveals the particle of my urania powder to be ~80 nm. A reduction in peak width is indicative of increasing grain size. Without a careful calibration, taking into account, for instance, line broadening from the sample shape or instrument specific contributions, a precise quantitative assessment of the grain size in the sample is not possible. Below the transition temperature to single phase UO_{2+x} (~750˚C) Figure 6.18 reveals a linear decrease in peak width revealing linear grain growth. Above this temperature, the peak width

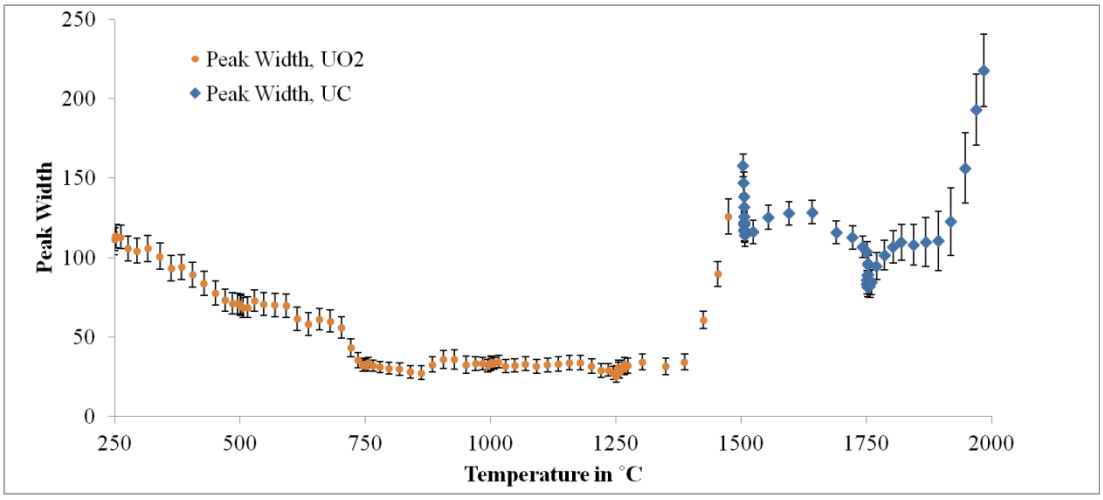

Figure 6.18: Peak width calculated from the sequential refinement for UO_2 and UC_x.

remains constant. It is unclear (though likely) that grain growth continued above 750˚C. However, possibly the resolution limit of the instrument is met at this point, preventing an observation of further decrease in peak width.

As the statistical error for both, the full width at half maximum (FWHM) and the peak position are high once the peak intensity dropped, the single peak fit of Figure 6.16 could have potentially provided a wrong result. As a proof, that indeed all the UO_2 has been completely consumed, the insets in Figure 6.16 show the fit range. The left inset shows the commencement of the experiment at 250˚C and the right inset proofs completely vanished UO_2 peak at 1650˚C in combination with the appearance of the 220 UC peak at 1.8 Å (TOF=3.4 ms). The complete consumption of UO_2 is substantiated by the post heating measurement using the sample changer (Figure 6.11) verifying the absence of the characteristic 111 reflection expected at 3.2 Å ().

E. Uranium Monocarbide

Concurrently, the carbon and UO_2 content in the sample start to decline at 1441˚C and are completely vanished at 1650˚C (Figure 6.16), while the UC phase appears, following the redox transformation

$$UO_2 + 2C \rightarrow UC + CO_2 \tag{3.4}$$

As shown through chemical analysis of quenched samples by Mukerjee et al. [131], the carbon content declines in agreement with this reaction equation predicting the discharge of CO_2 gas. As a reaction temperature just below 2000˚C is indicated by the literature [136], I did not employ a slower temperature profile to investigate this event

in more depth. The bulk portion of this transformation completed at 1500˚C, as indicated by the intensity drop of the 220 UO_2 peak (Figure 6.16). For an, with my sample, identical mole ratio of $C/UO_2 = 3$, Mukerjee et al. [131] determined a transformation onset at 1300˚C with completion at 1500˚C with e*x situ* measurements. Onset and completion are both ~150˚C lower than observed here. While the particle size of UO_2 is not mentioned in Mukerjee et al., the reacted graphite is two orders of magnitudes finer as compared to my sample. Because the roles of each reactant are unclear, I can only conclude that grain-size seems to effect the transformation temperature.

The carbon dioxide generation indicated by Equation 3.4 was also noticeable as a slight hump in the vacuum graph. The selected sample composition with a ratio of three carbon atoms per uranium is thus ideal for the selected experiment. Up to a third of the carbon atoms could escape the sample in the form of CO_2, leaving two carbon atoms per uranium behind, providing sufficient carbon atoms for the transition from UC to UC_2 at high temperature.

The thermal microstrain of UC has been derived in two ways: from a single peak fit of the 200 reflection and with the sequential refinement of the full spectrum leading to quantitatively different results (Figure 6.19). In both cases, the reference strain is the room temperature lattice parameter *a* with 4.961 Å. Single peak fits have shown to be useful in calculating transition temperatures, but the dimensional change in a unit cell should be far more accurate when considering the full d-spacing range of

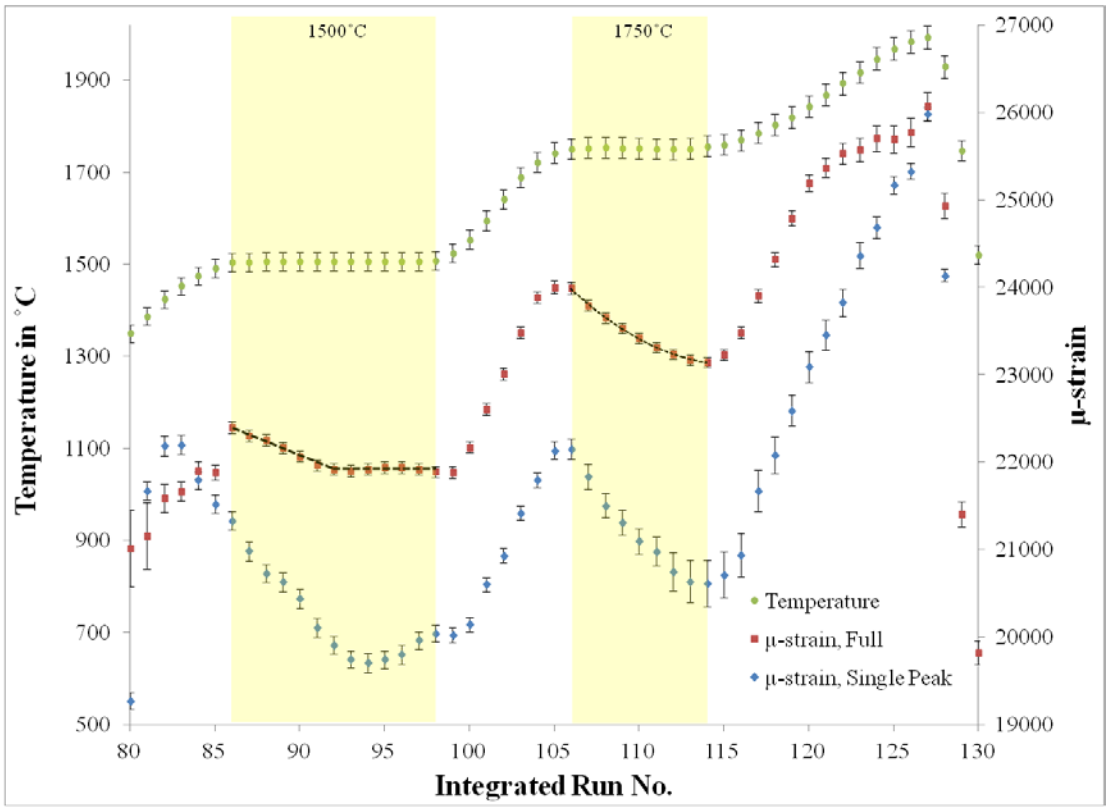

Figure 6.19: Thermal strain of UC_x lattice showing negatice CTE due to carbon diffusion and temperature profile with isothermal measurements shaded in yellow.

all five histograms. Thus, we will consider only the latter results (shown in red of Figure 6.19).

Analog to UO_x, the unit cell of UC_x also shrinks with increasing amount of interstitial atoms. During the isothermal hold at 1500˚C the lattice strain decreases from $22.395 \cdot 10^{-3}$ to $21.919 \cdot 10^{-3}$ within 39 min, before the thermally activated reaction reaches equilibrium. A linear regression calculates a strain rate of $3.09 \cdot 10^{-7} s^{-1}$ with an accuracy of $R^2=0.988$ for this diffusion region. At 1750˚C, the strain rate increases to $4.24 \cdot 10^{-7} s^{-1}$ determined during the 42 min of isothermal holding, which can be

explained due to the higher available thermal activation energy. A polynomial regression of 2nd order increases the R^2 value from 0.876 to 0.977 suggesting that the reaction rate at 1750˚C is controlled by diffusion rather than interface controlled [128]. The 2nd order strain rate approximation is described as:

$$\frac{\Delta d}{d} = 2.292 \cdot 10^{-2} + 9.701 \cdot 10^{-7} T + 3.081 \cdot 10^{-10} T^2 \quad (3.5)$$

After 42 min equilibrium conditions are not reached, implying that more carbon would have diffused into the UC crystal forming UC_2. Unaware of this at the time when the experiment was conducted, I increased the temperature to 2000˚C.

F. Intensity loss at 2000˚C

Starting at 1800˚C, the intensity of UC reflections markedly declines (Figure 6.20). I had to end the experiment prematurely at 2000˚C due to an overheating water chiller. Thus, a possible explanation for the intensity drop is presence of water vapor in the neutron beam. Hydrogen's high incoherent cross section of 80 b could have lead to a rise in background. However, the signal to noise ratio of the reflections at 3.2 and 3.4 Å remains constant. Hence, no increase in background is observed, which rules out water vapor as the reason for the intensity loss, substantiating the indication of an actual order-disorder transition of second order.

A change to a more uranium rich (< 53 at%, Figure 6.4) sample composition, could have caused partial melting of the sample, and thus could account for the loss of intensity. A complete transfer into the liquidus regime can be rejected, because the

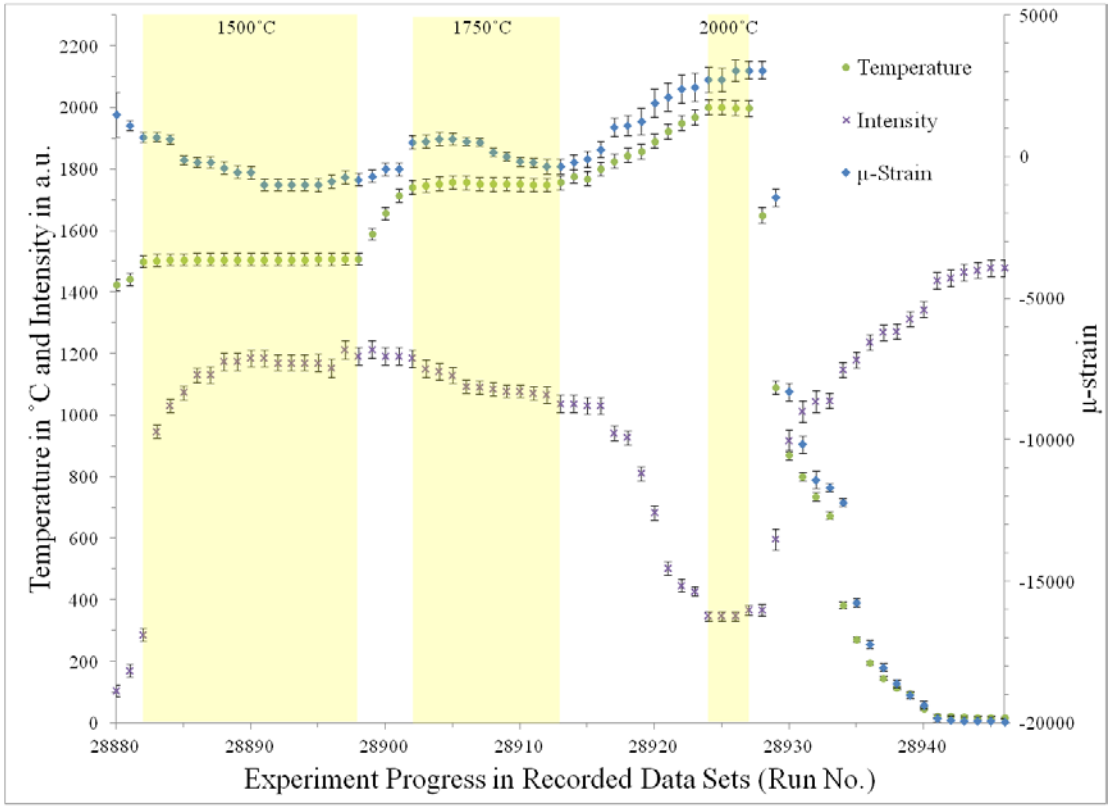

Figure 6.20: Single peak fit for 200 reflection at ~2.5 Å of the UC crystal and temperature profile with isothermal measurements shaded in yellow.

shape of the sample has been preserved. As mentioned above, even if every pair of oxygen atoms that escaped the sample captured a carbon atom to form CO_2, the sample composition would not have increased from 25 at% uranium above 33 at%. Even localized liquid states due to pockets with higher U content can be ruled out, as no uranium phase was detected in the post heat analysis with good statistics in the sample changer. Because the temperature of results in this experiment so far fit well, melting due to a 585˚C higher temperature to reach the melting point of U-75at%C (Figure 6.4) can be ruled out as well.

A number of order-disorder transitions in the anion sublattices have been reported resulting in an intensity loss of reflections as observed. A diffuse structural transition termed ‘Bredig transition’ is marked by the anion sublattice to move freely forming a superionic conductor [31]. The erratic movement of the unbound anions (carbon ions) eliminates the periodicity in the sublattice which will alter the diffraction pattern. However, we cannot neglect the contribution of the sublattice. As evident from the simulation of a diffraction pattern of a U matrix with voided interstitial sites (Figure 6.21, left), unbound anions don’t contribute to new Bragg reflections (lack of long range order), but eliminate some of the reflections of the cation matrix (e.g. intense reflection at ~3.2Å).

The Bredig transition has been observed for many fluorite-type structures including UO_2, generally near 0.8-0.84 [31] of the melting temperature [137]. Hayes [138] refers to this phenomenon as ‘premelting’ and includes silver halides and rare-

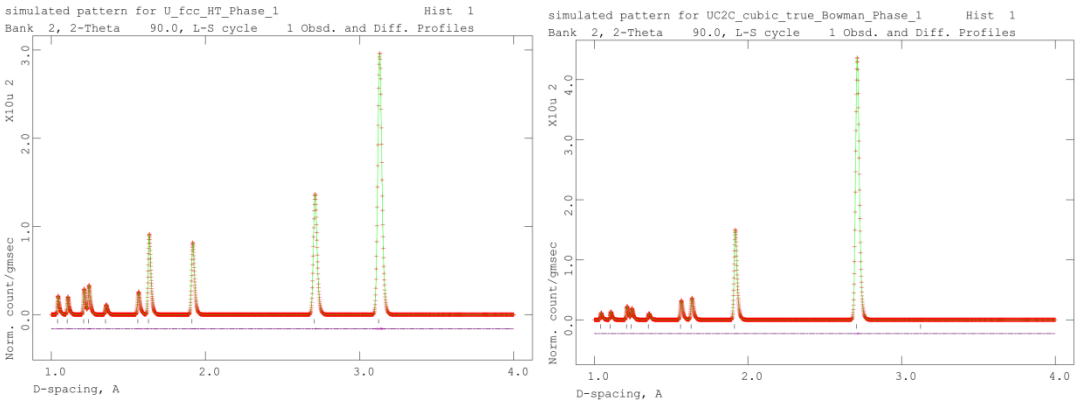

Figure 6.21: Simulated neutron diffraction pattern for fcc uranium matrix with vacated (left) and premelted (right) carbon sublattice; representing modifications of the cubic rock-salt UC_2 phase.

gas solids. We can simulate this state by increasing the thermal motion parameter U_{ISO} from 0.025 to 0.2 (Figure 6.21, right) revealing a vanishing of the 111 reflection. This simulation describes the experimental results better, yet a more viable solution shall be proposed next, as we thus far assumed the ICSD model of Bowman et al. to be correct. However, ICSD used a NaCl-type defect structure with half occupied cations (Figure 6.5, bottom left) to describe the 2:1 ratio of C to U ions. Bowman et al. actually proposed fully occupied U sites with a C_2 molecule at the anion site of the NaCl-type structure. This structure is similar to a pyrite-type structure which was clearly rejected by experimental observations in this work due to the missing 210 and 211 reflections at 2.447 Å and 2.234 Å respectively, thus the necessity of anion motion.

Kracek et al. [139] first described the 'free-rotation' model which constricts sublattice movements to rotations around a fixed interstitial point and belongs to the mean-field (or Landau) theory. A vanishing of the superlattice reflections in calcite ($CaCO_3$) and sodium nitrate ($NaNO_3$) has been explained with the free-rotation model [140]. As the transition temperature is approached, the nitrate and carbonate molecular ions increase in angular oscillation about the *c* axis eventually leading to a continuous rotation. Harris [140] recently described this phenomenon using the XY model of the universality principle resulting in a more accurate match. Free rotation along with random orientation has been first suggested for C_2 groups in the cubic UC_2 phase by Bowman et al. [118]. The postulated free rotation model or it's more recent enhanced counterpart, the XY model, are good candidates describing the thermally

activated anion movements of the C_2 dumbbells necessary to attenuate the pyrite-type reflections analogous to the simulation of a premelted sublattice (Figure 6.21, right). Another promising yet unpublished model considers oscillation rather than rotation of the C_2 molecules. These simulations by Wen et al. [141] utilizing the HSE (Heyd-Scuseria-Ernzerhof) screened Coulomb hybrid density functional show good agreement with structural, optical and electronic properties of cubic UC_2 by ~30˚ angular oscillation of C_2 molecules with a 1.443 Å bond length. Which of the above mentioned models describes the experimental data best needs further investigation.

Rotational dynamic disorder cannot be readily simulated with the Rietveld packages used in this work. Lokshin et al. [142] successfully analyzed rotational molecular dynamics in clathrate hydrate using FullProf (section 3.2). Alternatively, Nishimura et al. [143] evaluated dynamic disorder of Li in Li_xFePO_4 to obtain the nuclear density distribution. Both methods require neutron diffraction data with better statistic. Thus, we are planning to reinvestigate the cubic UC_2 phase after optimizing the high-temperature furnace described in section 4.3 in combination with extended isothermal counting time.

G. Post Heating Evaluation

The sample, after the heating cycle, appears porous due to the release of CO_2 gas according to Equation 3.4. The cylinder also shrank ~16% in each dimension, a 41% reduction in volume, from initially 16 mm diameter by 4 mm to 13.4 mm by 3.3 mm. The main reason for this is the more compact crystal structure of UC with a lattice

parameter of 4.961 Å, compared to the likewise fcc UO_2 unit cell with 5.47 Å accounting for 25% of the volumetric reduction. The remaining 16% volume change is likely due to the release of CO_2 and possibly sintering effects.

An observed 3 wt% UC_2 tetragonal phase in the sample changer is evident from the occurrence of its two strong reflections (Figure 6.5, bottom right); the 110 at 2.5728 Å and the 002 at 3.0038 Å in the recorded histogram (Figure 6.11). This small phase fraction however was not detectable during the experiment in the high-temperature furnace owing to higher noise levels, lower neutron intensities (due to 4 mm collimation) and lower counting times in order to capture reaction kinetics. The 002 of the 2H graphite phase at 3.3555 Å is not matched well by the refinement due to its sizeable texture evident by strong fluctuations in peak intensity throughout the different detector banks.

6.7 Conclusion and Outlook

Utilizing the high-temperature furnace (section 4.3), I found that Bowman's NaCl-type structure is the correct cubic UC_2 structure formed by uranium dicarbide in the graphite rich δ-phase regime. Recent safety calculations and models for accident scenarios in a nuclear reactor conducted by Chevalier and Fischer [120] as well as an independent work by Freyss [121], are inaccurate as these models assume Wilson's CaF_2-type structure. The NaCl structure is also substantiated on chemical grounds as the cubic UC_2 phase is known to form a solid solution with uranium monocarbide. Neither U_2C_3 nor the tetragonal UC_2 phase have been observed due to insufficient

time to rearrange the crystallographic structure, in agreement with Nickel and Saeger [124] and Mukerjee [131] respectively.

The novel synthesis of nano powder UO_2 with a particle size of ~80 nm proved successful. The redox reaction to form UC, with its onset at 1441˚C and its completion at 1650˚C, suggests that transformation temperature and particle size are inversely related, which needs to be further investigated. The observed non-linear strain rate of the carbon enrichment of the UC lattice at 1750˚C suggests it is a diffusion-controlled reaction. Whereas the linear strain rate at 1500˚C hints toward interface control, but also needs additional examination, as the amount of collected data makes this deduction inconclusive. CTE measurements of UO_2 agree well with a review by Martin in the single phase regime.

Commencing at 1800˚C, a second order reversible order-disorder transition has been observed indicating strong thermal motion of C_2 dumbbells at the anion position of the UC crystal. This transition behavior was yet unknown, as recent models do not incorporate such an increase in mean square displacement of the anions [31]. Localized rotation or oscillation of C_2 groups centered at anion position in the NaCl-type structure appears most probable, and agrees with unpublished first principle studies from Wen et al. [141]. A deeper investigation of this phenomenon is proposed.

Neutron diffraction proved to be the appropriate tool to study the described reaction *in situ* as and supplied clarification concerning the UC_2 structure, which only has been accurately determined by this technique.

7.0 CONCLUSION

All three sample environments have been developed and commissioned providing novel insights into crystallography and microstructure evolution as a function of temperature and stress for nuclear materials using neutron diffraction. The automated sample changer significantly reduces the time required to change samples and allows unattended operation of the instrument. Its three degrees of freedom allow for versatile use for texture analysis and sample alignment. Recent advancements in the software, mechanical components, electrical and optical feedbacks resulted in a high resiliency, improving the productivity and reliability of continuous automated sample measurements.

The creep furnace provides new opportunities to study the individual influences of elevated temperatures and uni-axial stress on the texture and lattice parameters of sample materials. I successfully confirmed phase composition and texture via comparison with room temperature results from a known sample environment, as well as temperature dependent lattice parameters which agree with published results of conventional furnaces and literature values. The room temperature measurements of Zr-2.5wt%Nb, before and after deformation at high temperature, clearly demonstrate the necessity of a sample environment as the creep furnace, capable of investigating phase transitions at elevated temperatures and deformation-related texture evolutions *in situ*. The experiment performed with this apparatus allowed to deconvolute the contributions of heating, phase transformation during heating, deformation at temperature in the β field, and phase transformation during cooling. Comparing only

the results before and after the heat and stress treatment, individual factors such as temperature, phase transition and compression cannot accurately be differentiated and as such their individual influence on texture evolution would remain ambiguous.

Variant selection in Zr-2.5wt%Nb has been observed during the $\alpha \rightarrow \beta$ transformation due to anisotropic thermal expansion of the α–phase, as well as during the $\beta \rightarrow \alpha$ transformation due to sample compression during the experiment, simulating extrusion. Texture changes of individual thermo-mechanical manufacturing steps have been quantified and can be used to benchmark and constrain future mechanical models in order to predict the material behavior. Thermal strains of the α–phase have been calculated from the Rietveld fit and agree with values published by Fong et al. [91] for this alloy, as well as literature values for pure Zr [100].

In general, hkl dependent lattice strains (with hkl being the Miller indices of the lattice plane), i.e. the tracking of reflection dependent peak shifts provide the foundation of strain pole figures which grant insight into the three-dimensional mechanical response of a polycrystalline aggregate and represent an extremely powerful material model validation tool. From these lattice strains one can also derive the macroscopic average stress and strain tensors. Such hkl dependent lattice strains are available from each detector panel recording diffraction data. Our setup therefore probes a large number of sample directions, providing a vast amount of constraining experimental data for such models. Creep furnace properties that can be improved are the signal-to-noise ratio and the removal of observed contamination peaks.

Finally, the high-temperature furnace allows unique opportunities to study structure and, by means of a rotating sample stick, also texture information at temperatures up to at least 2200˚C. Utilizing this apparatus, I found that Bowman's NaCl-type structure is the correct cubic UC_2 structure formed by uranium dicarbide in the graphite rich δ-phase regime. Recent safety calculations and models for accident scenarios in a nuclear reactor conducted by Chevalier and Fischer [120] as well as an independent work by Freyss [121], are inaccurate as these models assume Wilson's CaF_2-type structure. The NaCl structure is also substantiated on chemical grounds as the cubic UC_2 phase is known to form a solid solution with uranium monocarbide. Neither U_2C_3 nor the tetragonal UC_2 phase have been observed due to insufficient time to rearrange the crystallographic structure, in agreement with Nickel and Saeger [124] and Mukerjee [131].

The novel synthesis of nano powder UO_2 with a particle size of ~80 nm proved successful. The redox reaction to form UC, with its onset at 1441˚C and its completion at 1650˚C, suggests that transformation temperature and particle size are inversely related, which needs to be further investigated. The observed non-linear strain rate of the carbon enrichment of the UC lattice at 1750˚C suggests it is a diffusion-controlled reaction. Whereas the linear strain rate at 1500˚C hints toward interface control, but also needs additional examination, as the amount of collected data makes this deduction inconclusive. CTE measurements of UO_2 agree well with a review by Martin in the single phase regime.

Commencing at 1800˚C, a second order reversible order-disorder transition has been observed indicating strong thermal motion of C_2 dumbbells at the anion position of the UC crystal. This transition behavior was yet unknown, as recent models do not incorporate such an increase in mean square displacement of the anions [31]. Localized rotation or oscillation of C_2 groups centered at anion position in the NaCl-type structure appears most probable, and agrees with unpublished first principle studies from Wen et al. [141]. A deeper investigation of this phenomenon is proposed.

Due to observed divergence in the neutron beam from the incident collimator to an image plate behind the sample position, I propose to integrate a heat tolerant boron carbide collimator into the heat shield. Such a nearby collimator would allow for a larger beam spot at the sample position, preventing accidental diffraction of adjacent furnace parts and thus provide better statistic and time resolution. Further, we are researching the options of adding calorimetry and gas quenching capabilities. For a temperature measurement above 2320˚C, a pyrometer and neutron resonance spectroscopy [88], [89] are under consideration. As a final improvement for the high-temperature furnace, we are investigating the application of other heat sources. Heating elements made of tungsten alloy sheets would allow for similarly high temperatures, but lower partial pressures of the heating element material and potentially equivalent lifetime based on the grain-growth inhibiting contribution of the alloyed material. Alternatively we are exploring the option of inductively heating the sample, which holds challenges such as selecting sample containers for materials

with low electrical conductivity and determining a suitable balance for the water-cooled RF-coil diameter. A reduction in diameter increases the energy coupled into the sample and, thus, the maximum temperature that can be achieved, but has the downside of increasing the solid angle holding attenuating water which obstructs diffracted neutrons.

Neutron diffraction proved to be the appropriate tool to study the described reaction *in situ* and supplied clarification concerning the cubic UC_2 structure, which only has been accurately determined by this technique.

8.0 BIBLIOGRAPHY

[1] CODATA. NIST: 2010 CODATA recommended values. [Online]. physics.nist.gov/cuu/Constants

[2] Particle Data Group, K. Nakamura et al., "Review of Particle Physics," *J. Phys. G: Nucl. Part. Phys*, vol. 37, p. 075021, 2010.

[3] H.-R. Wenk, "Standard project for pole-figure determination by neutron diffraction," *J. Appl. Cryst.*, vol. 24, pp. 920-927, 1991.

[4] M.R. Daymond, R.A. Holt, S. Cai, P. Mosbrucker, and S.C. Vogel, "Texture inheritance and variant selection through an hcp-bcc-hcp phase transformation," *Acta Mater.*, vol. 58, no. 11, pp. 4053-4066, June 2010.

[5] S.C. Vogel, D. Bhattacharyya, G.B. Viswanathan, D.J. Williams, and H.L Fraser, "Phase transformation textures in Ti-6Al-4V alloy ," *Mater Sci. Forum*, vol. 495-497, pp. 681-686, 2005.

[6] I. Lonardelli, N. Gey, H.-R. Wenk, M. Humbert, and S.C. Vogel, "In situ observation of texture evolution during alpha → beta and beta → alpha phase transformations in titanium alloys investigated by neutron diffraction," *Acta Mater.*, vol. 55, no. 17, pp. 5718-5727, 2007.

[7] S.C. Vogel and H.G. Priesmeyer, "Neutron production, neutron facilities and neutron instrumentation," *Rev. Mineral. Geochem.*, vol. 63, p. 27, 2006.

[8] Paul W. Lisowski and Kurt F. Schoenberg, "The Los Alamos Neutron Science Center," *Nucl. Instrum. Meth. A*, vol. 562, no. 2, pp. 910-914, 2006.

[9] T.E. Mason, M. Arai, and K.N. Clausen, "Next-generation neutron sources ," *MRS Bull.*, vol. 28, no. 12, pp. 923-928, Dec. 2003.

[10] T. Ino et al., "Measurement of neutron beam characteristics at the Manuel Lujan Jr. neutron scattering center," *Nucl. Instrum. Meth. A*, vol. 525, pp. 496-510, 2004.

[11] H.-R. Wenk, L. Lutterotti, and S. Vogel, "Texture analysis with the new HIPPO TOF diffractometer," *Nucl. Instrum. Methods Phys. Res. A*, vol. 515, pp. 575-588, 2003.

[12] A. Huq, J.P. Hodges, O. Gourdon, and L. Heroux, "Powgen: A third-generation high-resolution high-throughput powder diffraction instrument at the Spallation Neutron Source," *Z. Kristallogr. Proc.*, vol. 1, pp. 127-135, 2011.

[13] S.S. Sidhu, L. Heaton, D.D. Zauberis, and F.P. Campos, "Neutron Diffraction Study of Titanium-Zirconium System," *J. Appl. Phsy.*, vol. 27, no. 9, pp. 1040-1042, Sep. 1956.

[14] M.T. Hutchings, "High-temperature studies of U O2 and Th O2 using neutron scattering techniques," *J. Chem. Soc. Farad. T. 2*, vol. 83, pp. 1083-1103, 1987.

[15] R.F. Egerton, *Physical Principles of Electron Microscopy*. New York: Springer Science+Business Media, Inc., 2005.

[16] International Atomic Energy Agency (IAEA) - Power Reactor Information System (PRIS). [Online]. http://www.iaea.org/

[17] P. Avery, *Nuclear Reactor Technology*. Delhi: The English Press, 2011.

[18] International Atomic Energy Agency (IAEA), "Nuclear Technology Review," 2011.

[19] M.W.R Williams, "Calculation of the Void Fraction and Void Coefficient in an Aqueous Homogeneous Reactor," *Nucl. Sci. Eng.*, vol. 168, no. 2, pp. 138-150, 2011.

[20] S. Anghaie, T.W. Knight, R. Norring, and Smith B.M., "Optimum utilization of nuclear fuel with gas and vapor core reactors," *Prog. Nucl. Energ.*, vol. 47, no. 1-4, pp. 74-90, 2005.

[21] U.S. Dept. of Energy - Generation IV. [Online]. http://www.ne.doe.gov/GenIV/neGenIV1.html

[22] B. Villamere, L. Allison, and L. Grande, "Thermal Aspects for Uranium Carbide and Uranium Dicarbide Fuels in Supercritical Water-Cooled Nuclear Reactors," in *ICONE17-75990*, Brussels, Belgium, 2009, pp. 731-742.

[23] L. Grande et al., "Thermal Aspects of Uranium Carbide and Uranium Dicarbide Fuels in Supercritical Water-Cooled Nuclear Reactors," *J. Eng. Gas Turb. Power*, vol. 133, p. 22901, Feb. 2011.

[24] Gen 4 - International Forum. [Online]. http://www.gen-4.org/Technology/systems/scwr.htm

[25] L. Mathieu et al., "Possible Configurations for the Thorium Molten Salt Reactor and Advantages of the Fast Nonmoderated Version," *Nucl. Sci. Eng.*, vol. 161, pp. 78-89, 2009.

[26] H. Cember, *Introduction to Health Physics*. New York: McGraw-Hill, 1996, vol. 3rd ed.

[27] O. Hahn and F. Strassmann, "Ueber die Entstehung von Radiumisotopen aus Uran durch Bestrahlen mit schnellen und langsamen Neutronen," *Naturwissenschaften*, vol. 26, pp. 755-756, 1938.

[28] R. Lenk, *Physik*, 2nd ed. Leipzig, DDR: VEB F. A. Brockhaus Verlag, 1989.

[29] J.J., Hamilton, L.G. Duderstadt, *Nuclear Reactor Analysis*. New York: Wiley, 1976.

[30] K. Yamada, K. Kurosaki, M. Uno, and S. Yamanaka, "Evaluation of thermal properties of uranium dioxide by molecular dynamics," *J. Alloy Compd.*, vol. 307, pp. 10-16, 2000.

[31] C.B. Basak, "Classical molecular dynamics simulation of uranium monocarbide (UC)," *Comp. Mater. Sci.*, vol. 40, pp. 562-568, 2007.

[32] S.C. Vogel et al., "Texture measurements using the new neutron diffractometer HIPPO and their analysis using the Rietveld method," *Powder Diffr.*, vol. 19, no. 1, p. 65, 2004.

[33] H.M. Rietveld, "A profile refinement methode for nuclear and magnetic structures," *J. Appl. Crystallogr.*, vol. 2, p. 65, 1969.

[34] R.A. Young, *The Rietveld Method*. New York: Oxford University Press, 1995.

[35] R.B. Von Dreele, J.D. Jorgensen, and C.G. Windsor, "Rietveld refinement with spallation neutron powder diffraction data," *J. Appl. Crystalogr.*, vol. 15, p. 581, 1982.

[36] R.B. Von Dreele, "Quantitative texture analysis by Rietveld refinement," *J. Appl. Cryst.*, vol. 30, pp. 517-525, 1997.

[37] A.C. Larson and R.B. Von Dreele, "General Structure Analysis System (GSAS)," 2004.

[38] GSAS - General Structure Analysis System. [Online]. http://www.ncnr.nist.gov/xtal/software/gsas.html

[39] S.C. Vogel, "gsaslanguage: a GSAS script language for automated Rietveld refinements of diffraction data," *J. Appl. Cryst.*, vol. 44, pp. 873 - 877, 2011.

[40] L. Lutterotti, S. Matthies, H.-R. Wenk, A. J. Schultz, and J. W. Richardson, "Combined texture and structure analysis of deformed limestone from time-of-flight neutron diffraction spectra," *J. Appl. Phys.*, vol. 81, no. 2, p. 594, 1997.

[41] S. Matthies, J. Pehl, H.-R. Wenk, L. Lutterotti, and S.C. Vogel, "Quantitative texture analysis with the HIPPO neutron TOF diffractormeter," *J. Appl. Cryst.*, vol. 38, p. 462, 2005.

[42] MAUD - Materials Analysis Using Diffraction. [Online]. http://www.ing.unitn.it/~maud/

[43] H.-R. Wenk, L. Lutterotti, and S.C. Vogel, "Rietveld texture analysis from TOF neutron diffraction data," *Powder Diffr.*, vol. 25, no. 3, pp. 283 - 296, 2010.

[44] J. Rodriguez-Carvajal, "Recent advances in magnetic structure determination by neutron powder diffraction," *Physica B*, vol. 192, p. 55, 1993.

[45] FullProf Suit Rietveld Analysis Software. [Online]. http://www.ill.eu/sites/fullprof/

[46] A.A. Coelho, "Indexing of powder diffraction patterns by iterative use of singular value decomposition," *J. Appl. Crystallogr.*, vol. 36, p. 86, 2003.

[47] TOPAS-Academic Rietveld Analysis Software. [Online]. http://www.topas-academic.net

[48] H.M. Reiche and S.C. Vogel, "A versatile automated sample changer for texture measurements on the high pressure-preferred orientation neutron diffractometer," *Rev. Sci. Instrum.*, vol. 81, no. 9, p. 93302, 2010.

[49] J.S. Kallend, U.F. Kocks, A.D. Rollett, and H.R. Wenk, "POPLA - An Integrated Software System for Texture Analysis," *Textures and Microstruct.*, vol. 14, p. 1203, 1991.

[50] R.A. Lebensohn and C.N. Tome, "A self-consistent anisotropic approach for the simulation of plastic deformation and texture development of polycrystals: Application to zirconium alloys," *Acta Metall. Mater.*, vol. 41, pp. 2611-2624, 1993.

[51] U.F. Kocks, C.N. Tome, and H.-R. Wenk, *Texture and Anisotropy*. Cambridge: Cambridge University Press, 1998.

[52] P. Wessel and W.H.F. Smith, "Free software helps map and display data," *EOS Trans. Amer. Geophys. U.*, vol. 72, p. 441, 1991.

[53] P. Wessel and W.H.F. Smith, "New Version of the Generic Mapping Tools released," *EOS Trans. Amer. Geophys. U.*, vol. 76, p. 329, 1995.

[54] P. Wessel and W.H.F. Smith, "New, Improved version of Generic Mapping Tools released," *EOS Trans. Amer. Geophys. U.*, vol. 79, p. 579, 1998.

[55] Ghostscript. [Online]. http://www.ghostscript.com/

[56] F. Wagner, H.-R. Wenk, H. Kern, P. Van Houtte, and C. Esling, "Development of Preferred Orientation in Plane Strain Deformed Limestone: Experiment and Theory," *Miner. Petrol.*, vol. 80, pp. 132-139, 1982.

[57] X.-L. Wang, Y.D. Wang, and J.W. Richardson, "Experimental error caused by sample displacement in time-of-flight neutron diffractometry," *J. Appl. Cryst.*, vol. 35, pp. 533-537, 2002.

[58] S. Vogel, *High-Pressure and Texture Measurements with an Imaging Plate*. Kiel, Germany: Christian-Albrechts-Universität, 2001.

[59] H. von Seggern, T. Voigt, W. Knuepfer, and G. Lange, "Physical model of photostimulated luminescence of X-ray irradiated BaFBr:Eu2+," *J. Appl. Phys.*, vol. 64, no. 3, pp. 1405-1412, 1988.

[60] H.M. Shah, "An automated, temperature controlled, twelve-position sample changer for neutron scattering instruments," *Physica B*, p. 551, 1991.

[61] J.E. Rix et al., "Automated sample exchange and tracking system for neutron research at cryogenic temperatures," *Rev. Sci. Instrum.*, vol. 78, no. 1, p. 13907, 2007.

[62] H.-R. Wenk and P. Van Houtte, "Texture and Anisotropy," *Rep. Prog. Phys.*, vol. 67, pp. 1367-1428, 2004.

[63] Square One Systems Design, Jackson, WY. [Online]. http://www.sqr-1.com

[64] Zygo, Middlefield, CT. [Online]. http://www.zygo.com/

[65] I.F. Bailey, "A review of sample environments in neutron scattering," *Z. Kristallogr.*, vol. 218, p. 84, 2003.

[66] A. Hoshikawa et al., "Development of an automatic sample changer for iMATERIA," *Nucl. Instrum. Meth. A*, vol. 600, pp. 203-206, 2009.

[67] Part 'SWX-238A', Shieldwerx, Rio Rancho, NM. [Online]. http://www.shieldwerx.com

[68] Model '5202.2', Huber Diffraction and Positioning Equipment, Rimsting, Germany. [Online]. http://www.xhuber.de/en

[69] Parker Hannifin Corporation, Rohnert Park, CA. [Online]. http://www.compumotor.com/

[70] Model 'Tom Thumb', Phd Inc., Ft. Wayne, IN. [Online]. http://www.phdinc.com

[71] H.-R. Wenk, I. Lonardelli, S.C. Vogel, and J. Tullis, "Dauphine twinning as evidence for an impact origin of preferred orientation in quartzite: An example from Vredefort, South Africa," *Geology*, vol. 33, no. 4, pp. 273-276, 2005.

[72] M. Kawasaki, I.J. Beyerlein, S.C. Vogel, and T.G. Langdon, "Characterization of creep properties and creep textures in pure aluminum processed by equal-channel angular pressing," *Acta Mater.*, vol. 56, no. 10, pp. 2307-2317, 2008.

[73] Kaixiang Tao et al., "In situ neutron diffraction study of grain-orientation-dependent phase transformation in 304L stainless steel at a cryogenic temperature," *J. Appl. Phys.*, vol. 100, p. 123515, 2006.

[74] B. Ye, B.S. Majumdar, and I. Dutta, "Texture memory and strain-texture mapping in a NiTi shape memory alloy," *Appl. Phys. Lett.*, vol. 91, no. 6, p. 061918, 2007.

[75] J.G. Barreiro et al., "Fabric Development in a Middle Devonian Intraoceanic Subduction Regime: The Careón Ophiolite (Northwest Spain)," *J. Geol.*, vol. 118, pp. 163-186, 2010.

[76] R.J. McQueeney et al., "Unusual Phonon Softening in delta-Phase Plutonium," *Phys. Rev. Lett.*, vol. 92, no. 14, p. 146401, 2004.

[77] L.R. Dalesio et al., "The experimental physics and industrial control system architecture: past, present, and future," *Nucl. Instrum. Meth. A*, vol. 352, no. 1-2, p. 179, 1994.

[78] Model 'VOS 310', Pepperl & Fuchs, Mannheim, Germany. [Online]. http://www.pepperl-fuchs.com

[79] H.M. Reiche, S.C. Vogel, P. Mosbrucker, E.J. Larson, and M.R. Daymond, "A furnace with rotating load frame for in situ high temperature deformation and creep experiments in a neutron diffraction beam line," *Rev. Sci. Instrum.*, vol. 83, no. 5, p. 053901, 2012.

[80] N. Gey et al., "Study of the α/β phase transformation of Zy-4 in presence of applied stresses at heating: analysis of the inherited microstructures and textures," *J. Nucl. Mater.*, vol. 302, no. 2-3, pp. 175-184, 2002.

[81] B. Winkler et al., "In situ observation of the formation of TiC from the elements by neutron diffraction," *J. Alloy Compd.*, vol. 441, pp. 374-380, Jan. 2007.

[82] ICSD Database of FIZ Karlsruhe – Leibniz Institute for Information Infrastructure. [Online]. http://icsd.fiz-karlsruhe.de/

[83] M.G. Bowman, D.E. Hull, W.G. Witteman, G.P. Arnold, and A.L. Bowman, "High temperature neutron diffraction furnace ," *Rev. Sci. Instrum.*, vol. 37, no. 11, pp. 1543-1544, 1966.

[84] G. Lorenz, R.B. Neder, J. Marxreiter, F. Frey, and J. Schneider, "A Mirror Furnace for Neutron Diffraction up to 2300 K," *J. Appl. Cryst.*, vol. 26, pp. 632-635, 1993.

[85] K. Clausen et al., "Investigation of oxygen disorder, thermal parameters, lattice vibrations and elastic constants of UO2 and ThO2 at temperatures up to 2930 K ," *Rev. Phys. Appl.*, vol. 19, pp. 719-722, 1984.

[86] A. Kahle, B. Winkler, B Hennion, and P. Boutrouille, "High-temperature furnace for dynamic neutron radiography," *Rev. Sci. Instrum.*, vol. 74, no. 8, pp. 3717-3721, Aug. 2003.

[87] E.A. Juarez-Arellano et al., "Reaction of rhenium and carbon at high pressures and temperatures," *Z. Kristallogr.*, vol. 223, pp. 492-501, 2008.

[88] H.J. Stone et al., "Remote determination of sample temperature by neutron resonance spectroscopy ," *Nucl. Instrum. Meth. A*, vol. 547, pp. 601-615, 2005.

[89] V.W. Yuan et al., "Shock Temperature Measurement Using Neutron Resonance Spectroscopy," *Phys. Rev. Lett.*, vol. 94, p. 125504, Apr. 2005.

[90] R.A Holt, "In-reactor deformation of cold-worked Zr-2.5Nb pressure tubes," *J Nucl Mater*, vol. 372, pp. 182-214, 2008.

[91] R.W.L. Fong, R Miller, H.J. Saari, and S.C. Vogel, "Crystallographic Texture and Volume Fraction of alpha and beta Phases in Zr-2.5Nb Pressure Tube Material During Heating and Cooling," *Metall. Mater. Trans. A*, vol. 43A, pp. 806-821, 2012.

[92] R.W.L. Fong, H. Saari, R. Miller, J. Teutsch, and S.C. Vogel, "A DSC Study of Phase Changes in an As-received Zr.2.5Nb Pressure Tube Material during Continuous Heating and Cooling," *Mater. Sci. Forum*, vol. 706-709, pp. 853-858, 2012.

[93] P. Mosbrucker, M.R. Daymond, and R.A. Holt, "In situ studies of variant selection during the alpha-beta-alpha phase transformation in Zr-2.5Nb," *Journal of ASTM Intl.*, vol. 8, no. 1, p. JAI103066 , 2011.

[94] Y. Li, R. Rogge, and R.A. Holt, "Development of local microstructure and crystallographic texture in extruded Zr–2.5Nb tubes," *Mat. Sci. Eng. A-Strut.*, vol. 437, pp. 10-20, 2006.

[95] H.-R. Wenk, I. Lonardelli, and D. Williams, "Texture changes in the hcp → bcc → hcp transformation of zirconium studied in situ by neutron diffraction," *Acta Mater*, vol. 52, no. 7, pp. 1899 - 1907, 2004.

[96] H. Okamoto, "Nb-Zr (Niobium-Zirconium)," *J. Phase Equilib.*, vol. 13, p. 577, 1992.

[97] G.C. Kaschner et al., "Exploring the dislocation/twin interactions in zirconium," *Mat. Sci. Eng. A-struct.*, vol. 463, no. 1-2, pp. 122-127, 2007.

[98] T.A. Sisneros et al., "Influence of strain rate on mechanical properties and deformation texture of hot-pressed and rolled beryllium ," *Mat. Sci. Eng. A-Struct.*, vol. 527, no. 20, pp. 5181-5188, July 2010.

[99] I.S. Lupakov, B.S. Rodchenkov, V.N. Vukolova, and V.N. Tyurin, "Structure and Phase Composition of Weldments in the Zr-2.5Nb Alloy," *Met. Sci. Heat Treat+*, vol. 15, pp. 379-381, 1973.

[100] Y.S Touloukian, *Thermal Expansion: metallic elements and alloys*. New York: IFI/Plenum, 1975.

[101] I.T. Bethune and C.D. Williams, "The alpha/(alpha+beta) Boundary in the Zr-Nb System," *J. Nucl. Mater.*, vol. 29, pp. 129-132, 1969.

[102] Y.D. Wang, X.-L. Wang, A.D. Stoica, J.W. Richardson, and R. Lin Peng, "Determination of the stress orientation distribution function using pulsed neutron sources," *J. Appl. Cryst.*, vol. 36, pp. 14-22, 2003.

[103] M.R. Daymond, M.A.M. Bourke, R.B. Von Dreele, B. Clausen, and T. Lorentzen, "Use of Rietveld refinement for elastic macrostrain determination and for evaluation of plastic strain history from diffraction spectra ," *J. Appl. Phys.*, vol. 82, no. 4, pp. 1554-1562, 1997.

[104] N.C. Popa and D. Balzar, "Elastic strain and stress determination by Rietveld refinement: generalized treatment for textured polycrystals for all Laue classes," *J. Appl. Cryst.*, vol. 34, pp. 187-195, 2001.

[105] M.R. Daymond, "The determination of a continuum mechanics equivalent elastic strain from the analysis of multiple diffraction peaks," *J. Appl. Phys.*, vol. 96, no. 8, pp. 4263-4272, 2004.

[106] D. Balzar, N.C. Popa, and S. Vogel, "Strain and stress tensors of rolled uranium plate by Rietveld refinement of TOF neutron-diffraction data," *Mat. Sci. Eng. A-Struct.*, vol. 528, pp. 122-126, 2010.

[107] B.R.T. Frost, "The Carbides of Uranium," *J. Nucl. Mater.*, vol. 10, no. 4, pp. 265-300, 1963.

[108] R. De Coninck, W. Van Lierde, and A. Gijs, "Uraniumcarbide: Thermal diffusivity, thermalconductivity and spectral emissivity at high temperatures," *J. Nucl. Mater.*, vol. 57, pp. 69-76, 1975.

[109] D.G. Martin, "A re-appraisal of the thermal conductivity of UO2 and mixed (U,Pu) oxide fuels," *J. Nucl. Mater.*, vol. 110, pp. 73-94, 1982.

[110] D.G. Martin, "The Thermal Expansion of Solid UO2 and (U,Pu) Mixed Oxides - A Review and Recommendations," *J. Nucl. Mater.*, vol. 152, pp. 94-101, 1988.

[111] H. Matzke, "On the rim effect in high burnup UO2 LWR fuels," *J Nucl. Mater.*, vol. 189, pp. 141-148, 1992.

[112] H. Wu, Y. Yang, and C. Cao, "Synthesis of Colloidal Uranium - Dioxide Nanocrystals," *J. Am. Chem. Soc.*, vol. 128, no. 51, pp. 16522-16523, 2006.

[113] O. Roth, H. Hasselberg, and M. Jonsson, "Radiation chemical synthesis and characterization of UO2 nanoparticles," *J. Nucl. Mater.*, vol. 383, pp. 231-236, 2009.

[114] T.M. Nenoff et al., "Synthesis and low temperature in situ sintering of uranium oxide nanoparticles ," *Chem. Mater.*, vol. 23, no. 23, pp. 5185-5190, 2011.

[115] S. Hasan, T.K. Ghosh, D.S. Viswanath, S.K. Loyalka, and B. Deng, "Synthesis of Uranium Oxide Nanoparticles in Aqueous Solutions ," *T. Am. Nucl. Soc.*, vol. 96, no. 1, pp. 180-182, June 2007.

[116] Q. Wang, G.-D. Li, S. Xu, J.-X. Li, and J. Chen, "Synthesis of uranium oxide nanoparticles and their catalytic performance for benzyl alcohol conversion to benzaldehyde," *J. Mater. Chem.*, vol. 18, no. 10, pp. 1146-1152, Mar. 2008.

[117] M.A. Bredig, "The High-Temperature Cubic Phases of Uranium and Lanthanum Dicarbides," *J. Am. Ceram. Soc.*, vol. 43, p. 493, 1960.

[118] A.L. Bowman, G.P. Arnold, W.G. Wittman, T.C. Wallace, and N.G. Nereson, "Crystal Structure of UC2," *Acta. Crystallogr.*, vol. 21, pp. 670-671, 1966.

[119] W.B. Wilson, "High-temperature X-ray diffraction investigation of uranium-carbon system," *J. Am. Ceram. Soc.*, vol. 43, pp. 77-81, 1960.

[120] P.Y. Chevalier and E. Fischer, "Thermodynamic modelling of the C-U and B-U binary systems," *J. Nucl. Mater.*, vol. 288, pp. 100-129, 2001.

[121] M. Freyss, "First-principles study of uranium carbide: Accommodation of point defects and of helium, xenon, and oxygen impurities," *Phys. Rev. B*, vol. 81, p. 014101, 2010.

[122] T.B. Massalski, *Binary Alloy Phase Diagrams*.: William W. Scott, Jr. Materials Park, Ohio, 1990.

[123] R. Chang, "A diffusionless UC2 (cubic) to UC2 (tetragonal) transformation," *Acta Crystalogr.*, vol. 14, pp. 1097-1098, 1961.

[124] H. Nickel and H. Saeger, "Ueber die Bildung des U2C3," *J. Nucl. Mater.*, vol. 28, pp. 93-104, 1968.

[125] L.E. Thomas, R.W. Knoll, L.A. Charlot, J.E. Coleman, and E.R. Gilbert, "Storage of LWR Spent Fuel in Air: Volume 2: Microstructural Characterization of Low-Temerature Oxidized LWR Spent Fuel," Pacific Northwest Lab., Richland, WA, Technical Report PNL-6640-Vol.2, 1989.

[126] R.J. McEachern and P. Taylor, "A review of the oxidation of uranium dioxide at temerpatures below 400C," *J. Nucl. Mater.*, vol. 254, no. 2-3, pp. 87-121, 1998.

[127] B. Belbeoch, C. Piekarski, and P. Perio, "Structure of U4O9," *Acta Crystalogr.*, vol. 14, no. 8, pp. 837-843, Aug. 1961.

[128] S. Vogel, E. Ustundag, J.C. Hanan, V.W. Yuan, and M.A.M. Bourke, "In-situ investigation of the reduction of NiO by a neutron transmission method," *Mat. Sci. Eng. A-Struct.*, vol. 333, pp. 1-9, 2002.

[129] S.C. Vogel, H. Reiche, and D.W. Brown, "High pressure deformation study of zirconium," *Powder Diffr.*, vol. 22, no. 2, pp. 113-117, 2007.

[130] S. Pojprapai et al., "Dynamic processes of domain switching in lead zirconate titanate under cyclic mechanical loading by in situ neutron diffraction ," *Acta Mater.*, vol. 58, no. 6, pp. 1897-1908, 2010.

[131] S.K. Mukerjee, J.V. Dehadraya, V.N. Vaidya, and D.D. Sood, "Kinetics and Mechanism of UO2+C Reaction for UC/UC2 Preparation," *J. Nucl. Mater*, vol. 210, no. 1-2, pp. 107-114, 1994.

[132] A.E. Austin, "Carbon Positions in the Uranium Carbides," *Acta Crystallogr.*, vol. 12, pp. 159-161, 1959.

[133] Y.S Touloukian, *Thermal Expansion: Nonmetallic Solids*. New York: IFI/Plenum, 1977.

[134] P.E. Blackburn, J. Weissbart, and E.A. Gulbransen, "Oxidation of Uranium Dioxide," *J. Phys. Chem.*, vol. 62, no. 8, pp. 902-908, 1958.

[135] M. Iwasaki and N. Ishikawa, "Air-Oxidation of UO2 Pellets at 800 and 900 C," *J. Nucl. Mater.*, vol. 36, no. 1, pp. 116-119, 1970.

[136] F Weigel, *The Chemistry of the Actinide Elements*, 2nd ed., G. T. Seaborg & L. R. Morss, J. J. Katz, Ed. London, UK: Chapman & Hill., 1986.

[137] J. Ralph and G.J. Hyland, "Empirical confirmation of a Bredig transition in UO2," *J. Nucl. Mater.*, vol. 132, pp. 76-79, 1985.

[138] W. Hayes, "Premelting," *Contem. Phys.*, vol. 27, no. 6, pp. 519-532, 1986.

[139] F.C. Kracek, E. Posnjak, and S.B. Hendricks, "Gradual transition in sodium nitrate II. The structure at various temperatures and its bearing on melecular rotation.," *J. Am. Chem. Soc.*, vol. 53, pp. 3339-3348, 1931.

[140] M.J. Harris, "A new explanation for the unusual critical behavior of calcite and sodium nitrate, NaNO3," *Am. Mineral.*, vol. 84, pp. 1632-1640, 1999.

[141] X.-D. Wen et al., "Rotational rehybridization and the high temperature phase of UC2," *unpublished*.

[142] K.A. Lokshin et al., "Structure and Dynamics of Hydrogen Molecules in the Novel Clathrate Hydrate by High Pressure Neutron Diffraction," *Phys. Rev. Lett.*, vol. 93, no. 12, p. 125503, Sep. 2004.

[143] S.-I. Nishimura et al., "Experimental visualization of lithium diffusion in LixFePO4 ," *Nat. Mater.*, vol. 7, no. 9, pp. 707-711, Sep. 2008.